University of Alberta

Novel Methods of Measuring Single Scan Dose Profiles and Cumulative Dose in Computed Tomography

By

Keith Nakonechny

A thesis submitted to the Faculty of Graduate Studies and Research in Partial fulfillment of the requirement for the degree of Master of Science

in

Medical Physics

Department of Physics

Edmonton, Alberta

Fall 2004

Library and Archives Canada

Published Heritage Branch

395 Wellington Street
Ottawa ON K1A 0N4
Canada

Bibliothèque et Archives Canada

Direction du Patrimoine de l'édition

395, rue Wellington
Ottawa ON K1A 0N4
Canada

Your file Votre référence
ISBN: 0-612-95825-6
Our file Notre référence
ISBN: 0-612-95825-6

The author has granted a non-exclusive license allowing the Library and Archives Canada to reproduce, loan, distribute or sell copies of this thesis in microform, paper or electronic formats.

The author retains ownership of the copyright in this thesis. Neither the thesis nor substantial extracts from it may be printed or otherwise reproduced without the author's permission.

L'auteur a accordé une licence non exclusive permettant à la Bibliothèque et Archives Canada de reproduire, prêter, distribuer ou vendre des copies de cette thèse sous la forme de microfiche/film, de reproduction sur papier ou sur format électronique.

L'auteur conserve la propriété du droit d'auteur qui protège cette thèse. Ni la thèse ni des extraits substantiels de celle-ci ne doivent être imprimés ou aturement reproduits sans son autorisation.

In compliance with the Canadian Privacy Act some supporting forms may have been removed from this thesis.

While these forms may be included in the document page count, their removal does not represent any loss of content from the thesis.

Conformément à la loi canadienne sur la protection de la vie privée, quelques formulaires secondaires ont été enlevés de cette thèse.

Bien que ces formulaires aient inclus dans la pagination, il n'y aura aucun contenu manquant.

Canada

For Shelley

Acknowledgement

I would like to acknowledge and thank all those who have helped and supported me during this research and throughout the years. I thank my graduate supervisors Dr. Satyapal Rathee and Dr. Gino Fallone for their guidance during the course of this work. I also thank the physicists and staff at the Cross Cancer Institute in Edmonton whom, at one time or another, were all "graced" with a timid knock at their door from me wanting assistance or advice. I would also like to acknowledge a few people from my undergrad years at the University of Regina, specifically Dr. Peter Bergbusch who instilled in me the notion to be the best at whatever it is you are doing, even if no one is looking! I would also like to thank Dr. Ted Mathie for his years of support and for not turning me away on that first day when I came to him a lowly, anonymous musician, wanting to enter that "money-maker" of a field ... physics.

Speaking of money, I would like to acknowledge the Natural Science and Engineering Research Council of Canada (NSERC), Informatics Circle of Research Excellence (iCORE), and the Alberta Cancer Board (ACB) for funding this work and thank them for allowing me to put some food on the table (bonus).

Who would of thought one could meet a good bunch of people along the way as well? In no particular order, thanks to Moira, Kristel, Anna, Tara, Steven, Erin, Alana, Deluan and the many others who made the journey more than just what is in the text book or on the computer screen, and for making me feel like the rock star I never was. Speaking of that, thanks to the Waltons clan, Jason, Todd, Sean, Dave and Brent. I'm one step closer to becoming the "spaceboy" you always imagined for me.

Of course, many thanks and much love goes out to my parents Don and Gloria for their years and years (and years) of love and support, and for encouraging me to do whatever it is I have chosen to do over the years. I'll get it right yet!

To Shelley, it is impossible to thank you for everything you do and everything that you are, but thank you for your support and patience on the many nights and days I was "away" trying to solve some equation or problem, even though I was physically in the next room. It's sad when I need an email to remember to do something like take out the garbage! And thank you to Talia and Mira, not for any particular reason other than being a part of my life.

Contents

1 Thesis Overview 1

Chapter 1 References 6

2 Background 8

2.1 Basics of CT 8

2.1.1 Elementary Theory of Image Formation 8

2.1.2 CT Scanner Generations and Developments 10

2.1.2.1 First Generation 10

2.1.2.2 Second Generation 11

2.1.2.3 Third Generation 11

2.1.2.4 Fourth Generation 12

2.1.2.5 Fifth Generation 12

2.1.2.6 Axial Scan Mode 12

2.1.2.7 Helical Volume Scanning 13

2.1.2.8 Multiple Slice Systems 14

2.2 Applications of CT 15

2.2.1 Diagnosis 15

2.2.2 Radiotherapy Treatment Planning 15

2.3 Radiation Dose from CT 15

2.3.1 Dose Distributions 15

2.3.1.1 Scan Plane 15

2.3.1.2 Longitudinal Axis 17

2.3.2 CT Phantoms 18

2.3.2.1 Cylindrical PMMA Phantoms 18

2.3.2.2 Anthropomorphic Phantoms 19

2.3.3 Multiple Scan Average Dose (MSAD) 20

2.3.4 Computed Tomography Dose Index (CTDI) 22

2.3.5 Measuring MSAD and CTDI 25

2.3.5.1 Film 25
2.3.5.2 TLDs 26
2.3.5.3 Pencil Ionization Chambers 29
2.3.6 Practical CTDI Variations 30
2.3.6.1 $CTDI_{14T}$ and $CTDI_{FDA}$ 30
2.3.6.2 $CTDI_{100}$ 32
2.3.6.3 Weighted CTDI 33
2.3.6.4 Dose Length Product (DLP) 33
2.3.7 Monte Carlo Methods 33
2.3.7.1 Effective Dose 34
2.3.7.2 Energy Imparted 35
2.3.8 Accumulated Dose $D_L(z)$ 36
2.3.8.1 Helical Scans 36
2.3.8.2 Axial Scanning 39
2.3.8.3 Helical Scanning for Off-Axis Points or Non-Cylindrical Phantoms 40
2.3.9 Relationship Between Dose and Image Quality 41
2.3.10 Factors Affecting Dose 42
2.3.10.1 X-Ray Tube Voltage (kVp) 42
2.3.10.2 Tube Current-Time Product (mAs) 43
2.3.10.3 Beam Collimation 43
2.3.10.4 Filtration 43
2.3.10.5 Focus-Axis Distance 44
2.3.10.6 Pitch or Scan Interval 44
2.3.10.7 Patient Size 44
2.3.10.8 Number of Slices 45
2.3.10.9 Rotation Angle 45
2.3.10.10 Single Slice vs. Multi-Slice Scanners 45
2.4 The Basic Problem and the Scope of this Thesis 46
Chapter 2 References 49

3 Materials and Methods **54**
3.1 CT Equipment 55
3.1.1 PQ5000 Single-Slice Scanner 55
3.1.2 MX8000 Quad Multi-Slice Scanner 56
3.2 Dosimeters 57

3.2.1 Diamond Detector 58
3.2.1.1 Basic Properties 58
3.2.1.2 Detection Mechanism 60
3.2.1.3 Priming 61
3.2.1.4 Energy Dependence 61
3.2.1.5 Directional Dependence 62
3.2.1.6 Dose Rate Dependence 62
3.2.2 Pencil Ion Chamber 63
3.2.3 IC-10 Ion Chamber 63
3.2.4 TLDs 64
3.3 Phantoms 65
3.3.1 CIRS Plastic Water Phantom 65
3.3.2 PMMA (CTDI) Phantoms 67
3.4 Single Scan Dose Profile Measurements 69
3.4.1 Diamond Detector Operation 69
3.4.2 Measurement Method 70
3.4.2.1 CIRS Phantom 70
3.4.2.2 CTDI Phantoms 72
3.4.3 Uncertainty Assessment 73
3.4.4 Verification using Alternate Dosimeters 73
3.5 Accumulated Dose Measurements 76
3.5.1 Ion Chamber Calibration 76
3.5.2 Dosimeter Energy Dependence 78
3.5.3 $D_L(0)$ Measurements 81
3.5.4 CTDI_{100} Measurements 83
3.5.5 Uncertainty Assessment for $D_L(0)$ and CTDI_{100} 83
Chapter 3 References 85

4 Results and Discussion **88**
4.1 Detector Energy Response 89
4.2 SSDPs 90
4.2.1 Analytic Profile Fitting 93
4.2.2 Profile Asymmetry 94
4.2.3 Off-Axis 97
4.2.4 Detector Comparison 99
4.2.5 Effect of Phantom Length 100

4.2.6 CTDI Phantoms 100
4.3 Cumulative Dose Profiles 102
4.4 Measuring $D_L(0)$ using a Small Volume Ion Chamber 103
4.4.1 Axial Mode Considerations 105
4.4.2 Helical Mode Considerations 106
4.4.3 $D_L(0)$ Results 110
4.4.3.1 Comparison to Pencil Chamber/$CTDI_{100}$ . . . 112
4.4.3.2 Helical vs. Axial Modes 113
4.4.3.3 Long Scan Lengths 113
Chapter 4 References 114

5 Conclusions **116**

List of Citations **120**

List of Tables

Table II Published results of the dose (relative to the peak dose of the SSDP) along the central axis of the CTDI body phantom at two z positions corresponding to the edges of 15 cm long CTDI phantoms and the dimensions of 10 cm long pencil chambers. Data is based on either Monte Carlo-generated (MC) or TLD-measured SSDPs as indicated. 46

Table III.a Selectable operating parameters on the PQ5000 single-slice scanner that affect the patient dose. 55

Table III.b Selectable operating parameters on the MX8000 Quad multi-slice scanner that affect the patient dose. 56

Table III.c Operating parameters of the PTW Riga Type 60003 diamond detector as supplied by the manufacturer. . . . 59

Table III.d Energy and filtration combinations of the Pantak orthovoltage x-ray unit used in determining the energy-dependent responses of the detectors used in this study (excluding TLDs). 80

Table III.e Justification of the choice of scan lengths L used in measuring $D_L(0)$. 81

Table IV.a Parameter values of the central axis SSDP fits using Eq. (4.6) for the PQ5000, 10 mm slice width (PQ-10) and the MX8000, 1×20 mm slice selection (MX-20). . 94

Table IV.b Accumulated dose at the center of the scan series $D_L(0)$ for the PQ5000 CT scanner. Pencil chamber/$CTDI_{100}$ readings (equivalent to $L = 102$ mm) for comparison are in brackets. Measurement settings: 130 kVp, Axial: $b = 4$ mm for all T, Helical: $\nu\tau = P \cdot T$. Note that the quoted values of $D_L(0)$ have been calculated with $\nu\tau = b = T$ and expressed as air-kerma per 100 mAs. . 111

Table IV.c Accumulated dose at the center of the scan series $D_L(0)$ for the MX8000 Quad multi-slice CT scanner (120 kVp) at the center of the CIRS phantom for axial scans ($b = 4$ mm for all T). Pencil chamber/$CTDI_{100}$ readings (equivalent to $L = 102$ mm) for comparison are in brackets. Note that the quoted values of $D_L(0)$ have been calculated with b = slice width and expressed as air-kerma per 100 mAs. 112

List of Figures

Figure 2.1 General configuration of the major components and geometry of a third generation CT scanner where the x-ray tube and detector array rotate together around the patient. The x-ray tube generates a fan beam of x-rays with incident intensity I_o which are incident on the detector array with intensity I. 9

Figure 2.2 Comparison of simulated dose distributions in the head resulting from projection radiography (irradiation from above) and a 360° CT scan. Values indicated are the relative dose normalized to the surface dose. 16

Figure 2.3 Left: Irradiation geometry in CT for a thin slice through a cylindrical phantom. Right: The longitudinal (z-axis) dose profile between points A-B at a point (x, y) in the scan plane. 17

Figure 2.4 Conventional PMMA (acrylic) "CTDI" phantoms used for CT dosimetry. These are 14 cm long, and 16 cm and 32 cm in diameter to represent the size of an average adult human head and body respectively. 18

Figure 2.5 Simulated multiple scan dose profile $D_{N,b}(z)$ resulting from the superposition of $N = 9$ single slice dose profiles $f(z)$ of nominal width T separated by an interval b. Also indicated is the multiple scan average dose (MSAD). . 20

Figure 2.6 Illustration of the CTDI concept: The area under the SSDP $f(z)$ is equivalent to the area of the rectangular region of base T and height (dose) equal to the CTDI. 22

Figure 2.7 Schematic of a PMMA rod designed to hold an array of TLDs for measuring a SSDP in the CTDI phantoms. TLDs are stacked face to face in the central region for high sampling of the SSDP peak and are typically spaced at 3 mm intervals for the scatter tail regions of the SSDP. Re-created from AAPM (1993). 27

Figure 2.8 Instantaneous dose rate profile along the central axis of a cylindrical phantom moving at constant velocity ν for a helical scan. 37

Figure 2.9 The SSDP $f(z)$ convolved with a rectangular function representing the helical scan length L to produce the accumulated dose distribution $D(z)$. 38

Figure 3.1 Detector elements in the adaptive array of the MX8000 multi-slice scanner. Also shown is an example configuration of the detector collimator for a 1×4 mm slice selection. 56

Figure 3.2 Detectors used in this study (from top to bottom): Wellhöfer IC-10 ionization chamber, PTW diamond detector, Capintec PC-4P pencil ionization chamber and lithium fluoride (LiF) thermoluminescent dosimeters (TLDs). . . 57

Figure 3.3 Schematic of a PTW diamond detector. 59

Figure 3.4 Basic outline of the charged particle detection mechanism of in a diamond detector. 60

Figure 3.5 Schematic of the Wellhöfer IC-10 ion chamber used in this study for verification of the SSDP measured with the diamond detector, and for measuring accumulated dose. 64

Figure 3.6 CIRS homogeneous plastic water phantom used in this study. 66

Figure 3.7 Schematic of the detector rods manufactured in house to be inserted into the PMMA CTDI phantoms for an IC-10 ion chamber and PTW diamond detector. All dimensions are in mm. 68

Figure 3.8 Experimental setup of the CIRS phantom and the PQ5000 CT scanner. The diamond detector is inserted along the central axis of the phantom. 69

Figure 3.9 Illustration of the method used to measure a SSDP. The PTW diamond detector, at a position in the phantom corresponding to $z = 0$ of the profile, translates through the CT beam rotating at a fixed z position and measures the primary and scattered radiation at each z location. 71

Figure 3.10 Lucite 12.7 cm diameter circular tray for holding TLDs, inserted into a $25 \times 25 \times 0.64$ cm^3 sheet of lucite (white), used for the normalization of individual TLD chip sensitivities using the Pantak x-ray unit. 74

Figure 3.11 Experimental setup of the TLDs for normalizing chips sensitivities using the Pantak orthovoltage x-ray unit. . 74

Figure 3.12 Plastic water TLD rods for insertion into the CIRS phantom. TLDs are placed on edge in the rod cavities and spaced apart using plastic water plugs. 75

Figure 3.13 Approximate positions of the detectors within the CIRS phantom for measurements along the central axis. . . . 82

Figure 4.1 Relative energy response curves for the Wellhöfer IC-10 and Capintec PC-4P ionization chambers, and the PTW diamond detector (inset), normalized to an effective energy of 59 keV (approximate effective energy of the CT beams). 89

Figure 4.2 Relative SSDPs along the central axis of the CIRS phantom for the PQ5000 single-slice CT scanner for 3, 5 and 10 mm nominal slice widths (a) and for the MX8000 Quad multi-slice CT scanner for 1×4, 1×10 and 1×20 mm slice settings (b), measured using a PTW diamond detector. The curves through the 10 mm (a) and 1×20 mm (b) profiles are analytic fits (see Eq. (4.6)). 91

Figure 4.3 Extent and causes of the slight asymmetry when measuring SSDPs with the diamond detector in the CIRS phantom. The PQ-10 SSDP is used here as an example. 95

Figure 4.3 Extent and causes of the slight asymmetry when measuring SSDPs with the diamond detector in the CIRS phantom. The PQ-10 SSDP is used here as an example. 96

Figure 4.4 Comparison of the SSDPs along the central axis and off-axis position 2 (see Fig. 3.6(b)) of the CIRS phantom for the PQ5000 scanner, 10 mm slice width. (a) Readings are electrometer units ($\propto$ charge) per 100 mAs (b) Relative to the peak doses. 98

Figure 4.5 Comparison of the central axis SSDP in the CIRS phantom measured using the PTW diamond detector, IC-10 ion chamber and LiF TLDs (TLD-100) for the PQ5000, 10 mm slice width. 99

Figure 4.6 Comparison of the central axis SSDP measured in one half (15 cm) and full (30 cm) CIRS phantom for the PQ5000 scanner, 10 mm slice width. 100

Figure 4.7 SSDPs in the body (a) and head (b) CTDI phantoms for nominal slice widths of 5 and 3 mm respectively, PQ5000 CT scanner. 101

Figure 4.8 Cumulative dose $D_L(z)$ along the central axis of the CIRS phantom, normalized to the equilibrium dose at the center of the scan series $D_{eq}(0)$, generated using convolutions of the symmetrized SSDP for various scan lengths (in mm) for the PQ5000 scanner, 10 mm slice width. 102

Figure 4.9 Predicted ratios of the maximum to equilibrium central axis dose in the CIRS phantom at the center of the scan series of various lengths, for the PQ5000 (a) and MX8000 (b) scanners. The legends state the nominal slice widths (a) and the slice settings in single slice mode (b). . . . 104

Figure 4.10 Simulated effects of detector (volume) averaging (helical and axial mode) and a 4 mm sampling interval (axial mode) on measuring the PQ-10 SSDP with the IC-10 ion chamber. 105

Figure 4.11 Definition of the geometry of an elliptical phantom translating through a CT scanner (z direction) in terms of the center (C) of the phantom and the eccentric/source angle θ. The semi-major and semi-minor axes are denoted as a and c respectively and r is the distance from the phantom center to its surface. 107

Figure 4.12 Simulated relative intensity of photons reaching the center of elliptical (oscillating curve) and cylindrical (horizontal line) plastic water phantoms as a function of z position for a helical scan series. 108

Figure 4.13 Simulated accumulated dose $D_L(z)$ at the center of a elliptical plastic water phantom compared to a cylindrical phantom with an equivalent effective attenuation radius (marked "average"). The oscillating curves are for starting angles of the source 90° out of phase to show the maximum deviation in $D_L(0)$. 109

List of Symbols

b	Axial scan interval
CT	Computed Tomography
CTDI	Computed Tomography Dose Index
CTDI_{100}	CTDI integrated over 100 mm
CTDI_{14T}	CTDI integrated over 14 times the nominal slice thickness T
CTDI_{FDA}	CTDI as defined by the FDA
CTDI_{w}	Weighted CTDI
$D_{eq}(0)$	Equilibrium dose at the center of a scan series of length L
$D_L(0)$	Cumulative Dose at the center of a scan series of length L
$D_L(z)$	Cumulative Dose for a scan of length L
DLI	Dose Line Integral
DLP	Dose Length Product
FDA	Food and Drug Administration
FSD	Focus to Surface Distance
FWHM	Full-Width at Half-Maximum
FWTM	Full-Width at Tenth-Maximum
$f(z)$	Single scan dose profile (SSDP)
cGy or mGy	Centigray or Milligray
HVL	Half Value Layer
I	Slice (image) Index
kVp	Kilovoltage Peak
L	Scan Length
LiF	Lithium Fluoride
mA	X-ray tube current (milliamperes)
mAs	Tube current-time product
MSAD	Multiple Scan Average Dose

MU	Monitor Unit
MV	MegaVolts
μ	Linear attenuation coefficient
n	Number of simultaneously reconstructed slices for a multi-slice scanner
N	Number of axial scans in a series
N_X	Exposure calibration factor
ν	Couch speed
$\nu\tau$	Table advance per rotation
P	Pitch
PMMA	Polymethyl Methacrylate
SSDP	Single Scan Dose Profile
SSP	Slice Sensitivity Profile
T	Nominal slice width
τ	Time for one rotation of the x-ray source
TLD	Thermoluminescent Dosimeter
Z	Atomic number
Z_{eff}	Effective atomic number

Chapter 1

Thesis Overview

Introduction

It is well known that computed tomography (CT) is a relatively high-dose radiological procedure. Though it represents only about 11% of radiology exams in the U.S., CT is estimated to contribute up to 67% of the total effective dose (Mettler et al., 2000). Therefore one should report the dose received by every patient resulting from a CT procedure as accurately as possible. Accurate measurement of CT dose as a function of the operating parameters will aid in risk-benefit analysis of the radiological exam. Several methods for quantifying CT dose have been developed (see Sec. 2.3) but the traditional and most widely used method involves the computed tomography dose index (CTDI) concept (Jucius and Kambic, 1977; Shope et al., 1981). CTDI measurements are typically made using a long (10 cm) pencil ionization chamber which integrates the longitudinal single scan dose profile (SSDP) using a single axial scan (Jucius and Kambic, 1977; Suzuki and Suzuki, 1978). Therefore, CTDI represents the accumulated dose due to a long series of CT scans. However, the major assumption in practical measurement of CTDI is that most of the profile is contained within the active length of the detector and the chamber reading is therefore an accurate representation of multiple scan average dose (MSAD) at the center of a series of contiguous scans. This assumption may not always be valid, even for small slice widths.

Several methods have been described for measuring SSDPs including radiographic film and small volume ion chambers (Dixon and Ekstrand, 1978; Shope et al., 1982), but by far the most common method is using thermoluminescent dosimeters (TLDs) in cylindrical PMMA (lucite) phantoms (AAPM,

1993). There are some drawbacks to this method however. A large number of TLDs are required to measure a SSDP and the spatial resolution is constrained by the thickness of an individual TLD chip ($\sim$ 1 mm). This limit on the maximum attainable resolution potentially leads to inadequate sampling of the peak and penumbral regions of the SSDP, especially for small slice widths. Additionally, large amounts of care and time are required to produce accurate and precise results, limiting the use of TLDs for routine measurement of SSDPs. A potential alternative for SSDP measurement is the use of diamond detectors that have become popular for small-field dosimetry (Laub and Wong, 2003). Diamond detectors exhibit very good spatial resolution ($0.1-0.4$ mm when oriented perpendicular to the beam), high sensitivity, low leakage current and high radiation resistance (Planskoy, 1980), making them suitable detectors for measuring CT dose profiles.

Typical CT phantoms are only 15 cm long in part due to the assumption that the dose in the scatter tails of the SSDP falls approximately to zero within the dimensions of the phantom. This assumption may be true only near the phantom surface for a body phantom (32 cm diameter) and approximately holds at several positions in a head phantom (16 cm diameter) where the scatter to primary ratio is relatively low. An accurate measurement of the SSDP at large distances from the scan center is desirable to test the validity of measuring the CTDI using 10 cm long pencil chambers, especially along the central axis of a trunk phantom. With the wider radiation slice widths available on multi-slice scanners, designed as such to achieve similar noise properties in outer and central slices, the scatter tails in SSDPs are likely to be significant at larger distances. Therefore, a 10 cm long pencil chamber may not be able to encompass the entire SSDP. In these cases, it may be more accurate to use a small volume ionization chamber and multiple rotations to correctly include the longer scatter tails in the dose measurements. Furthermore, since there is no currently accepted method for directly measuring the dose from a helical scan series using ion chambers, a small volume chamber method may be useful. Although the dependence of phantom diameter on the CTDI has been studied (Nickoloff et al., 2003; Avilés Lucas et al., 2004) the effect of the length and composition of the phantom used to acquire the SSDP (and therefore the value of the CTDI) has not been investigated. Phantoms constructed from PMMA, with densities 19% greater than water, are adequate for measuring CTDI as a characterization of the output for a particular CT scanner. They

do not, however, give a realistic estimation of the patient dose due to the difference in the medium that is attenuating the CT beam.

Formulations of the dose from a series of CT scans, expressed as the convolution of a SSDP and a rectangular function of width equal to the scan length, have recently appeared in the literature (Dixon, 2003; Boone et al., 2000). Dixon (2003) highlighted that the equilibrium dose from an axial or helical scan series is a function of the width (and shape) of the SSDP, the scan length, and the distance between adjacent scans. A method of measuring this dose at any point along the scan series, for any scan length (whether equilibrium is reached or not), using a small volume ion chamber was also suggested and briefly validated experimentally in standard CT phantoms for a 150 mm scan length. Dixon stated that integrating the dose over a 100 mm scan length should result in the same dose measured using a 10 cm pencil chamber. An experimental verification of this method is required.

In this work, the use of a commercially available diamond detector (PTW Riga Type 60003) to measure SSDPs in CT was explored. To better estimate the longitudinal extent of the SSDP in a real patient, a water-equivalent phantom (CIRS Model 002H5), twice as long as the acrylic phantoms commonly used in CT, was utilized. From numeric integration of the SSDPs and through convolution methods, the accumulated dose from axial and helical scan series was predicted for scan lengths up to 25 cm, and these predictions were tested by measuring the integral dose with a small volume ionization chamber (Wellhöfer IC-10).

This thesis is organized in the following chapters.

Chapter 2: Background

An overview of the relevant background material to the thesis is presented in Chapter 2. The topics include a basic overview of CT scanning (basic operation, scanner types, relevant terminology, main applications), a discussion of the relationship between dose and image quality in CT, an overview of the dose quantities appropriate for CT, a description of the methods currently used for measuring CT dose , and the equipment- and application-related factors that influence the patient dose in CT. A formalism for measuring the integral dose recently introduced (Dixon, 2003) is presented in greater detail since one of the goals of this work was experimental verification of this formalism.

Chapter 3: Materials and Methods

Chapter 3 is a description of the material and methods used in this experimental investigation of CT dosimetry. The main operating parameters of the two CT systems utilized for this work are described, with emphasis on the technique parameters that affect the patient dose. All the dosimeters used for measuring absolute and relative dose are described and their preferential use over other potential dosimeters is justified when applicable. This discussion includes a more detailed description of a PTW Riga Type 60003 diamond detector used for relative SSDP measurements since the use of diamond detectors for CT dosimetry is new. Also included in this chapter are brief descriptions of each of the phantoms used for dose measurements. The method of measuring relative SSDPs in the phantoms using the PTW diamond detector is presented in detail. In addition, the methods for measuring one representative SSDP using a small volume ion chamber and TLDs, used for verification of the diamond-measured SSDP, are described. A description of the methods used for absolute dose measurements using the small volume chamber and a pencil ion chamber in a long plastic-water is given. This includes discussions of the method of calibrating the chambers for absolute dose measurements, determination of the energy response characteristics of the ion chambers and diamond detector, and finally the actual integral dose measurements.

Chapter 4: Results

In Chapter 4, the results of several experiments are presented including the energy response curves of the dosimeters and the SSDPs measured using the diamond detector in the plastic-water and PMMA CT phantoms. Observations and explanations regarding the measured SSDPs are given including the extended scatter tails and asymmetries due to the measurement method. SSDPs are numerically integrated to predict the accumulated dose and are fit with an empirically derived analytic function. Several other results are presented including the effects on the measured SSDP due to differences in the length and composition of the phantom and the dosimeter used for measurement. Simple theoretical discussions of the potential errors inherently introduced in the measured absolute integral dose with a small volume chamber when scanning in axial and helical modes are developed. Chapter 4 closes with the tabulated absolute integral doses measured using the small volume and pencil ion

chambers.

Chapter 5: Conclusions

The thesis closes with Chapter 5 which restates the major results presented in Chapter 4 and provides concluding remarks and recommendations based on this experimental investigation of CT dosimetry.

Chapter 1 References

AAPM (1993). Task group 2: Diagnostic x-ray imaging, report no. 39: Specification and acceptance testing of computed tomography scanners. Technical report, American Institute of Physics.

Avilés Lucas, P., Dance, D. R., Castellano, I. A., and Vañó, E. (2004). Monte Carlo simulations in CT for the study of the surface air kerma and energy imparted to phantoms of varying size and position. *Phys. Med. Biol.*, 49:1439–1454.

Boone, J. M., Cooper III, V. N., Nemzek, W. R., McGahan, J. P., and Seibert, J. A. (2000). Monte carlo assessment of computed tomography dose to tissue adjacent to the scanned volume. *Med. Phys.*, 27(10):2393–407.

Dixon, R. L. (2003). A new look at CT dose measurement: Beyond CTDI. *Med. Phys.*, 30(6):1272–1280.

Dixon, R. L. and Ekstrand, E. E. (1978). A film dosimetry system for use in computed tomography. *Radiology*, 127:255–258.

Jucius, R. A. and Kambic, G. X. (1977). Radiation dosimetry in computed tomography. *Proc. SPIE*, 127:286–295.

Laub, W. U. and Wong, T. (2003). The volume effect of detectors in the dosimetry of small fields used in IMRT. *Med. Phys.*, 30(3):341–7.

Mettler, F. A., J., Wiest, P. W., Locken, J. A., and Kelsey, C. A. (2000). CT scanning: Patterns of use and dose. *J. Radiol. Prot.*, 20(4):353–9.

Nickoloff, E. L., Dutta, A. K., and Lu, Z. F. (2003). Influence of phantom diameter, kVp and scan mode upon computed tomography dose index. *Med. Phys.*, 30(3):395–402.

Planskoy, B. (1980). Evaluation of diamond radiation dosemeters. *Phys. Med. Biol.*, 25(3):519–32.

Shope, T. B., Gagne, R. M., and Johnson, G. C. (1981). A method for describing the doses delivered by transmission x-ray computed tomography. *Med. Phys.*, 8(4):488–495.

Shope, T. B., Morgan, T. J., Showalter, C. K., Pentlow, K. S., Rothenberg, L. N., White, D. R., and Speller, R. D. (1982). Radiation dosimetry survey of computed tomography systems from ten manufacturers. *Br. J. Radiol.*, 55(649):60–9.

Suzuki, A. and Suzuki, M. N. (1978). Use of a pencil-shaped ionization chamber for measurement of exposure resulting from a computed tomography scan. *Med. Phys.*, 5(6):536–9.

Chapter 2

Background

2.1 Basics of CT

X-ray computed tomography (CT) is the process of creating two dimensional cross sectional images or tomograms of a three dimensional object using projections (line integrals) of the object at many angles measured by the transmission of x-rays. The projection data is then reconstructed on a computer. The mathematical foundations of CT were derived as far back as 1917 by J. H. Radon (Radon, 1986) but the possible medical applications of the theory were not realized at the time. The first clinical CT scanner was manufactured in 1972 by G. N. Hounsfield who independently developed the mathematical background for image reconstruction in the 1970's (Hounsfield, 1973).

In the following sections, a very basic overview of the theory, history and terminology of CT that is relevant to the experimental work presented in this thesis will be given. Much of the information is summarized from Kalendar (2000); Bushberg et al. (2002); Goldman and Fowlkes (1995); Van Dyk (1999).

2.1.1 Elementary Theory of Image Formation

Most modern scanners consist of a x-ray tube (operating between 80 kVp and 140 kVp) rotating in the $x - y$ or transverse plane on a gantry, and a couch which translates the patient through the gantry in the longitudinal (z) direction as shown in Fig. 2.1 for a third generation scanner (Sec. 2.1.2.3). A (diverging) fan beam of x-rays in the $x-y$ plane is produced which is collimated in the z direction to define the beam width. The fan beam, after passing through the patient, is incident on either a single linear array of detectors

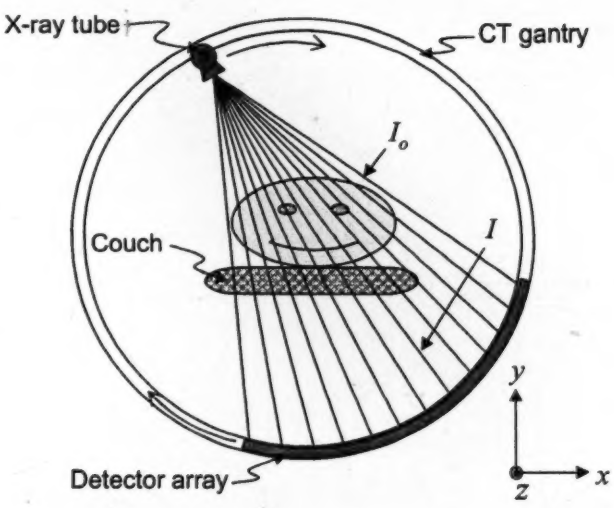

Figure 2.1: General configuration of the major components and geometry of a third generation CT scanner where the x-ray tube and detector array rotate together around the patient. The x-ray tube generates a fan beam of x-rays with incident intensity I_o which are incident on the detector array with intensity I.

(single slice scanners) or on multiple rows of detector arrays abutted together in the z direction (multiple slice scanners). Only a fraction of x-rays scattered in the fan beam plane are detected due to the focussed detector septa; those photons scattered in the z direction beyond the total width of detectors are completely rejected. Assuming monochromatic x-rays, the transmission of x-rays along a single ray in the fan beam through a heterogeneous object (such as the human body) of total thickness d is given by

$$I = I_o e^{-\int_d \mu \, dt} \tag{2.1}$$

where I and I_o are the intensities of transmitted and incident x-rays respectively, μ is the linear attenuation coefficient and dt is the path length element. The measurable quantities are I and I_o, and Eq. (2.1) can be rearranged as

$$\ln(I_o/I) = \int_d \mu(x, y) \, dt \tag{2.2}$$

in order to estimate the line integral of the $\mu(x, y)$ values along a given ray using a single transmission measurement. By using many rotations of the x-ray source, thus creating many sets of projection data at numerous angles,

it is possible to estimate the distribution $\mu(x, y)$ by essentially inverting the set of equations (2.2). The most common approach to the inversion process involves filtering the projection data and then backprojecting onto a digital matrix to form a pixel map or image. In reality of course, CT beams are polyenergetic and the average energy of the beam increases with depth in the patient. This beam hardening introduces image artifacts that are reduced in most CT scanners by using a bow-tie filter, and further corrected in software by using several beam-hardening correction algorithms. A comprehensive description of the theoretical aspects of CT image acquisition and reconstruction is beyond the scope of this thesis (which focuses on the dose from CT) and is described in detail in several text books including Herman (1980) for example.

Since values of $\mu(x, y)$ are highly dependent on the spectral energy of the beam, quantitative comparison between images taken at different kVp or on different systems is difficult. Therefore for display purposes, attenuation coefficients are normalized to that of water μ_w and referred to as CT numbers in Hounsfield units (HU),

$$CT\# = \frac{\mu(x, y) - \mu_w}{\mu_w} \cdot 1000 \text{ HU}. \tag{2.3}$$

Thus the CT number of water is 0 HU by definition.

2.1.2 CT Scanner Generations and Developments

The development and evolution of CT scanner technology is commonly broken down into scanner "generations", with each generation describing a different x-ray beam and detector geometry for acquiring the tomographic transmission data. These scanner generations and developments such as helical scanning and multi-slice acquisition are described below.

2.1.2.1 First Generation

The first generation of CT scanners consisted of a pencil-beam of x-rays and one or two detectors, operating as a translate/rotate system. In Hounsfield's first commercially available scanner, the source and detector(s) linearly translated together laterally across the patient in 160 steps, generating parallel projection data at a fixed angle (Kalendar, 2000). The source and detector were then rotated by a small angle (1°) and the process was repeated for 180°

coverage in order to form a single 13 mm thick tomographic slice. Although the pencil-beam geometry of first generation scanners provided reduced radiation scattering and very efficient rejection of the amount of scatter detected, scan times were long, especially for large body scans. The long scan times (5 minutes per rotation and 35 minutes for a complete exam) also lead to artifacts in the images due to patient motion and breathing.

2.1.2.2 Second Generation

As opposed to the pencil-geometry of the first generation scanners, a narrow ($\sim 10°$) x-ray fan beam and a single linear array of about 30 detectors were incorporated into the second generation scanners. The z-extent or slice thickness of the fan beam was limited by collimation near the source. Since the fan angle was not large enough to encompass the entire patient cross section, the x-ray source still had to translate laterally across the patient at a fixed angle and the process was repeated over several angles (but fewer than the first generation system). Thus second generation scanners were also translate/rotate systems. Scan times were shorter (20 s per scan) than the first generation scanners due to the fan beam but more scattered radiation was produced and detected in the plane of the detector array.

2.1.2.3 Third Generation

Due to the limitation on scan speeds of the first and second generation scanners, widespread clinical implementation of CT scanners was not fully realized until the introduction of third generation scanners. Third generation systems employ a wide fan beam, wide enough to at least cover the entire patient cross section, incident on an array of hundreds of detectors focussed onto the source on the opposite side of the patient. This eliminated the transverse translational motion of the source seen in earlier generations. The source and detector array rotate together (i.e., a "rotate/rotate" system) around the patient. The scan times of third generation scanners were substantially shorter than previous generations, with 360° coverage for a single slice acquisition obtained in the order of seconds.

2.1.2.4 Fourth Generation

Fourth generation scanners utilize a *fixed* detector array around the entire 360° of the CT gantry. The x-ray tube still forms a fan beam, but the tube now rotates around the gantry inside of the fixed detector array. Fourth generation scanners were introduced to overcome the problem of ring artifacts in images from third generation scanners which were due to miscalibrated detectors or due to the non-uniformity of detector response in the array.

2.1.2.5 Fifth Generation

Fifth generation scanners (also known as ciné, ultrafast or electron beam) do not utilize any mechanically moving parts in the gantry but instead use a scanning electron beam incident on tungsten anodes situated at various points around the gantry. A fan beam of x-rays is generated at the point of interaction and are detected on the opposite side of the gantry using a stationary ring of detectors. Because there are no moving parts, scan times on fifth generation systems are very fast (msec) and are used primarily for cardiac imaging to reduce motion artifacts. In the previous decade, a significant development in ultrafast multi-slice helical CT scanners have reduced overall scan times. The cardiac motion artifact is overcome by applying cardiac gating techniques (Kachelriess et al., 2000). For this reason, fifth generation systems are no longer considered for use in the clinic.

2.1.2.6 Axial Scan Mode

All scanning systems discussed thus far initially operated only in axial mode where the projection data is collected over several angles at a fixed z location in planar geometry. After scanning a single slice with the patient stationary, the couch is translated in the z direction by an increment known as the scan interval b. Image reconstruction is only possible at the discrete z positions chosen at the time of acquisition and therefore the sampling interval in the z direction is determined by b. Although the choice of b is arbitrary, the most common choice is an amount equivalent to the nominal slice width, i.e, contiguous scanning. In axial scanning, the distance between reconstructed images or the index I is equivalent to the scan interval.

The nominal slice width T is defined as the full-width at half-maximum (FWHM) of the slice sensitivity profile (SSP) (FDA, 2003). The SSP is a

graphical representation of the system's response on a line perpendicular to the scan plane (z direction) to an attenuating impulse object. For axial scanning, the SSP is typically measured using a "ramp phantom" where a thin wire or sheet of metal is inclined at an angle to the z-axis. The image of the ramp then directly constitutes the sensitivity profile. The reader is referred to Suess et al. (1995) for a more thorough description on measuring the SSP. The slice width in a single detector array (single slice) CT system operating in axial mode is determined primarily by the physical beam collimation of the incident x-rays near the source.

2.1.2.7 Helical Volume Scanning

Third and fourth generation scanners when initially introduced were essentially "step and shoot" systems for volume imaging in axial mode, meaning that after each slice was acquired, the gantry had to be stopped and repositioned to the initial (angular) position before translating the couch in the z direction. This was done to avoid entanglement of the cables to the gantry, which typically rotated with the x-ray tube and/or detectors. The so-called "sixth generation" scanners avoided this through the use of slip ring technology which allowed continuous x-ray tube rotation during couch translation in the z direction. This is known as spiral or helical scanning since the path of the x-ray focus relative to the patient is helical (non-planar geometry). Helical scanning greatly reduced total study times for imaging large volumes. All modern scanners incorporate both helical and axial scanning modes but are still referred to as third or fourth generation scanners depending on the arrangement of the source and detectors.

Unlike axial scanning, planar slices (images) can be reconstructed at any z location in helical mode through interpolation of the non-planar helical data ("z-interpolation"). Therefore the choice of index I is arbitrary and can be retrospective. For helical scanning, in addition to collimation, the slice width T also depends on the z-interpolation algorithm used for reconstruction. This is because the interpolation, in addition to the table motion, tends to broaden the SSP compared to a conventional axial slice. For measuring the SSP in helical scanning, delta impulse objects such as tiny high density spheres (i.e., infinitesimal small extent in the z-direction) are employed where the maximum CT number of the bead in each of a series of closely-spaced reconstructed slices is recorded (Suess et al., 1995) and displayed as the SSP as a function of slice

location in the series.

The advent of helical scanning required the introduction of new terminology, one of which is the concept of the pitch factor or pitch P. For a single slice scanner (single detector array), the pitch of a helical scan is defined as

$$P \doteq \frac{\text{table advance per 360° source rotation}}{T}. \tag{2.4}$$

A value of $P = 1$ implies contiguous scanning while $P < 1$ indicates overlapping scans.

2.1.2.8 Multiple Slice Systems

Traditional single slice CT systems use relatively wide detectors (z direction) in the linear array and the slice width is determined primarily by the adjustable source collimators (up to the detector width). In multiple slice scanners, many linear detector arrays are abutted together in the z direction, making possible the acquisition of many imaged slices during one rotation of the source. The slice width is set using the source collimation, adjustable collimators directly in front to the detectors, and electronic binning of detectors in the z direction for beams wider than the pitch of each detector. Multi-slice scanners commercially available can reconstruct from 4 to 64 slices per rotation in axial mode, greatly reducing scan times compared to equivalent single slice systems when imaging large volumes of the body.

Multi-slice scanning in helical mode requires a slight modification of the definition of pitch since the width of the x-ray beam is not necessarily equivalent to the *reconstructed* slice width as in single slice scanners. For example, a scanner with four detectors rows and a total z-extent of 20 mm may produce four 5 mm thick slices. The common notation used in multi-slice CT for this slice selection would be 4×5 mm. For this thesis, the definition of pitch that will be used is

$$P = \frac{\text{table advance per 360° source rotation}}{\text{beam width}} \tag{2.5}$$

$$= \frac{\text{table advance per 360° source rotation}}{nT} \tag{2.6}$$

where n is the number of reconstructed slices of nominal width T. This definition of pitch, commonly referred to in the literature as "collimator pitch", reduces to that for single slice scanners (Eq. (2.4)) with $n = 1$.

2.2 Applications of CT

2.2.1 Diagnosis

CT is widely used as a tool for diagnosis due to its ability to differentiate soft tissue structures such as the lungs, the liver and fat. It offers improved delineation of low-contrast structures over traditional radiography where the three dimensional content of the body is reduced to a projection onto a two dimensional image. CT is especially useful in identifying the size, extent and spatial location of lesions which occupy relatively large volumes as well as tumors and metastasis. CT can also be useful for detecting things such as blood clots and blood vessel defects for example. Although the spatial resolution of conventional film projection radiography is superior to CT, contrast resolution in CT is much better than film although not as good as magnetic resonance imaging (MRI).

2.2.2 Radiotherapy Treatment Planning

CT images also form the basis for radiation therapy in cancer. This is usually carried out using a CT simulator, which is a combination of a standard diagnostic CT scanner, a laser localization system for alignment of the patient in the treatment position, as well as a workstation for image manipulation, delineation of normal tissues, and delineation and contouring of tumor volumes. The attenuation coefficient data in CT images can be converted relatively easily to relative electron densities which can then be sent to a computer treatment planning system (since the data is already in a digital format) to calculate the dose to a target volume and surrounding healthy structures.

2.3 Radiation Dose from CT

2.3.1 Dose Distributions

2.3.1.1 Scan Plane

In conventional projection radiography, the dose from the absorption of primary and scattered photons in the irradiated object decreases roughly exponentially from the beam entrance to the exit side of the object. In CT, the

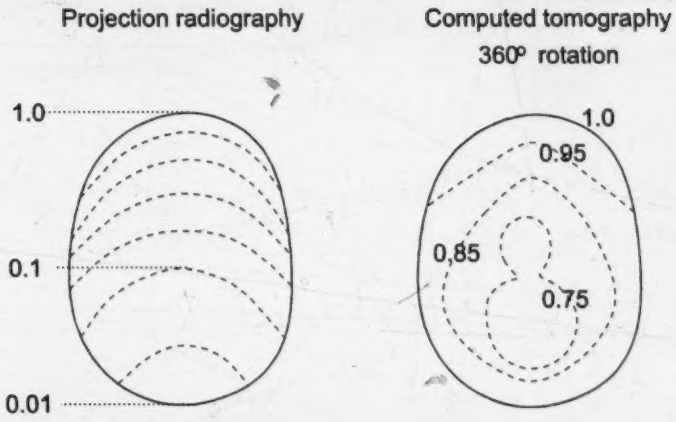

Figure 2.2: Comparison of simulated dose distributions in the head resulting from projection radiography (irradiation from above) and a 360° CT scan. Values indicated are the relative dose normalized to the surface dose.

dose from a 360° scan is distributed much more uniformly throughout the scan plane ($x - y$ plane) due to the rotational geometry of the CT scanning process. This is illustrated in Fig. 2.2 for a simulated dose distribution for a head CT scan and a 360° rotation of the x-ray source. The maximum variations in dose with depth are about a factor of two for a 360° scan and not orders of magnitude (Kalendar, 2000). Jucius and Kambic (1977) measured the dose distribution in the scan plane using TLDs (for the peak dose from a single scan) and a 10 cm long pencil ion chamber (for the multiple scan average dose (MSAD); see Sec. 2.3.3) in 21.6 cm diameter lucite phantoms. They found that for a 360° scan (with a slight overscan) at 130 kVp, the peak dose from a single 7 mm wide scan at the center of the phantom was about 15% of the surface peak dose. At the position of the central scan of a series, they found the MSAD at the phantom center to be about 55% of the surface MSAD. This was significantly less variation of dose with depth than for the peak dose due to the larger contribution of out of plane scatter in a multiple scan series (discussed in Sec. 2.3.3). In a Monte Carlo study of CT doses using a 5 mm slice width and 16 cm long cylindrical phantoms of various materials, Atherton and Huda (1995) found essentially no change with radial position in the MSAD for 80 keV photons in 16 cm diameter acrylic and water phantoms (which approximate the size of the human head). For 32 cm diameter acrylic and water phantoms (to simulate the human body), they determined the surface MSAD to be approximately twice that at the phantom center. A linear

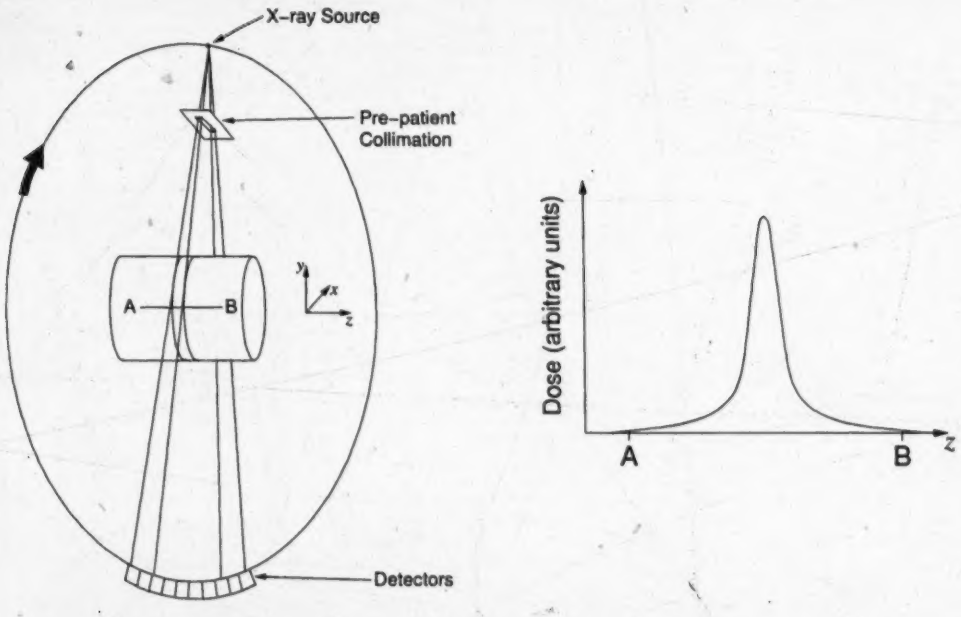

Figure 2.3: Left: Irradiation geometry in CT for a thin slice through a cylindrical phantom. Right: The longitudinal (z-axis) dose profile between points A-B at a point (x, y) in the scan plane.

decrease of the MSAD from the surface to the center is commonly assumed for cylindrical tissue-like phantoms in order to calculate an average MSAD in the entire scan plane (Leitz et al., 1995). This is done by measuring the MSAD at the center and periphery of the phantoms and computing a weighted average (see Sec. 2.3.6.3).

2.3.1.2 Longitudinal Axis

Another fundamental difference between projection radiography and CT is that images in CT consist of thin transverse slices through the patient. However, the energy deposited in the patient during a single CT scan is not confined to the directly irradiated slice, but extends to the adjacent volume as well. This is primarily due to the wide angle Compton scattering within the patient and, to a lesser extent, beam penumbra and divergence of the beam from the x-ray source. The irradiation geometry for a single axial slice of a cylindrical phantom is illustrated on the left side of Fig. 2.3, with the resulting longitudinal (z) dose distribution (perpendicular to the scan plane) at a point (x, y) in the phantom shown on the right. This is known as the single

scan dose profile (SSDP) or $f(z)$. In the absence of any detector collimation, the nominal slice width is approximately equal to the FWHM of the SSDP assuming the phantom central axis and scanner rotational axis coincide.

2.3.2 CT Phantoms

2.3.2.1 Cylindrical PMMA Phantoms

The phantoms traditionally used for measuring many of the dose quantities to be described in this chapter are constructed from polymethyl-methacrylate (PMMA) which is also known as acrylic, lucite, perspex or Plexiglas^{TM}. PMMA has a density of 1.19 g/cm^3 (Berger et al., 1998) and an effective atomic number $Z_{eff} = 6.6$ (Khan, 1994). PMMA CT phantoms are right circular cylinders, at least 14 cm in length and are typically manufactured in both 16 cm and 32 cm diameters to represent the sizes of an average adult human head and body respectively. Figure 2.4 shows the 14 cm long head and body phantoms constructed in our department. The head phantom is also sometimes used to estimate pediatric body doses. Holes, typically $1-2$ cm in diameter and the length of the phantom, are drilled parallel to the phantom (central) axis at various radial positions to accommodate the insertion of dosimeters such as ion chambers, film or TLDs. Dosimeters are held in place in rods designed

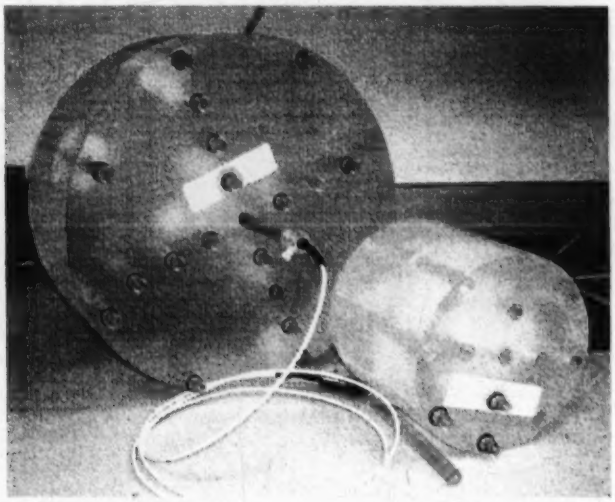

Figure 2.4: Conventional PMMA (acrylic) "CTDI" phantoms used for CT dosimetry. These are 14 cm long, and 16 cm and 32 cm in diameter to represent the size of an average adult human head and body respectively.

to fit snugly into the holes. Thus the dose and/or dose distributions in the scan plane and along the longitudinal (z) axis can be measured. Although the radial positions of the holes are arbitrary, most phantoms have holes at the center and at the azimuthal positions corresponding to 3, 6, 9 and 12 o'clock at a depth of 1 cm. A pencil ion chamber (discussed in greater detail in Sec. 2.3.5.3) is shown partially inserted at the body phantom center in Fig. 2.4. Holes that are not used during dose measurements are plugged with solid PMMA rods to maintain a nearly homogeneous phantom. These phantoms are readily available commercially and are often referred to as "CTDI" phantoms since they are standard for measuring the computed tomography dose index or CTDI (see Sec. 2.3.4). Since the FDA in the United States requires CT manufacturers to report the dose values using PMMA phantoms (see Sec. 2.3.6.1), these phantom dimensions are specified in FDA (2003) and have therefore become standard for CT dosimetry.

The PMMA CTDI phantoms are traditionally assumed to approximately simulate the scattering conditions in a real patient undergoing a CT examination. This approximation is true at megavoltage energies used in radiation therapy since the dominant interaction is the Compton effect where the interaction cross section is proportional to electron density. The electron densities of PMMA and soft tissue are both approximately 3.3×10^{26} e/kg (Khan, 1994). The patient-like approximation of PMMA at kilovoltage (i.e., CT) energies may not hold however due to increased photoelectric interactions, which are strongly dependent on atomic number. The effective atomic number of soft tissue is 7.4 (Khan, 1994). This patient-like approximation of CTDI phantoms is one of the assumptions of conventional CT dosimetry that will be explored in the experimental chapters of this thesis. It is also commonly assumed that the $14 - 15$ cm length of CTDI phantoms is adequate such that the scatter tails of the SSDP for all slice widths fall approximately to zero at the phantom edges. This is discussed in greater detail in the last section of this chapter.

2.3.2.2 Anthropomorphic Phantoms

Anthropomorphic phantoms in general are designed to simulate the shape and internal composition of a section of the human body in its response to high energy radiation. This includes both soft tissue (muscle, organs, etc.) and bony anatomy. For direct application to CT where the Compton effect dominates, the most important consideration is that the CT numbers of the

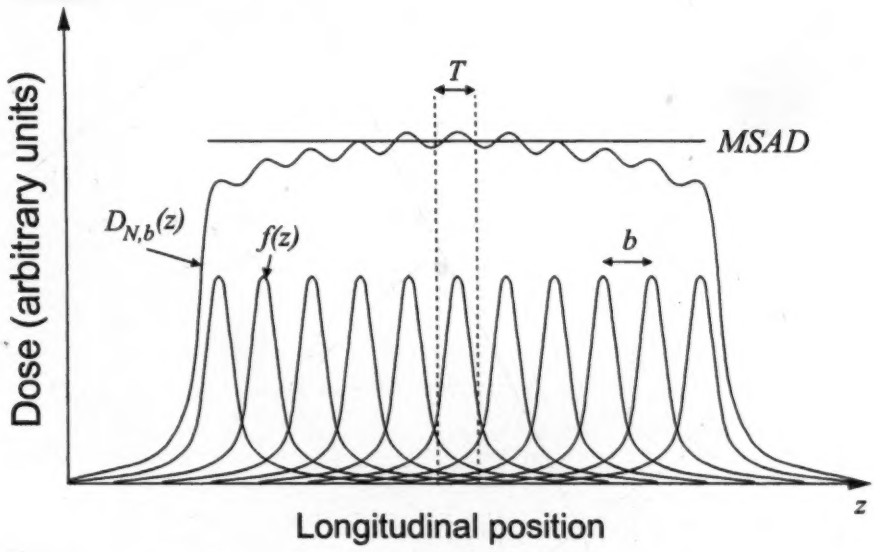

Figure 2.5: Simulated multiple scan dose profile $D_{N,b}(z)$ resulting from the superposition of $N = 9$ single slice dose profiles $f(z)$ of nominal width T separated by an interval b. Also indicated is the multiple scan average dose (MSAD).

phantom's constituents accurately mimic those corresponding to real patient data by having similar electron densities. In other words, the radiographic response in the range of CT energies must be similar to that of the human body. Some phantoms, like the Alderson Rando^{TM}humanoid phantom, are divided into thin ($\sim$ 25 mm) transverse sections. Doses can then be measured directly for organs or tissues of interest by inserting TLDs between the slices for example, and irradiating the phantom in the CT beam.

2.3.3 Multiple Scan Average Dose (MSAD)

Virtually all CT procedures consist of multiple scans distributed along the z axis. Describing the dose for a CT scan series using the peak of the SSDP for example is not entirely meaningful or appropriate. This is because the dose to the region of any one slice will be the sum of the contributions from adjacent slices, due solely to the extended dose profile illustrated in Fig. 2.3. Figure 2.5 illustrates this for $N(= 9)$ axial slices of nominal width T spaced at an interval b. The multiple scan dose profile $D_{N,b}(z)$ builds up from the superposition of

the adjacent slices (SSDPs) as follows for odd N:

$$D_{N,b}(z) = \sum_{n=-(N-1)/2}^{(N-1)/2} f(z - nb). \tag{2.7}$$

As the number of scans increases such that the outer slices no longer contribute significant dose to the region of the central slice, $D_{N,b}(z)$ reaches a maximum or equilibrium value over the region near the central slice. The relationship between b and the SSDP shape determines the spatial frequency and relative magnitude of the fluctuations in $D_{N,b}(z)$. If the SSDPs are narrow (e.g., near the surface of a phantom where the scatter contribution is relatively small compared to that from the primary radiation) or if b is large, the variations in $D_{N,b}(z)$ with z can also be significant. Conversely, for small b and/or wide SSDPs, $D_{N,b}(z)$ can be almost constant or flat over the central region. The multiple scan average dose (MSAD) (Shope et al., 1981) is defined as

$$MSAD = \frac{1}{b} \int_{-b/2}^{b/2} D_{N,b}(z) dz, \tag{2.8}$$

and is indicated in Fig. 2.5. The MSAD at the center of CTDI body phantom for contiguous slices can be four to five times the peak dose due to a single slice (Shope et al., 1982; McGhee and Humphreys, 1994). Generally the MSAD increases for points nearer the phantom surface due to the greater contribution of dose from primary radiation at the shallower depths. The MSAD at the phantom center decreases with the size (diameter) of the phantom (Nickoloff et al., 2003) due to greater attenuation of the primary beam. Increasing the scan interval b will decrease the MSAD and can also create large variations between the peaks and valleys with z of the multiple scan dose profile. However, this occurs only in the (narrow) overlap regions and the dose over the central region of the imaged volume is near the MSAD as seen in Fig. 2.5. Values of the MSAD were reported by Conway et al. (1992) as a summary of the results of the 1990 Nationwide Evaluation of X-ray Trends (NEXT) survey of the radiation dose from a typical adult head procedure. The MSAD, measured at the center of the head CTDI phantom using TLDs, was between 34 and 55 mGy for most of the 252 CT systems surveyed, and reached as high as 140 mGy. This data provides an order of magnitude estimation of the MSAD in general.

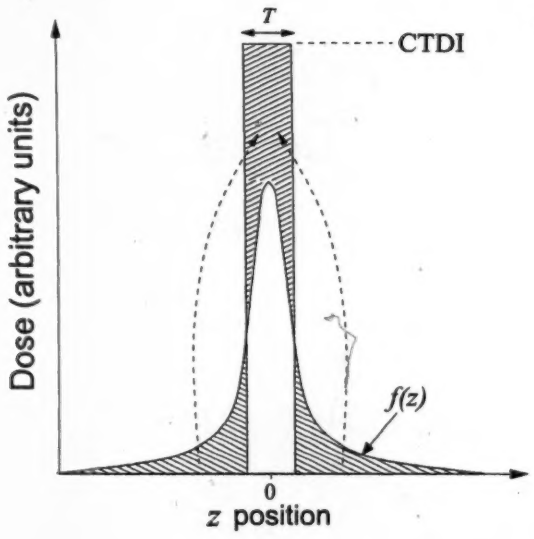

Figure 2.6: Illustration of the CTDI concept: The area under the SSDP $f(z)$ is equivalent to the area of the rectangular region of base T and height (dose) equal to the CTDI.

2.3.4 Computed Tomography Dose Index (CTDI)

Probably the most widely used dose descriptor for an axial scan series in CT is the computed tomography dose index or CTDI (Shope et al., 1981; Jucius and Kambic, 1977). Under the condition that the scan interval is equal to the slice thickness ($b = T$, contiguous scanning) and that the series contains a large enough number of slices such that the first and last slice do not contribute dose to the region T, it can be shown that (Shope et al., 1981) the contribution of dose from slices adjacent to a region T about the central scan of a series is equivalent to the integral of the SSDP over $|z| \geq T/2$. Thus the area under the entire SSDP is equivalent to the area under $D_{N,b}(z)$ over a width T of the central scan,

$$\int_{-\infty}^{\infty} f(z)dz = \int_{-T/2}^{T/2} D_{N,T}(z)dz \tag{2.9}$$

where $D_{N,T}(z)$ is the multiple scan dose profile when $b = T$ and for a large enough N. Defining the CTDI for a point (x, y) in the scan plane as

$$CTDI = \frac{1}{T}\int_{-\infty}^{\infty} f(z)dz, \tag{2.10}$$

the CTDI is equivalent to the MSAD if $b = T$ (Eq. (2.8)). If $b \neq T$, then

$$CTDI = \frac{b}{T} MSAD. \tag{2.11}$$

Figure 2.6 illustrates the meaning of CTDI. If all the dose under the SSDP were confined to a rectangular region equivalent in width to the nominal or directly irradiated slice width, the resulting dose would be equivalent to the value of the CTDI. It is again assumed that the first and last scans of the series contribute no significant dose to the region of the central scan, but how many scans are necessary to fulfill this requirement? Shope et al. (1981) determined the ratio of the MSAD to the CTDI based on measurements at various radial positions in the CTDI body phantom using four CT scanner models. The MSAD was calculated using Eq. (2.8) where $D_{N,b}(z)$ was obtained by the (mathematical) superposition of N SSDPs measured with TLDs. To obtain the CTDI, the SSDPs were fitted using the sum of two Gaussians and then integrated analytically. They found the ratio MSAD/CTDI at the body phantom center to be greater than 0.8 for 12 or more scans but only approached a value of 1 after approximately 20 scans. The ratio approached 1 quicker ($\sim$ 12 scans) near the phantom surface (1 cm depth) than at the center since the surface SSDP was narrower due primarily to less scatter at the shallower depth. For one CT system and using the 16 cm diameter CTDI head phantom, MSAD/CTDI approached 1 within about 10 scans for all radial positions.

One problem with the definition of CTDI has been pointed out by several authors (Spokas, 1982; Dixon, 2003), and that is the inclusion of an imaging parameter (T) in a quantity describing dose. The slice width T in Eq. (2.10) is formally defined by the FDA as the "full-width at half-maximum (FWHM) of the [slice] sensitivity profile taken at the center of the tomographic volume ..." (FDA, 2003). The nominal slice width T then is only representative of the *imaged* volume and has little to do with dose. In general, the dose and slice sensitivity profiles are not equivalent since, by definition, the radiation contributing to dose is absorbed in the patient/phantom and does not reach the detectors to form the image. This is especially true for the more readily absorbed low energy photons which contribute to the formation of the SSDP scatter tails. Therefore the SSP is generally narrower than SSDP. Furthermore, detector collimators (for scatter rejection or slice selection in multi-detector scanners)

may be present, further narrowing the SSP. These factors can combine to create significant differences between the FWHM of the SSPs and SSDPs. For nominal slice widths of 10, 5, 3 and 1 mm on a single slice scanner, McNitt et al. (1999) found +10%, +30%, +30% and +144% differences respectively in the FWHM of the measured SSDPs from the nominal collimation. Oliveira et al. (1995) measured an 11.4 mm FWHM of the SSDP for a nominal slice width of 8 mm. Attempts have been made to eliminate T in the definition of accumulated CT dose. Spokas (1982) proposed that CT dose should be described by two parameters, the maximum value (peak) of the SSDP, D_{max}, and the width of the equivalent rectangular profile given by,

$$w = \frac{1}{D_{max}} \int_{-\infty}^{\infty} f(z)dz. \tag{2.12}$$

Oliveira et al. (1995) kept the CTDI formalism but instead replaced the factor T with the FWHM of the SSDP and denoted the quantity CTDI*. They also introduced the plateau dose D_{plt} given by

$$D_{plt} = \frac{\int_{\text{plateau}} f(z)dz}{\text{plateau}} \tag{2.13}$$

where the plateau is the length of the plateau region of the SSDP. These alternate descriptions of CT dose have not been adopted at large however, possibly due their impracticality for quality assurance in a clinical setting where time and ease of implementation are important factors. The method of Spokas (1982) requires either a SSDP measured with TLD, or two ion chamber measurements: a small chamber for D_{max} and a pencil chamber for the dose line integral. For the method of Oliveira et al. (1995), measuring the SSDP using TLDs is practically a requirement. Additionally, the plateau length for small slice widths becomes somewhat undefined since spatial resolution in measuring the SSDP using TLDs is limited to the 1 mm thickness of an individual TLD chip, thereby averaging the peak over the active length of the TLD. This could be overcome using film with its much higher spatial resolution, but as will be discussed in the next section, the response of film exhibits an appreciable energy dependence at CT energies.

Despite these efforts to modify and potentially improve upon the CTDI concept, the dose from a CT scan series has been quantified using the CTDI for nearly 25 years. The benefit of the CTDI as a practical dose descriptor is

that only a single axial scan is needed for measuring the MSAD, an important consideration in the early days of CT when x-ray source rotation times were slow and the heat capacity of x-ray tube anodes was low.

2.3.5 Measuring MSAD and CTDI

The MSAD can be measured directly by using multiple scans and either an array of thermoluminescent dosimeters (TLDs), or a thin strip of film, aligned parallel to the z-axis in a CTDI phantom (for example). For determination of the CTDI, all that is required is a method to integrate the SSDP. Traditional methods have included measuring the primary and scattered radiation along the z-axis (the SSDP) using film or TLDs and a single axial scan. The CTDI can be calculated by mathematical integration of the SSDP. The most common method, however, is to measure the dose line integral directly using a long pencil ionization chamber and a single axial scan.

2.3.5.1 Film

Film provides the ability to measure the dose at many points simultaneously with high spatial resolution. However, due to the high atomic number (Z) chemicals present in film emulsions, one can expect a large energy-dependent response at CT energies due the high Z dependence of the photoelectric effect as Z^n ($n = 3 - 4$ (Attix, 1986)). Dixon and Ekstrand (1978) explored the use of Kodak XV-2 film for measuring the single scan and contiguous multiple scan longitudinal dose distributions at the surface of a cylindrical water-filled phantom. They found that the doses measured using film on four CT scanner models were accurate to within $\pm 15\%$ compared to TLD measured point doses, and the accuracy was limited mostly by the energy dependent response of the film. Shope et al. (1982) used individually packaged 1.6 cm by 20 cm strips of Kodak XV-2 film on the surface of, and inserted into, the CTDI head and body phantoms in order to measure SSDPs. For the peak dose, they found disagreements with TLD point dose measurement of up to 20%. Film tended to give higher dose values than TLDs in the scatter tails of the SSDPs which lead the authors to caution against using SSDPs measured using film alone in calculating multiple scan dose profiles. This was again due to the energy response of film. Because of these results, film is not in wide use today for accurate measurements of absolute SSDPs in conventional x-ray CT. Film has

been used with somewhat better results for electron beam CT, presumably due to the harder x-ray spectrum compared to conventional CT (Zink and McCollough, 1994).

2.3.5.2 TLDs

By far the most common and most accepted dosimeter for measuring absolute CT single and multiple scan dose profiles is the TLD. TLDs offer high sensitivity and dynamic range (linear response from a few cGy to $\sim$ 10 Gy) and no dose-rate dependence (Attix, 1986). They can be manufactured to small dimensions and thus offer potentially high spatial resolution ($<$ 1 mm sampling interval). Discussions of the general properties of TLDs can be found in Attix (1986) for example. Although TLDs come in many forms, those used for SSDPs are usually 3 mm $\times$ 3 mm $\times$ 0.9 mm lithium fluoride (LiF) chips doped with trace amounts of Mg and Ti (denoted LiF:Mg,Ti). These chips, like many other TLDs, can be purchased singly or pre-arranged in long ribbons. Davis et al. (2003) studied the energy response of LiF:Mg,Ti TLDs (model TLD-100, Thermo Electron RM&P) exposed to radiation ranging from 30 kV x-rays to ^{60}Co gamma rays, and found less than 5% variation in relative dose response for the range of mean energies of 10 keV to 100 keV. A few groups have recently utilized LiF:Mg,Cu,P TLDs for measuring CT dose profiles. Tsai et al. (2003) used LiF:Mg,Cu,P TLDs to measure SSDPs and stated that these TLDs possess a lower detection limit, 30 – 40 times the sensitivity and improved tissue equivalence compared to LiF:Mg,Ti TLDs, and claimed that they are ideal for measuring dose profiles since these TLDs provide high spatial resolution. They reported that the 4.5 mm diameter and 0.86 mm thick TLD chips had a low detection threshold of 0.6 μGy (lower than standard TLDs) and an energy dependence within 15% in the energy range of 15 keV to 3 MeV. Cheung et al. (2001) used these same TLDs to measure single and multiple scan dose profiles and highlighted the same desirable characteristics as Tsai et al. (2003). Use of these newer forms of TLDs however is not yet widespread.

No matter which form of TLDs is used, dose profiles are typically measured by arranging the TLD chips along a line perpendicular to the scan plane (parallel to the axis of rotation) in standard CTDI head and body phantoms. Although any radial position in the phantom can be used, the SSDP is usually only measured along the phantom central axis since this is what is required by FDA regulations (FDA, 2003). The TLDs are arranged in a PMMA rod

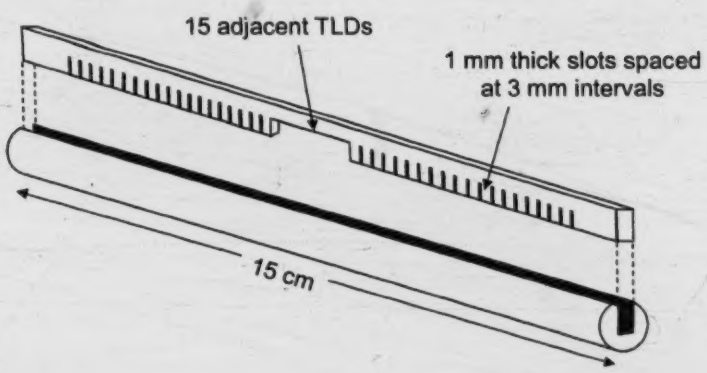

Figure 2.7: Schematic of a PMMA rod designed to hold an array of TLDs for measuring a SSDP in the CTDI phantoms. TLDs are stacked face to face in the central region for high sampling of the SSDP peak and are typically spaced at 3 mm intervals for the scatter tail regions of the SSDP. Re-created from AAPM (1993).

similar to the illustration shown in Fig. 2.7 which is a re-creation of the design suggested in AAPM (1993). The rod is inserted into the CTDI phantoms at the longitudinal bore positions. For the scatter tails of the SSDP, the TLDs are spaced at relatively large intervals, 3 mm for example, since the magnitude of the dose gradient is small. For the high dose gradient regions near the peak of the SSDP ($z = 0$), typically 15 TLDs are stacked face to face to achieve higher sampling. Thus with an individual TLD thickness of 0.9 mm, the smallest achievable sampling interval using TLDs is 0.9 mm. This is generally thought to be adequate for details of the spatial variation of the SSDPs (Rothenburg and Pentlow, 1995) although this may not be true when measuring the SSDP peak and penumbral regions of thin slices. In using this technique to measure the SSDP, only a single axial scan is required meaning that the irradiation time is short and does not thermally challenge the heat storage capacity of the x-ray tube too heavily.

Once the SSDP is measured, the SSDP curve is then used to calculate the MSAD or CTDI. The MSAD can be determined by mathematically superposing and summing the SSDP curves offset from one another along the z-axis at the sampling interval (b) of interest. For calculating the CTDI, SSDPs can be numerically integrated if the sampling rate is high enough. Alternately, the SSDPs can be fit with an empirically-derived function and integrated analytically. For SSDPs measured in CTDI phantoms using LiF TLDs, several functional forms have been derived and applied with reasonable success includ-

ing the sum of two Gaussians (Shope et al., 1981), a product of exponentials (Leitz et al., 1995) and the sum of a Gaussian and Lorentzian function (Tsai et al., 2003).

In measuring multiple scan dose profiles, the same TLD rods used for measuring SSDPs are utilized for convenience even though the high sampling rate near the central scan is not really required (since the multi-scan dose profile is relatively flat in this region). The MSAD is then the average dose value over the interval $z = \pm b/2$ of the multiple scan dose profile where b is the scan interval. Jucius and Kambic (1977) found good agreement between a multiple scan profile for a series of four scans measured with TLDs along the central axis of the body CTDI phantom and one reconstructed from the superposition of several offset SSDPs. In McGhee and Humphreys (1994), the agreement between the measured and calculated multiple scan dose profiles from 11 contiguous slices in the body CTDI phantom was reasonably good. However, the difference between the MSAD extracted from the measured and calculated multiple scan profiles differed by up to 15%, with the calculated values consistently higher. No explanation of the difference was given. The results from both of these authors did however experimentally validate the MSAD concept in general.

The major difficulty arising from the use of TLDs is their practicality in a clinical setting due to the amount of time and care needed to produce an accurate and precise result. The total time invested in measuring single and multiple scan dose profiles, when one considers TLD handling, annealing and readout, can be substantial. Many TLDs ($\sim$ 100) are required to measure a single profile and if an error is made during irradiation, one must wait hours to prepare and calibrate another batch of TLDs if more are not at hand. Furthermore, Rothenburg and Pentlow (1995) state that for measuring SSDPs, an accuracy of only 20% can be obtained with optimum handling of TLDs. For these reasons, routine quantitative CT dosimetry is performed using alternate dosimeters such as the pencil ionization chamber discussed in the next section. TLDs still remain the "gold standard" for measuring SSDPs but more as a tool for visualizing the spatial extent of the dose and not necessarily to determine an accurate value of the MSAD or CTDI.

2.3.5.3 Pencil Ionization Chambers

Since measurements of the MSAD or CTDI using TLDs was (and is) time consuming and cumbersome, an alternate measurement method requiring only a single scan was desired in the early development years of CT dosimetry. This lead to the introduction of a long pencil ionization chamber to measure and integrate the SSDP directly as described in Suzuki and Suzuki (1978). Unlike TLDs, a pencil chamber offers no information on the spatial distribution of the dose, only the dose line integral. The pencil chamber can be used free in air but is more commonly inserted into CTDI phantoms and aligned parallel to the z-axis. Assuming the chamber length is sufficiently long enough to include all of the scatter tails of the SSDP, the CTDI and hence MSAD can be calculated for a given slice width T as

$$CTDI = M \cdot N_X \cdot f \cdot \frac{L}{T} \tag{2.14}$$

where M is the electrometer reading ($\propto$ charge) that has been corrected to a set of reference calibration conditions, N_X is the exposure calibration factor for the ion chamber at the effective energy of the CT beam and L is the active length of the pencil ion chamber. In Eq. (2.14), M includes corrections for ambient temperature and pressure, and also includes the reading to charge conversion factor if it is not included in the N_X calibration. f is the exposure to dose conversion factor

$$f = 0.876 \text{ cGy/R} \left(\frac{\overline{\mu}_{en}}{\rho} \right)_{air}^{med} \tag{2.15}$$

where $(\overline{\mu}_{en}/\rho)_{air}^{med}$ is the ratio of the mass energy absorption coefficients of the measurement medium to air at the effective energy of the CT beam. N_X and f are usually evaluated at an effective energy of 70 keV which is taken to correspond to 120 kVp to 140 kVp filtered CT beams (Rothenburg and Pentlow, 1995). The variation of the f factor as a function of the effective photon energy is about 17% over the $55 - 80$ keV range (McCrohan et al., 1987). Thus reporting the absolute dose to any medium other than air may lead to significant errors since the quality of beams can vary substantially between different scanner models operating at the same kVp (dependent on inherent and added filtration), and the beams become harder with depth in phantom.

Pencil chambers can be purchased with active lengths up to 15 cm but almost all chambers currently in use (as evidenced by the literature) are 10 cm long. The active volumes are typically 3 cm^3. Pavlicek et al. (1979) evaluated a 10 cm long MDH model 20x5-103CT ion chamber and found a flat energy response for beam energies > 30 keV. The response decreased to 75% at 15 keV. This was deemed acceptable for routine measurements. Spatially, a flat response was observed for the central 80% of the chamber length, highlighting the problem of possible variations in sensitivity over the long active length. Jucius and Kambic (1977) found slightly better results for a 10 cm long Capintec PC-4P pencil chamber with < 10% change in response for effective x-ray energies of 20 keV to 100 keV and less than < 5% variation in response over the active length of the chamber. Calibration of the chambers usually consists of irradiation in a uniform field large enough to cover the active length of the chamber. Since CT slices are usually thin however, this may not represent the best calibration conditions due to changes in sensitivity along the length of the chamber. Bochud et al. (2001) recommended irradiating only the central 50% of the chamber length to obtain a calibration factor for the chamber most representative of the operational geometry. Since the authors determined that this method of calibration represents a less than 3% change in the chamber calibration factor compared to irradiation of the entire chamber length, it is not usually implemented.

2.3.6 Practical CTDI Variations

Several variations on the CTDI exist, either because of the practical difficulties in measuring the SSDP over an infinite distance, or to describe the dose for specific conditions. These are briefly discussed below.

2.3.6.1 $CTDI_{14T}$ and $CTDI_{FDA}$

Based largely on the original Shope et al. (1981) data for the ratio of the MSAD to the CTDI as a function of the number of scans mentioned in Sec. 2.3.4, the FDA has formally defined the CTDI as

$$CTDI_{14T} = \frac{1}{nT}\int_{-7T}^{+7T} f(z)dz \tag{2.16}$$

where n is the number of tomograms (images) produced in a single scan (FDA, 2003). The factor n is included to accommodate multi-slice CT scanners which, on the newest scanners (to date), can produce up to 64 images per rotation. The quantity that is required by FDA regulations to be reported with every CT scanner in the U.S. is denoted CTDI_{FDA} and differs from CTDI_{14T} only in that it must be stated as absorbed dose to PMMA, the material of the phantom required for it's measurement. Doses must be reported for the center and periphery (1 cm depth) of the CTDI phantoms for every slice width.

The variable integration limits of Eq. (2.16) assume that most of the SSDP is contained within an interval equivalent to $14T$. For SSDPs measured in phantom (as opposed to free in air), this assumption is true generally only for thick slices since for thin slices (e.g., $\leq$ 3 mm), a smaller scatter volume is included in the (variable) integration limits and the scatter tails in the SSDP do not fall off proportionately with slice width (Kalendar, 2000). Another practical problem is that if one measures CTDI_{14T} using a pencil chamber with its fixed integration limits of 10 cm (for example), the pencil chamber reading will overestimate CTDI_{14T} for slice widths less than about 7 mm and underestimates CTDI_{14T} for slice widths more than 7 mm. To overcome this problem, Knox and Gagne (1996) measured slice width correction factors for CTDI_{14T} pencil chamber readings at the center of the CTDI head phantom. This was done by comparing readings acquired with the pencil chamber active length reduced to effectively $\pm 7T$ by covering the chamber with radio-opaque sleeves, to readings taken using the chamber's full 10 cm active length. Correction factors were also determined by integrating SSDPs measured using TLDs, which was necessary for slice widths greater than 7 mm due to the 10 cm active length of the chamber. This method enabled one to report CTDI_{14T} for any slice width using the pencil chamber reading by multiplying by a correction factor. A few example correction factors are 0.45 and 1.1 for 1 mm and 10 mm slice widths respectively. Correction factors for pencil chamber readings acquired in the CTDI phantoms at central and peripheral (1 cm depth) positions for several slice widths have also been calculated by the ImPACT group (ImPACT, 2004) and are currently in wide use. These factors include the f factor for absorbed dose to PMMA. For CT systems in North America, the CTDI for a given technique shown on the display console is actually CTDI_{FDA} and these two terms (CTDI and CTDI_{FDA}) are often used interchangeably.

2.3.6.2 $CTDI_{100}$

There are systematic difficulties with the FDA definition of the CTDI due to the variable integration limits discussed in the last section, e.g., the necessity of correction factors. The fact that the pencil chamber correction factors for $CTDI_{14T}$ were not unity for slice widths < 7 mm implies that there is significant dose in the SSDP for $|z| \geq \pm 7T$ that is not being included in the dose integral. In other words, $CTDI_{14T}$ as a fundamental quantifier of the accumulated dose is inadequate especially for small slice widths. Leitz et al. (1995) instead proposed a "practical" variation of the CTDI which had fixed 100 mm integration limits, independent of the slice width,

$$CTDI_{100} = \frac{1}{T}\int_{-50mm}^{+50mm} f(z)dz. \tag{2.17}$$

Unlike $CTDI_{FDA}$ which is reported as absorbed dose to PMMA, air-kerma is the dose quantity reported using $CTDI_{100}$. Thus any potential errors introduced by incorporating the energy-dependent f factor are removed. One immediate advantage of $CTDI_{100}$ is that a 10 cm pencil chamber directly integrates the SSDP over the proper 10 cm interval and no slice width conversion factors are needed. In actuality, the ImPACT (ImPACT, 2004) conversion factors discussed in the last section are the ratio $CTDI_{100}/CTDI_{FDA}$. This ratio in the ImPACT data approached 3.9 in the body CTDI phantom for a 1 mm slice width, highlighting the extent to which $CTDI_{FDA}$ can underestimate the accumulated dose. $CTDI_{100}$ is the CT dose descriptor currently used in Europe (OOPEC, 1999) where measurements are required at the center and periphery of CTDI phantoms. One additional observation is that the correction factor determined by Knox and Gagne (1996) for a 10 mm slice width is 1.1, implying that $CTDI_{100}$ as a dose quantifier and 10 cm long pencil chambers may be inadequate to properly include the scatter of the SSDP, even at the center of the head phantom. One would expect the dose outside the limits of $CTDI_{100}$ to be even larger at the center of the body phantom especially for large slice widths. In fact, the ImPACT correction factor for a 10 mm slice width at the center of the body phantom (after correcting for the f factor) is 1.15.

2.3.6.3 Weighted CTDI

Assuming a linear decrease in dose from the surface of a phantom to the center, the average dose or weighted CTDI, $CTDI_w$ was defined by Leitz et al. (1995) as

$$CTDI_w = \frac{1}{3}CTDI_{100,c} + \frac{2}{3}CTDI_{100,p} \tag{2.18}$$

where $CTDI_{100,c}$ and $CTDI_{100,p}$ are the $CTDI_{100}$ at the phantom center and periphery (1 cm depth) respectively. In this definition, the authors assumed for simplicity that for a single scan the dose outside T was zero, and within the slice the value for $CTDI_{100}$. $CTDI_w$ attempts to give an average dose to the entire scan plane instead of just one x, y point like $CTDI_{100}$ or $CTDI_{FDA}$. There is no advantage in $CTDI_w$ over other CTDI definitions except that it combines two dose values (central and peripheral) into one. Although European countries now require reporting the dose as $CTDI_{100}$, the dose displayed on the scanner console for a given technique is $CTDI_w$. When the pitch P is not equal to 1 for volume scanning, the effective CTDI (also known as $CTDI_{vol}$) is defined as $CTDI_w/P$.

2.3.6.4 Dose Length Product (DLP)

The dose length product (DLP)(OOPEC, 1999) attempts to characterize the spatial extent and intensity from a complete scan series or examination, and is given by

$$DLP = CTDI_w \cdot N \cdot T \tag{2.19}$$

where N is the number of slices in the scan series. One should keep in mind that because of the division of the dose line integral by T (Eq. 2.10, the value of the CTDI (or $CTDI_w$) assumes that the dose outside of T is zero. Therefore, taking pitch related effects into account, the irradiated volume is NT and not necessarily the scan length L ($L = NT$ for contiguous scanning only). The DLP as defined by Eq. (2.19) takes these pitch-related effects into account.

2.3.7 Monte Carlo Methods

Monte carlo computer simulations have been used for decades in radiotherapy to model radiation transport in matter in order to estimate the dose to a patient. Although the use of Monte Carlo for CT dosimetry is relatively new, it has been used successfully for primarily two purposes: (1) to estimate the

effective dose to the patient as the weighted sum of the dose to specific organs or (2) to determine the energy imparted (integral dose) to a region from a single CT slice or a scan series. One can also re-create the multiple and single scan dose profiles in cylindrical CTDI-like phantoms using Monte Carlo to determine the standard dose descriptors like CTDI and MSAD.

2.3.7.1 Effective Dose

Up to now, all the dose parameters discussed have been specific to CT and do not allow any direct comparison to standard radiological procedures such as projection radiography. Therefore an effective dose has been defined as the equivalent uniform dose to the entire body from a CT scan series, derived from the sum of the organ doses which may or may not lie inside the directly irradiated volume of the body. It is meant to provide an assessment of risk to the patient. Formally the effective dose is

$$E_{eff} = \sum_i w_i D_{org,i} \tag{2.20}$$

where $D_{org,i}$ is the mean dose to a particular organ and w_i is a tissue-weighting factor which depends on the organ's sensitivity to radiation. Sample values for w_i as reported in ICRP60 (1991) are 0.20 for gonads, 0.12 for lungs, 0.05 for breast tissue, and 0.01 for the skin. The use of Monte Carlo techniques enters into determination of effective dose through the calculation of $D_{org,i}$. Shrimpton et al. (1991) used a Monte Carlo model simulating the circular motion of an x-ray source around a (mathematical) adult anthropomorphic phantom for several source-to-axis distances, kVp and beam filtrations in order to determine the mean doses to 27 different organs or regions using standard organ masses. Organ and region doses were computed for scans series consisting of 208 slices (5 mm slice width) for a region covering the phantom from the top of the head to nearly the base of the trunk. Most estimates of the effective dose are calculated using the data of Jones and Shrimpton (1993). Effective doses from CT examinations can range from approximately 1 to 64 mSv (Nagel, 2000) dependent upon the region of the body scanned, i.e., the proximity to particularly radiation sensitive organs.

2.3.7.2 Energy Imparted

Determination of effective doses to patients from Monte Carlo calculation of mean organ doses can be difficult and time consuming. An alternative method is to calculate the energy imparted (EI) to the scanned volume of the phantom or patient. Although the EI to a volume does not consider the relative radiosensitivity of a given organ, it does allow evaluation of the relative changes in patient dose dependent on the scanner technique factors used.

Huda and Atherton (1995); Atherton and Huda (1995, 1996) used Monte Carlo techniques to study the relationship between the CTDI and energy deposited in a cylindrical phantom using a range of $30 - 140$ keV monoenergetic photons. They showed that a first-order estimate of the EI to a cylindrical (CTDI) phantom can be obtained by multiplying the average CTDI value at the center and periphery (i.e., $CTDI_w$) with the mass of the directly irradiated portion of the phantom. Improvements on such EI estimates can be made by the inclusion of Monte Carlo derived correction factors which consider the energy-dependent effects of the beam-shaping filter and phantom radius on the photon fluence.

In Atherton and Huda (1995), computer generated SSDPs for a 5 mm slice width were shown for 80 keV photons at the center and periphery of a simulated head CTDI phantom. The profiles were similar to measured profiles shown in the literature although like others shown in the literature, the SSDPs were scaled to the peak peripheral SSDP value such that the magnitude of the relative dose in the scatter tails at the center of the body phantom was not scaled downwards. They also showed that for 80 keV photons, the dose integral ($\sim$ CTDI) is nearly independent of the radial position in an acrylic head phantom and increases slowly, nearly doubling from the center to the surface of the body phantom. Absolute integral dose values in an acrylic phantom were generally lower ($10 - 20\%$) than in phantoms of water, lung, fat and muscle indicating that acrylic (PMMA) may not properly simulate the scattering conditions in a real patient (this was not explicitly stated by the authors) as was alluded to earlier in this chapter. Boone et al. (2000) also generated SSDPs in 16 cm and 32 cm diameter cylindrical water phantoms using Monte Carlo simulations, and compared the results to relative air-kerma measurements made using a large-volume ion chamber and CTDI phantoms. No bow-tie filters were present in the modeled and real scanner. The measurement method differed from traditional methods in that the probe was adjacent

to the end of phantom in order to measure the scattered radiation from slices incident along the phantom length. Therefore they were able to measure a half-SSDP out to a distance of 14 cm from the scan center. In both the head and body CTDI phantoms for 80 kVp and 120 kVp beams, the relative air-kerma was significant at distances of 14 cm and was in good agreement with the Monte Carlo results. For the head phantom, the relative air kerma at $z = 50$ mm was about 40% of the peak dose at both kVp settings, though the implication of this substantial relative air-kerma on the CTDI value was not explicitly discussed. Multiple scan dose profiles were also presented using the Monte Carlo data to show the effects of pitch on the magnitude of the dose. Finally, dose values for several phantom radial positions, scan lengths and kVp as a function of z distance from the scan center in CTDI phantoms were tabulated in order to estimate the dose to organs in regions adjacent to the scanned volume.

It is clear that Monte Carlo techniques for estimating radiation dose (either as effective dose or energy imparted) can be much more flexible that conventional measurement techniques such as CTDI and MSAD using TLDs or pencil chambers. However, Monte Carlo methods are still applied using generic mathematical phantoms and are not necessarily patient specific. Patient-specific modelling is possible based on the CT images of patient anatomy for example, but Monte Carlo calculations are time consuming and not clinically practical with today's current computational technology. Therefore, conventional measurement-based methods are still the most practical for estimating the patient dose from CT.

2.3.8 Accumulated Dose $D_L(z)$

A recent reformulation of the accumulated dose in CT was introduced by Dixon (2003). Since much of the focus of the experimental sections of this thesis is the verification of the theory and methods suggested by Dixon, a more comprehensive summary of the theoretical considerations are presented below.

2.3.8.1 Helical Scans

Let $\dot{f}(z,t)$ be the instantaneous dose rate profile along the axis of a cylindrical phantom which is moving at a constant velocity ν through a rotating CT beam

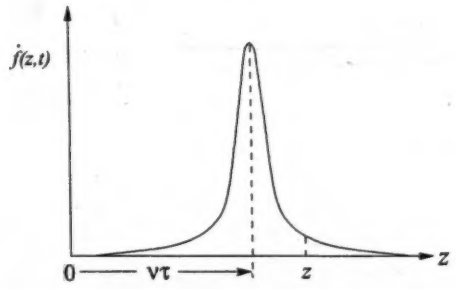

Figure 2.8: Instantaneous dose rate profile along the central axis of a cylindrical phantom moving at constant velocity ν for a helical scan.

(i.e., a helical scan). Assume that the phantom axis and rotational axis of the scanner are coincident. The accumulated dose $D(z)$ at a point z along the phantom axis as the phantom translates through the beam is then the integral of the portion of $\dot{f}(z,t)$ that the point z "sees" as it moves through the profile during an irradiation time t_o,

$$D(z) = \int_{-t_o/2}^{t_o/2} \dot{f}(z - \nu t, t)dt. \tag{2.21}$$

This is illustrated in Fig. 2.8. Since the dose rate along the central axis is constant in time (neglecting fluctuations in x-ray tube output) due to the cylindrical symmetry of the phantom, $\dot{f}(z,t) = f(z)/\tau$ where $f(z)$ is equivalent to the SSDP previously defined and τ is the time for one rotation of the x-ray source. If $L = \nu t_o$ is the total length of phantom traversed by $f(z)$ and we let $y = \nu t$, then the temporal integral Eq. (2.21) becomes the spatial integral

$$D_L(z) = \frac{1}{\nu\tau} \int_{-L/2}^{L/2} f(z - y)dy. \tag{2.22}$$

where the product $\nu\tau$ is the table advance per rotation of the source and the subscript L is included as a reminder that *the accumulated dose is now a function of the length of the phantom actually irradiated* (compare to CTDI or MSAD). If the scan length is represented as a rectangular function $\Pi(z/L)$

with base L and unit height, then Eq. (2.22) can be re-written as

$$D_L(z) = \frac{1}{\nu\tau}\int_{-\infty}^{\infty} f(z-y)\Pi(y/L)dy \tag{2.23}$$

$$= \frac{1}{\nu\tau} f(z) \otimes \Pi(z/L) \tag{2.24}$$

where $\otimes$ represents the convolution operation. The way in which the accumulated dose builds up as the SSDP moves through the "scan length box" is illustrated in Fig. 2.9. Assuming $f(z)$ to be a symmetric function, the maximum dose (arguably the most important from a clinical dosimetry point of view) will occur at the center of the scan length ($z = 0$) and Eq. (2.22) becomes

$$D_L(0) = \frac{1}{\nu\tau}\int_{-L/2}^{L/2} f(z)dz. \tag{2.25}$$

When the scan length L is longer than the z-extent of $f(z)$ (i.e., the SSDP width), $D_L(0)$ will reach a limiting or equilibrium value since we have now integrated the entire SSDP. Equation (2.25) then becomes

$$D_{eq}(0) = \frac{1}{\nu\tau}\int_{-\infty}^{\infty} f(z)dz \tag{2.26}$$

where $D_{eq}(0)$ is the equilibrium dose. Therefore the equilibrium condition depends only on the length of the scan and the profile width. The dose length

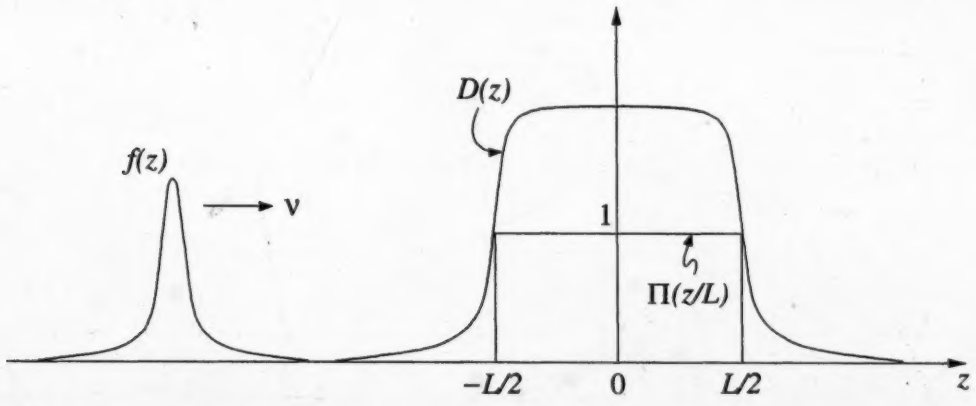

Figure 2.9: The SSDP $f(z)$ convolved with a rectangular function representing the helical scan length L to produce the accumulated dose distribution $D(z)$.

integral (DLI), similar to the dose length product (DLP) defined previously, is given as (see Dixon (2003))

$$DLI = \int_{-\infty}^{\infty} D_L(z)dz = \ldots = LD_{eq}(0). \tag{2.27}$$

The dose length product using the DLI definition is then the area under the *entire* cumulative dose profile, including the scatter tails beyond the scan length L, and not just the volume of the directly irradiated region with extent NT ($= L$ for contiguous scans) used in the DLP definition, Eq. (2.19).

As mentioned earlier, possibly the most important point to emerge from this formulation of the accumulated dose in CT is the dependence of the dose on the scan length. The ideal definition of the CTDI (Eq. (2.10)) involves integrating the entire SSDP, which is now shown to be unnecessary if the actual scan length used is shorter than the SSDP width. Thus if only a 10 cm long volume is irradiated, then CTDI_{100} is entirely accurate. However, clinical scans lengths can be considerably longer and the potential underestimate of the dose using CTDI_{100} or CTDI_{FDA} becomes obvious if there exists considerable dose in the SSDP scatter tails beyond 100 mm or $14T$ respectively. Also note that unlike the CTDI concept, the nominal slice width T does not appear anywhere in the equations for dose (e.g., Eq. (2.25)). Instead, the dose line integral is divided by a factor related to the scan spacing (through $\nu\tau$) which unlike T, *is* directly related to the dose. For example, at a constant rotation time τ, increasing the couch speed ν results in a decrease in dose to the patient since the exposure is now spread over a larger volume.

2.3.8.2 Axial Scanning

Unlike helical scanning, the phantom is stationary during irradiation in axial scanning with each scan of a series equally spaced by the scan interval b. Then for $N = 2J + 1$ scans with the central scan centered about $z = 0$, the cumulative dose can be represented as

$$D(z) = \sum_{n=-J}^{J} f(z - nb) = f(z) \otimes \sum_{n=-J}^{J} \delta(z - nb). \tag{2.28}$$

Since the cumulative dose profile will be quasi-periodic along z with a period b due to the summation of several discretely spaced SSDPs (see Fig. 2.5), the

running-mean dose over one period b can be shown to be (see Dixon (2003))

$$\overline{D}_L(z) = \frac{1}{b}\int_{-L/2}^{L/2} f(z-y)dy \tag{2.29}$$

which is similar in form to the helical case. Again the factor T in the CTDI definition has been replaced by the scan interval which directly influences the patient dose. The maximum dose will occur at the center of the scan series for a symmetric SSDP and is given by

$$\overline{D}_L(0) = \frac{1}{b}\int_{-L/2}^{L/2} f(z)dz, \tag{2.30}$$

which represents the same quantity as the MSAD and is similar to the expression for accumulated dose for a helical scan series, Eq. (2.25); with $L = Nb$, the DLI= $L\overline{D}_{eq}(0)$.

2.3.8.3 Helical Scanning for Off-Axis Points or Non-Cylindrical Phantoms

For points off the central axis (peripheral) in a cylindrical phantom or at any point in a non-cylindrical phantom, the instantaneous dose rate profile now depends on the angle of the source θ, i.e.,

$$\dot{f}(z) = \frac{1}{\tau} f(z, \theta - \theta_z). \tag{2.31}$$

The dose rate is maximum at $\theta = \theta_z$. The average axial dose profile is then

$$f(z) = \frac{1}{2\pi}\int_{\theta_0}^{\theta_0+2\pi} f(z, \theta - \theta_z)d\theta \tag{2.32}$$

where θ_0 is an arbitrary starting angle. Substituting Eq. (2.32) into Eq. (2.21) with $y = \nu t$ and $\theta = \omega t$ gives (see Dixon (2003))

$$D(z, \theta_z) = \frac{1}{\nu\tau}\int_{-L/2}^{L/2} f(z-y, \theta - \theta_z). \tag{2.33}$$

Averaging this result over θ_z leads once again to the same expressions for helical dose on the central axis, as Eq. (2.22) or Eq. (2.23), which also represent the running mean dose (averaging over z) on a peripheral axis for points near

$z = 0$ provided that $L \gg \nu\tau$.

Armed with the SSDP $f(z)$ measured using one's dosimeter of choice, the accumulated dose at any point z, for any scan length and scan spacing, can be calculated using the $D_L(z)$ formalism. However, as mentioned earlier, the sampling capabilities (spatial resolution) of TLDs may lead to errors in calculating the cumulative dose, not to mention the considerable time expenditure necessary in using TLDs. Alternately, one could place any small integrating dosimeter such as a *single* TLD chip or small volume ion chamber at the position $z = 0$ in a phantom and integrate the dose directly as one performs a scan series of *any* length L to determine the maximum dose $D_L(0)$. Since ion chambers are more accurate than TLDs, a small volume ion chamber may be desirable to measure the dose integral including the scatter tails that potentially extend beyond the active length of 10 cm pencil chambers. Dixon briefly tested this method experimentally using a 0.6 cm^3 Farmer chamber at the center of the head CTDI phantom on a multi-slice scanner for a slice selection of 4×5 mm and a scan length of 150 mm. Values of $D_L(0)$ for helical (pitch = 0.75) and axial ($b = 20$ mm) scans of length $L = 150$ mm were about 10% higher than $CTDI_{100}$ values measured using a standard 10 cm long pencil chamber.

It is obvious that the dose line integral (integral of Eq. (2.25)) measured using an axial or helical scan series and a small volume ion chamber for $L = 100$ mm should be equal to the dose length product using a 10 cm long pencil chamber and a single axial scan. This was mentioned in Dixon (2003) but not demonstrated experimentally. A comprehensive experimental evaluation of this method is therefore required including measuring $D_L(0)$ for parameter sets consisting of scan length, slice width and CT system. Primary verification of the method would be comparison of the current "gold standard" of measuring the dose integral, the pencil chamber.

2.3.9 Relationship Between Dose and Image Quality

The primary goal of CT is to obtain an image which contains adequate spatial and contrast resolution to detect and diagnose any abnormalities. The image quality in CT depends primarily on the subject (inherent) contrast, object contrast and the statistical noise present. It is the superior low-contrast reso-

lution in CT that distinguishes it from other clinical x-ray modalities. All else being equal, the most direct way of improving low-contrast resolution and thus image quality in CT is to reduce the quantum noise or mottle by increasing the number of photons reaching the detectors. Unfortunately this cannot be realized without also increasing the dose to the patient. Therefore a compromise must be made for the maximum allowable dose while still forming a usable image. Brooks and Di Chiro (1976) derived the relationship between dose and an image quality or noise in CT. For a water phantom with a circular cross section, the dose at the surface (perimeter) is given by the relation

$$D \propto \frac{e^{\mu d}}{\sigma^2 w^3 T} \tag{2.34}$$

where μ is the mean linear attenuation coefficient of water, d is the phantom diameter, σ is the standard deviation of the CT numbers in the image (a metric of noise), w is the effective beam width ($\sim$ voxel dimension) and T is the slice thickness. Therefore, reducing the noise by one half requires a four-fold increase in the dose to the patient, all other factors being equal. Similar relationships can be made regarding changes in the patient size (d), spatial resolution (through w) and the slice thickness (T) and their affect on the dose.

2.3.10 Factors Affecting Dose

Below is a breakdown of the factors which influence the patient dose in CT where the influence of one parameter assumes all others remain unchanged.

2.3.10.1 X-Ray Tube Voltage (kVp)

The effective energy of the polyenergetic CT beam (ignoring filtration) depends on the accelerating potential of the x-ray tube, or kilovoltage peak (kVp). The efficiency of x-ray production by bremsstrahlung increases with increasing kVp, and so therefore does x-ray tube output since the number of photons at all energies in the spectrum are increased. If the radiation output is quantified as the amount of ionization produced in air or the exposure, the exposure is approximately proportional to kVp^2 for x-ray tubes operating in the diagnostic energy range (Bushberg et al., 2002). The result is an increase in the overall patient dose with increased kVp, and also an increase in the ratio of the dose at depth to the surface dose (increased dose uniformity in the scan plane) since

the higher energy beam is more penetrating. Nickoloff et al. (2003) reported a dependence of the CTDI $\propto$ kVp^n, with n for six different CT scanners ranging between 1.63 and 2.35. These results were based on pencil chamber measurements at the center of the CTDI body phantom.

2.3.10.2 Tube Current-Time Product (mAs)

The x-ray tube current (mA) is the number of electrons accelerated from the cathode to the anode per unit time. The total x-ray output, and therefore exposure or dose, then depends on the product of the current and the total x-ray production time (s), or mAs. Increasing the mAs increases the dose proportionately and thus it is common to quote the output of a given CT scanner as the dose per 100 mAs. The dose is also linear in mA and time separately. One of the most direct ways to reduce the image noise is to increase the mAs, but that of course is accompanied by an increase in the dose.

2.3.10.3 Beam Collimation

Changing the collimated slice width has little effect on the MSAD and changes the dose to a point only slightly. For constant mAs, increasing the slice width results in a marginally higher patient dose. McNitt et al. (1999) measured the CTDI at the center of a 32 cm diameter lucite phantom using TLDs for collimations of 1, 3, 5 and 10 mm. They found that for contiguous axial and helical scans, smaller collimations yielded approximately the same dose ($\pm$15%) to those of larger collimations due to the higher degree of overlap between adjacent scans seen for studies using a smaller collimation.

2.3.10.4 Filtration

X-ray beams in CT are almost always filtered which serves many purposes. First, inherent tube filtration and any added flat filters (i.e., not beam-shaping filters) serve to remove the lower energy photons that are easily absorbed in a patient as dose, and therefore contributing nothing to image formation and quality. Secondly, beam-shaping filters are usually added to create a constant attenuation path length along a ray through the patient, thus providing a more constant signal to the detectors and minimizing beam hardening artifacts (since the pixel intensity is proportional to the effective μ). Increased filtration hardens the beam, increasing the effective energy and decreasing the dose (at

constant mAs) as discussed in Sec. 2.3.10.1. This dose reduction is somewhat offset however since the reduced beam intensity as a result of the filter may require increased tube loading to ensure an adequate signal to the detectors for imaging. Filtration also increases the ratio of the dose at depth to the surface dose, and hence a more uniform distribution of dose in the scan plane, since the beam is more penetrating than an unfiltered beam .

2.3.10.5 Focus-Axis Distance

Most scanners today have a focus-axis distance (FAD) of about 60 cm but can range from $50 - 80$ cm. At constant mAs, decreasing the FAD will increase the ratio of the surface to center dose in phantom since the effective x-ray output is greater (inverse-square effect), leading to a less homogeneous dose distribution in the scan plane. This does not mean that the scanner with a shorter FAD will result in a greater overall dose than one with a long FAD however since the mAs per scan can be reduced accordingly.

2.3.10.6 Pitch or Scan Interval

The MSAD varies approximately inversely with pitch in helical scanning and inversely with the scan interval in axial scanning (McNitt et al., 1999). The is because the effective mAs over the irradiated volume decreases as the spacing between adjacent scans increases.

2.3.10.7 Patient Size

Since dose is defined as energy absorbed per unit mass, a larger patient (mass) for the same scanning technique results in an overall decrease in the dose to the irradiated volume. The CTDI at the center of cylindrical lucite phantoms was found by Nickoloff et al. (2003) to decrease approximately exponentially with phantom diameter (size). They also determined that the CTDI at the center of a small phantom (6 cm diameter) was nearly the same as the CTDI at the surface (1 cm depth). For a CTDI body phantom, they found the central CTDI to be about 50% of the surface CTDI, in agreement with the results from other references in the literature presented earlier in this thesis.

2.3.10.8 Number of Slices

When the spacing between scans is such that the SSDPs overlap, the integral dose increases with the number of slices for scan lengths less than the width of the SSDP as stated earlier. For scan lengths greater than the SSDP width, the multi-scan dose reaches an equilibrium value. If the pitch or scan interval is large, the number of slices may not affect the *accumulated* dose if the SSDPs are non-overlapping (the dose along z in a patient will just approach the local value of the SSDP).

2.3.10.9 Rotation Angle

CT image reconstruction only requires (180°+fan angle) though most scanning techniques expose the patient over the full 360° (normal) rotation. To counteract image artifacts due to patient motion for example, some scanners can overscan by up to 45° more than 360° leading to an obvious increase in dose compared to a normal acquisition. The radial dose distribution will also be highly asymmetric in this case.

2.3.10.10 Single Slice vs. Multi-Slice Scanners

There is no obvious reason why the dose from a multi-slice scanner should be any different than a single slice scanner for the same technique settings since the gantry geometry and x-ray filtration are essentially the same for the two systems. However, the geometric efficiency (ratio of the x-rays exiting the patient to those striking the sensitive region of the detectors) of multi-slice scanners is generally lower than single slice systems. This is because the primary collimation of multi-slice systems must be made wider than $n \times T$ ("overbeaming") in order to avoid calibration problems in the outermost detectors due to beam penumbra. Lewis (2001) stated that the CTDI for the widest collimations on modern multi-slice scanners is about 10% higher than single slice scanners (at fixed mAs), and up to about 40% higher for the smallest collimations. These results were based on data provided by the ImPACT group. Since multi-slice CT is a relatively new technology, there is an insufficient quantity of data in the literature to make a broad statement on the differences in the accumulated dose between single- and multi-slice scanners.

2.4 The Basic Problem and the Scope of this Thesis

Conventional techniques of measuring the accumulated dose in CT incorporate several assumptions, the most important of which involves the true extent of the scatter tails of the SSDP. Implicit in the definition of the CTDI is that the first and last scans of the series contribute no significant dose to the region of the central scan. Alternatively, it is assumed that most of the SSDP is being integrated regardless of the measurement method (TLDs or a pencil ion chamber). Standard 15 cm long CTDI phantoms are assumed to be long enough such that the scatter tails of the SSDP fall to zero near the phantom edges. If this assumption is not valid, it automatically follows that a 10 cm long pencil chamber will not be long enough to integrate most of the SSDP. $CTDI_{100}$ as a quantifier of CT dose will also be inadequate.

Several authors have indicated that the scatter tails of the SSDP measured at the center of standard CTDI body phantoms are non-negligible at large distances from the central scan. The consequence on the CTDI was usually never expressed explicitly. Table II summarizes the extent of the scatter tails as reported in the literature based on either measured TLD data or Monte Carlo (MC) simulations. The dose relative to the peak of the SSDP is tabulated for z positions corresponding to the edges of standard CTDI phantoms ($z = \pm 75$ mm) and for the integration limits of a 10 cm long pencil chamber or $CTDI_{100}$ ($z = \pm 50$ mm). Although comparison between the data from these three authors is inappropriate, the relative doses at the phantom edges and at the

Table II: Published results of the dose (relative to the peak dose of the SSDP) along the central axis of the CTDI body phantom at two z positions corresponding to the edges of 15 cm long CTDI phantoms and the dimensions of 10 cm long pencil chambers. Data is based on either Monte Carlo-generated (MC) or TLD-measured SSDPs as indicated.

Authors	Method	Beam width (mm)	Relative dose	
			$z = \pm 75$ mm	$z = \pm 50$ mm
Shope et al. (1982)	TLD	13	11%	25%
Boone et al. (2000)	MC	10	28%	42%
Dixon (2003)	TLD	20	17%	32%

limits of a 10 cm pencil chamber in both real and simulated profiles were clearly non-negligible. This observation is hard to identify in most other SSDPs displayed in the literature (for example Shope et al. (1982); McNitt et al. (1999); Cheung et al. (2001); McGhee and Humphreys (1994); Atherton and Huda (1995)) due either to the way they scaled the SSDPs (usually to the much larger peak of a peripheral profile) or since only the inner ±50 mm of the SSDP is shown. The results of Boone et al. (2000) are substantially larger than the others since no bow-tie filters were present in the CT beam.

At the center of the head phantom, the scatter tail dose tends to drop more rapidly with increasing distance from the scan center compared to the body phantom since less scatter is generated in the smaller diameter phantom. Tsai et al. (2003) measured the SSDP using LiF TLDs in the head phantom for a 5 mm slice thickness and showed a very slow decrease in the SSDP with distance from the scan center, reaching 9% of the peak dose at a distance of 35 mm. No data points were shown beyond this position. This result is consistent with other published SSDPs in the head phantom for a 5 mm slice width such as Cheung et al. (2001) who measured about 8% dose at $z = \pm 50$ mm , and with Boone et al. (2000) who showed about 5% dose at $z = \pm 5$ mm for a Monte Carlo generated SSDP. Therefore, for slice widths less than about 5 mm, the CTDI head phantom and pencil chambers lengths are probably adequate for measuring the scatter tails of the SSDP. This may not be true however when moving to the larger beam widths present in multi-slice scanners. For a 20 mm beam width on a multi-slice scanner (4×5 mm slice selection), Dixon (2003) showed 18% dose relative to the peak at $z = \pm 50$ mm, and fell to 1% dose at the phantom edges. Consequently, a 10 cm long pencil chamber may not be adequate for measuring the CTDI even at the center of the head CTDI phantom, especially for large beam widths. The argument could be made for longer pencil chambers, but current 10 cm long chambers are already quite fragile and problems with changes in sensitivity along the active length would only be exacerbated.

Another point of consideration is that the CTDI concept is technically only defined for axial scanning since it is a single slice measurement. However, McGhee and Humphreys (1994) found that the MSAD as determined by the superposition of offset SSDPs measured using TLDs in CTDI phantoms were in good agreement to the MSAD extracted from the multiple scan dose profile for 11 slices scanned in helical mode. They also concluded that $CTDI_{14T}$

was a good estimate of the MSAD in helical CT, but only in comparison to an equivalent axial scan with the same total scan length. There is currently no accepted method for measuring the accumulated dose from a helical scan series using an ion chamber, pencil or otherwise. ImPACT (2001) suggested a method using a pencil chamber to measure the CTDI for helical scans which involved scanning the entire length of the chamber in both axial and helical modes and calculating a correction factor to estimate "helical CTDIs". This method has not found widespread use. Based on the literature, it appears that the length of common pencil chambers may be inadequate for long body scans, especially for the large beam widths in multi-slice scanners. Therefore a small ion chamber method of measuring the accumulated dose using the $D_L(0)$ formalism is desirable and would currently represent the only method for measuring the accumulated dose in helical CT using ion chambers. As mentioned earlier, Dixon (2003) *did* experimentally demonstrate a small volume ion chamber method but only for a scan length equal to the length of CTDI phantoms (150 mm).

The general goal of this work is to experimentally test some of the common assumptions of conventional CT dosimetry, specifically the adequacy of the lengths of CTDI phantoms and 10 cm long pencil ion chambers. Additionally, an alternative method to TLDs for measuring SSDPs is explored using a diamond detector in an effort to improve on the spatial resolution and accuracy of the measured SSDP (with possibly less effort than TLDs). Finally, a small volume ion chamber method for measuring the accumulated dose in CT for several scan lengths, including scans in a phantom longer than the standard CTDI phantoms, will be investigated in an effort to properly include in the dose integral the extended scatter tails evident in the literature.

Chapter 2 References

AAPM (1993). Task group 2: Diagnostic x-ray imaging, report no. 39: Specification and acceptance testing of computed tomography scanners. Technical report, American Institute of Physics.

Atherton, J. V. and Huda, W. (1995). CT doses in cylindrical phantoms. *Phys. Med. Biol.*, 40(5):891–911.

Atherton, J. V. and Huda, W. (1996). Energy imparted and effective doses in computed tomography. *Med. Phys.*, 23(5):735–41.

Attix, F. H. (1986). *Introduction to Radiological Physics and Radiation Dosimetry.* John Wiley & Sons, New York.

Berger, M. J., Hubbell, J. H., Seltzer, S. M., Coursey, J. S., and Zucker, D. S. (1998). XCOM: Photon Cross Sections Database. http://physics.nist.gov/PhysRefData/Xcom/Text/XCOM.html.

Bochud, F. O., Grecescu, M., and Valley, J. (2001). Calibration of ionization chambers in air kerma length. *Phys. Med. Biol.*, 46:2477–2487.

Boone, J. M., Cooper III, V. N., Nemzek, W. R., McGahan, J. P., and Seibert, J. A. (2000). Monte carlo assessment of computed tomography dose to tissue adjacent to the scanned volume. *Med. Phys.*, 27(10):2393–407.

Brooks, R. A. and Di Chiro, G. (1976). Statistical limitations in X-ray reconstructive tomography. *Med. Phys.*, 3:237–240.

Bushberg, J. T., Seibert, J. A., Leidholt, J. E. M., and Boone, J. M. (2002). *The Essential Physics of Medical Imaging.* Lippincott Williamn & Wilkins, Philadelphia.

Cheung, T., Cheng, Q., Feng, D., and Stokes, M. J. (2001). Study on examinee's dose delivered in computed tomography. *Phys. Med. Biol.*, 46(3):813–20.

Conway, B. J., McCrohan, J. L., Antonsen, R. G., Rueter, F. G., Slayton, R. J., and Suleiman, O. H. (1992). Average radiation dose in standard CT examinations of the head: Results of the 1990 NEXT survey. *Radiology*, 184:135–140.

Davis, S. D., Ross, C. K., Mobit, P. N., Van der Zwan, L., Chase, W. J., and Shortt, K. R. (2003). The response of LiF thermoluminescence dosemeters to photon beams in the energy range from 30 kV x rays to ^{60}Co gamma rays. *Radiat. Prot. Dosimetry.*, 106(1):33–43.

Dixon, R. L. (2003). A new look at CT dose measurement: Beyond CTDI. *Med. Phys.*, 30(6):1272–1280.

Dixon, R. L. and Ekstrand, E. E. (1978). A film dosimetry system for use in computed tomography. *Radiology*, 127:255–258.

FDA (2003). Code of federal regulations: Performance standards for ionizing radiation emitting products. Technical Report 21CFR 1020.33.

Goldman, L. W. and Fowlkes, J. B., editors (1995). *Medical CT and Ultrasound*. Advanced Medical Publishing.

Herman, G. T. (1980). *Image Reconstruction from Projections: The Fundamentals of Computerized Tomography*. Academic Press, New York.

Hounsfield, G. N. (1973). Computerized transverse axial scanning (tomography). *Br. J. Radiol.*, 46:1023–1047.

Huda, W. and Atherton, J. V. (1995). Energy imparted in computed tomography. *Med. Phys.*, 22(8):1263–1269.

ICRP60 (1991). 1990 recommendations of the International Commission on Radiological Protection. Technical Report 60, Internation Commission on Radiological Protection, Oxford: Pergamon Press.

ImPACT (2001). Information leaflet no. 1: CT scanner acceptance testing. Technical report, Imaging Performance Assessment of CT Scanners,

Medicines and Health Care Products Regulatory Agency, St. George's Hospital, London, UK. Available from http://www.impactscan.org.

ImPACT (2004). ImPACT CTDI Tables. Technical report, Imaging Performance Assessment of CT Scanners, Medicines and Health Care Products Regulatory Agency, St. George's Hospital, London, UK. http://www.impactscan.org.

Jones, D. G. and Shrimpton, P. C. (1993). Survey of CT practice in the UK-part 3: normalized organ doses calculated using Monte Carlo techniques. Technical Report R250, National Radiological Protection Board (NRBP), London:HMSO.

Jucius, R. A. and Kambic, G. X. (1977). Radiation dosimetry in computed tomography. *Proc. SPIE*, 127:286–295.

Kachelriess, M., Ulzheimer, S., and Kalendar, W. (2000). ECG-correlated image reconstruction from subsecond multi-slice spiral CT scans of the heart. *Med. Phys.*, 27(8):1881–1902.

Kalendar, W. A. (2000). *Computed Tomography.* Publicis MCD Verlag, Munich.

Khan, F. M. (1994). *The Physics of Radiation Therapy.* Williams and Wilkins, Baltimore, MD, 2nd edition.

Knox, H. H. and Gagne, R. M. (1996). Alternative methods of obtaining the computed tomography dose index. *Health Phys.*, 71(2):219–224.

Leitz, W., Axelsson, B., and Szendro, G. (1995). Computed tomography dose assessment-a practical approach. *Radiat. Prot. Dosimetry*, 57:377–380.

Lewis, M. A. (2001). Multislice CT: opportunities and challenges. *Br. J. Radiol.*, 74:779–781.

McCrohan, J. L., Patterson, J. F., Gagne, R. M., and Goldstein, H. A. (1987). Average radiation doses in a standard head examination for 250 CT systems. *Radiology*, 163:263–268.

McGhee, P. L. and Humphreys, S. (1994). Radiation dose associated with spiral computed tomography. *Can. Assoc. Radiol. J.*, 45(2):124–9.

McNitt, M., Cagnon, C., Solberg, T., and Chetty, I. (1999). Radiation dose in spiral CT: The relative effects of collimation and pitch. *Med. Phys.*, 26:409–414.

Nagel, H. D. (2000). *Radiation Exposure in Computed Tomography.* European Coordination Committee of the Radiological and Electromedical Industries.

Nickoloff, E. L., Dutta, A. K., and Lu, Z. F. (2003). Influence of phantom diameter, kVp and scan mode upon computed tomography dose index. *Med. Phys.*, 30(3):395–402.

Oliveira, A. D., Alves, J. G., Carvalho, A. F., and Carreiro, J. V. (1995). Dose profile and dose index analysis in computed tomography. *Radiat. Prot. Dosimetry*, 57:387–391.

OOPEC (1999). European guidelines on quality criteria for computed tomography. Technical Report Report 16262, Office for Official Publications of the European Communities.

Pavlicek, W., Horton, J., and Turco, R. (1979). Evaluation of the MDH Industries, Inc. pencil chamber for direct beam CT measurements. *Health Phys.*, 37:773–774.

Radon, J. H. (1986). On determination of functions from their integral values along certain manifolds. *IEEE Transactions on Medical Imaging*, MI-5(4):170–176. English translation of the original 1917 paper.

Rothenburg, L. and Pentlow, K. (1995). *Medical CT and Ultrasound*, chapter CT Dosimetry and Radiation Safety, pages 519–553. Advanced Medical Publishing, Madison, WI.

Shope, T. B., Gagne, R. M., and Johnson, G. C. (1981). A method for describing the doses delivered by transmission x-ray computed tomography. *Med. Phys.*, 8(4):488–495.

Shope, T. B., Morgan, T. J., Showalter, C. K., Pentlow, K. S., Rothenberg, L. N., White, D. R., and Speller, R. D. (1982). Radiation dosimetry survey of computed tomography systems from ten manufacturers. *Br. J. Radiol.*, 55(649):60–9.

Shrimpton, P. C., Jones, D. G., Hillier, M. C., Wall, B. F., Le Heron, J. C., and Faulkner, K. (1991). Survey of CT practice in the UK-part 2: Dosimetric aspects. Technical Report R249, National Radiological Protection Board (NRBP), London:HMSO.

Spokas, J. J. (1982). Dose descriptors for computed tomography. *Med. Phys.*, 9(2):288–92.

Suess, C., Kalendar, W. A., and Polacin, A. (1995). *Medical CT and Ultrasound*, chapter Performance Evaluation and Quality Control in CT. Advanced Medical Publishing, Madison, WA.

Suzuki, A. and Suzuki, M. N. (1978). Use of a pencil-shaped ionization chamber for measurement of exposure resulting from a computed tomography scan. *Med. Phys.*, 5(6):536–9.

Tsai, H. Y., Tung, C. J., Huang, M. H., and Wan, Y. L. (2003). Analyses and applications of single scan dose profiles in computed tomography. *Med. Phys.*, 30(8):1982–1989.

Van Dyk, J. (1999). *The Modern Technology of Radiation Oncology*. Medical Physics Publishing, Madison.

Zink, F. E. and McCollough, C. H. (1994). The measurement of radiation dose profiles for electron-beam computed tomography using film dosimetry. *Med. Phys.*, 21(8):1287–1291.

Chapter 3

Materials and Methods

In the previous chapters, it was pointed out that the phantom lengths used in CT dosimetry are perhaps too short to account for the long-range scatter tails of the single scan dose profiles (SSDPs). The use of 10 cm long pencil ion chambers for the measurement of the dose-length product and hence CTDI was probably inspired by the incorrectly extrapolated SSDPs. The purpose of this chapter is to describe a new method of measuring SSDPs using a longer, water-equivalent phantom that better mimics the scattering properties in the abdomen of a real patient. A new experimental method of measuring the accumulated dose at the center of the scan length $D_L(0)$ using a non-pencil ion chamber in the plastic-water phantom is also described.

This work was carried out on two CT systems which are briefly described in regards to the operating parameters that affect dose. Two commercially available phantoms used here for the measurement of the SSDP and $D_L(0)$ are briefly discussed. Since the operating principles of ion chambers and TLDs are well-described in text books (e.g., Attix (1986)), only brief details of the particular ion chambers and TLDs used in this work are provided. The construction, detection mechanism, priming and operating characteristics of a diamond detector, used in this work for measuring SSDPs, are discussed in greater detail.

3.1 CT Equipment

3.1.1 PQ5000 Single-Slice Scanner

The PQ5000 (Philips Medical Systems, Andover, MA) is a single slice, fourth-generation system with 4800 solid state detectors. There is no detector collimator present. This machine is used primarily for treatment planning in radiotherapy of cancer, as opposed to radiological diagnosis. The available technique parameters on the PQ5000 that affect patient dose are given in Tab. III.a. The anode-cathode axis of the x-ray tube is parallel to the axis or rotation (z-axis) with the anode in the direction of the patient's feet when positioned head-first on the couch. This orientation of the tube along the z-axis reduces any photon fluence gradients across the slice plane ($x - y$) directly due to the heel effect, which would ultimately result in non-uniform noise characteristics in tomographic images.

In this study, all doses were measured with the PQ5000 at an x-ray tube potential of 130 kVp (8.5 mm Al half-value layer (HVL)) using the large focal spot. The machine's body bow-tie filter was engaged during all measurements. As will be discussed in much greater detail in forthcoming sections, relative SSDPs and accumulated dose $D_L(0)$ were measured in a plastic-water phantom for nominal slice widths of 3, 5, and 10 mm. Both helical and 360°-axial acquisition modes were used in measuring $D_L(0)$. Relative SSDPs were also measured in standard CTDI phantoms using 3 mm and 5 mm slice widths in the head and body phantoms respectively.

Table III.a: Selectable operating parameters on the PQ5000 single-slice scanner that affect the patient dose.

Parameter	Values
Slice width (mm)	1.5, 2, 3, 4, 5, 8 and 10
Tube potential (kVp)	80, 100, 110, 120, 130, 140
mA range	30 - 400 mA
Scan time (s)	1, 1.5, 2, 4
Pitch selections	0.5 - 3.00 in steps of 0.25
Scan interval (axial)	-50 mm to +50 mm in steps of 0.5 mm.

Table III.b: Selectable operating parameters on the MX8000 Quad multi-slice scanner that affect the patient dose.

Parameter	Values
Slice width (mm)	0.5, 1, 2, 2.5, 4, 5, 8, 10, 16, 20
Tube potential (kVp)	90, 120, 140
mA range	28-500 mA in steps of 1 mA
Scan time (s)	0.5 - 2.0 in steps of 0.25
Pitch selections	0.25 - 1.75 in steps of 0.025
Scan interval (axial)	-20.0 to 20.0 times T in steps of 0.1.

3.1.2 MX8000 Quad Multi-Slice Scanner

In order to ensure that the methods developed herein were applicable to a CT system other than the PQ5000, less extensive dose measurements were made on a MX8000 Quad (Philips Medical Systems, Andover, MA) multi-slice, third-generation scanner. This CT unit is used in our clinic primarily for diagnostic radiology. The detector array consists of ceramic scintillating detectors of variable size arranged in a so-called adaptive array (Chen et al., 2000) shown in Fig. 3.1. The detector elements are wider away from the center of the array for a total z-axis detector length of 20 mm. Detector collimators are present in the system to reduce the detection of scattered photons. The slice thickness and number of contiguous slices n $(= 1, 2, 4)$ are chosen by beam collimation, detector collimation and by electronic selection and/or summation of detector signals. The available technique parameters that affect patient dose, including the slice widths, are given in Tab. III.b.

The anode-cathode axis is oriented parallel to the z-axis with the anode in the

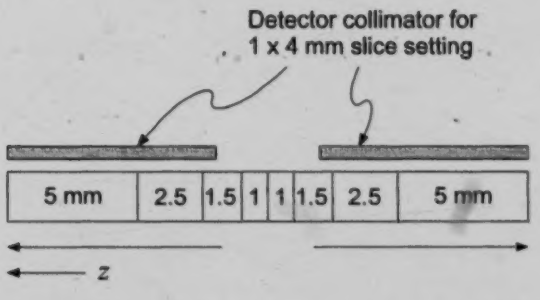

Figure 3.1: Detector elements in the adaptive array of the MX8000 multi-slice scanner. Also shown is an example configuration of the detector collimator for a 1×4 mm slice selection.

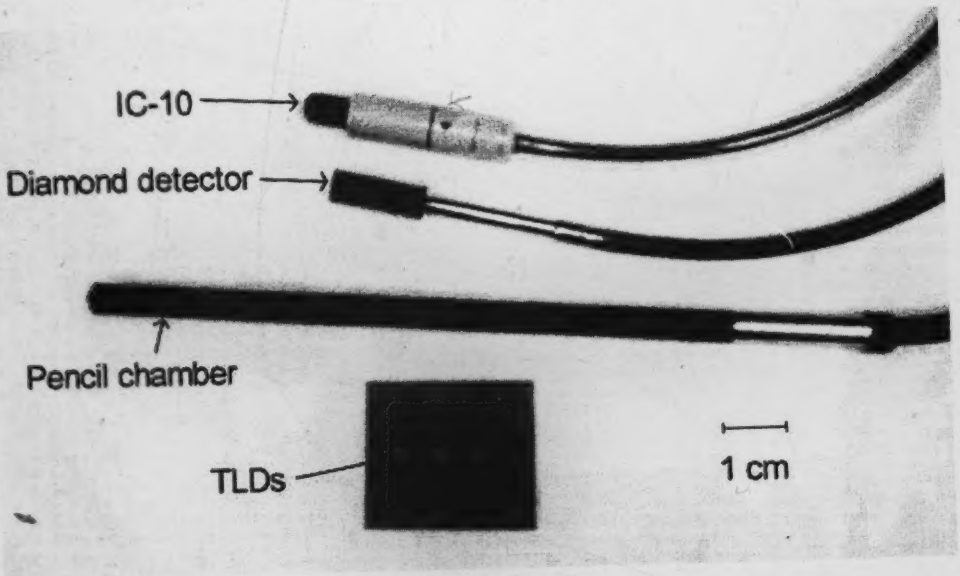

Figure 3.2: Detectors used in this study (from top to bottom): Wellhöfer IC-10 ionization chamber, PTW diamond detector, Capintec PC-4P pencil ionization chamber and lithium fluoride (LiF) thermoluminescent dosimeters (TLDs).

direction of the patient's feet when positioned head-first on the couch.

In this work, the MX8000 was operated at 120 kVp (9.2 mm Al HVL) using the large focal spot and with the machine's body bow-tie filter engaged for all measurements. Using the CIRS phantom, relative SSDPs were measured for fused slice selections ($n \times T$) of 1×4 mm, 1×10 mm and 1×20 mm while absolute $D_L(0)$ was measured in 360°-axial acquisition mode for slice selections of 1×10 mm and 1×20 mm.

3.2 Dosimeters

Figure 3.2 shows all the detectors used in this experimental investigation of CT dosimetry. From top to bottom in Fig. 3.2: a Wellhöfer IC-10 ionization chamber (Scanditronix Wellhöfer North America, Bartlett, TN) used for measuring absolute accumulated dose $D_L(0)$ and a single relative SSDP, a PTW diamond detector (PTW, Freiburg, Germany) used as the primary detector for measuring relative SSDPs, a Capintec PC-4P pencil ionization chamber (Capintec, Inc., Ramsey, NJ) used to measure absolute $CTDI_{100}$, and lithium fluoride (LiF) thermoluminescent dosimeters (TLDs), TLD-100 (Thermo Elec-

tron RM&P, Roswell, GA) used for measuring a single relative SSDP. The single SSDP that was measured using both the IC-10 and TLDs was acquired only for the verification of the SSDP measured with the diamond detector. All detector properties and their applications in this work are discussed in greater detail in the following sections. Since the use of diamond detectors for CT dosimetry and kilovoltage-energy photon beam dosimetry in general is relatively new, the basic operation and detection mechanisms as well as the characteristics of the diamond detector will be discussed in greater detail than for the other dosimeters.

3.2.1 Diamond Detector

3.2.1.1 Basic Properties

Diamond detectors possess many desirable characteristics for dosimetry including near tissue equivalence ($Z = 6$ compared to $Z_{eff} = 7.4$ for soft tissue (Khan, 1994)), very good spatial resolution (< 0.4 mm when oriented perpendicular to the beam direction) and high sensitivity [~ 2 nC/cGy (Rustgi, 1995)] due to the relatively low energy (13 eV) required for ion pair formation (Mainwood, 2000). Air-filled ion chambers are less sensitive than a diamond detector since it takes 33.97 eV to produce an ion pair in air (Boutillon and Perroche-Roux, 1987). Diamond detectors exhibit a low level of leakage current, are highly radiation resistant (Planskoy, 1980) and their response is nearly temperature-independent varying $< 0.1\%/°C$ over the range from 15°C to 40°C (De Angelis et al., 2002). The diamond detector is used in our clinic primarily for measuring relative dose of megavoltage therapy beams. This includes step and shoot IMRT field segments containing small sub-fields where the dose gradients are large.

The operating parameters of the PTW Riga Type 60003 diamond detector used in this work are given in Tab. III.c as supplied by the manufacturer. The PTW diamond detector's sensitive volume is a low-impurity natural diamond plate with a density of 3.51 g/cm^3 (Mobit and Sandison, 1999) sealed within a cylindrical polystyrene housing of 7.3 mm outer diameter as shown in the schematic in Fig. 3.3. The effective point of measurement is 1 mm below the end of the housing. Thin gold electrodes biased to a nominal potential of +100 V sandwich the diamond crystal providing the applied electric field in the crystal. The positively biased electrode is also connected to a pre-

Table III.c: Operating parameters of the PTW Riga Type 60003 diamond detector as supplied by the manufacturer.

Characteristic	Nominal value
Operating bias	+100 V (±1%)
Dark current	$\leq 5\times 10^{-12}$ A
Sensitive volume	1.7 mm^3
Sensitive area	6.8 mm^2
Thickness of sensitive volume	0.25 mm
Pre-irradiation dose	> 2 Gy
Directional response	$\leq$ 2% in the range of 0°-170°
Sensitivity to ^{60}Co radiation	(0.5 – 5.0) nC/cGy

amplifier circuit to measure the charge. The pre-amp is isolated from +100 V by a capacitor (see Fig. 3.4). Of special interest to measuring CT dose profiles is the sensitive volume thickness of 0.25 mm that provides an approximately four-fold improvement in spatial resolution over common TLDs (TLD-100; see Sec. 3.2.4). This was the primary motivating factor in choosing the diamond detector for measuring SSDPs in this work.

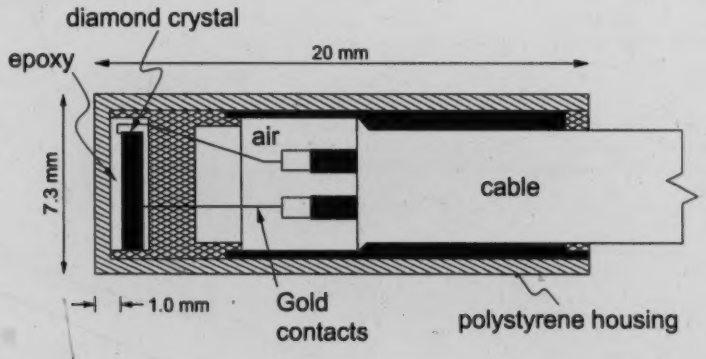

Figure 3.3: Schematic of a PTW diamond detector.

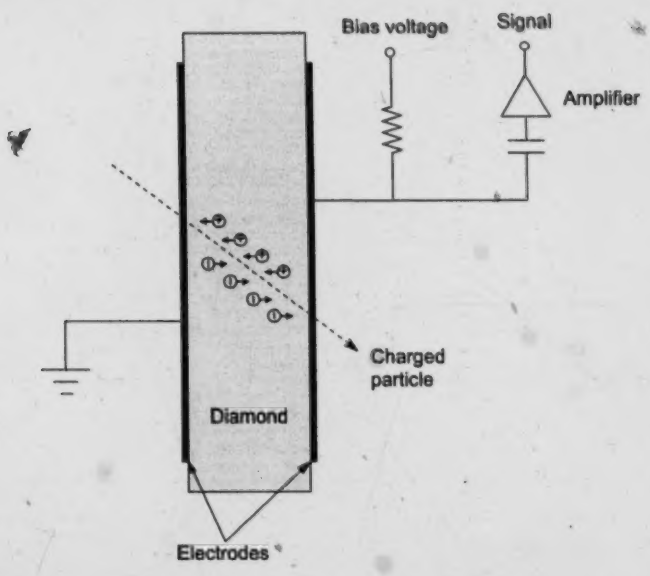

Figure 3.4: Basic outline of the charged particle detection mechanism of in a diamond detector.

3.2.1.2 Detection Mechanism

Comprehensive descriptions of the detection mechanism of the diamond detector to ionizing radiation can be found in Mainwood (2000) and Tapper (2000). An abbreviated description is provided below.

Figure 3.4 shows the basic detection process in a diamond detector which effectively acts as a solid-state radiation detector. When an energetic charged particle passes through the sensitive volume, for example the electrons liberated from x-rays interacting with the surrounding medium, the charged particle can ionize the carbon atoms promoting electrons to the conduction band and creating holes in the valence band. As a general rule for semiconductors, the formation of electron-hole pairs requires about three times the band gap energy. In the case of diamond, it takes $\sim$ 13 eV to create an ion pair since the band gap energy of diamond is 5.5 eV. The number of electron-hole pairs created is approximately proportional to the energy lost by the incident charged particle. For particles with speeds greater than about 0.95c where c is the speed of light in a vacuum, the ionization rate varies slowly with energy and is known as a minimum ionizing particle (MIP) In diamond, about 36 ion pairs are created per μm travelled by a MIP. In the presence of an applied electric field, the charge carriers created in the diamond crystal migrate toward the

electrodes, inducing a charge on the electrodes proportionate to the relative velocities between the electrons and holes (Ramo, 1939). This constitutes the primary current in the detector. The ion pairs do not actually have to reach the electrodes to generate a current. Those electrons and holes which are not trapped at impurity sites, stopped at the boundaries or do not recombine, may reach the electrodes additionally contributing to the measured signal. Recombination can be minimized by applying a large voltage.

3.2.1.3 Priming

Some of the electron-hole pairs created by charged particle interactions in diamond get trapped at impurity sites within the crystal (mainly nitrogen for the PTW detector) and eventually build up to form space charges. These give rise to an electric field opposite in direction to the applied field, thus polarizing the crystal. The result is a reduction in the current since the diamond detector operates approximately as a resistive element, with current varying almost linearly with the effective electric field for a given dose rate (Hoban et al., 1994). Therefore the detector response tends to initially decrease with absorbed dose due to polarization. This effect can be overcome by pre-irradiating or priming the diamond detector, thereby establishing an equilibrium population of traps (Hoban et al., 1994) and stabilizing the response. The manufacturer's recommended pre-irradiation dose is > 200 cGy. Hugtenburg et al. (2001) reported less than 1% variation in readings for the same model detector after delivering 250 cGy using 45 kVp and 100 kVp beams.

3.2.1.4 Energy Dependence

The near-tissue equivalence of diamond ($Z = 6$) stated earlier leads to a flat relative air-kerma response for photon energies $\gtrsim$ 200 keV (Planskoy, 1980) since the ratio of mass energy absorption coefficients of carbon to air $(\mu_{en}/\rho)^{C}_{air}$ varies slowly. However at energies $\lesssim$ 200 keV, $(\mu_{en}/\rho)^{C}_{air}$ varies considerably due to the roughly Z^3 dependence of the photoelectric cross section. Additionally, the relative air-kerma response of diamond detectors is known to depart from this ratio (Seuntjens et al., 1999; Yin et al., 2004) due most likely to photoelectrons created in the high-Z contacts used to bias the diamond crystal. Using a three-component model of energy absorption (i.e., C, Ag, and Cu), Yin et al. (2004) found a much better agreement between the measured rel-

ative air-kerma response curve and the $(\mu_{en}/\rho)_{air}^{C-Ag-Cu}$ curve for their PTW diamond detector which had silver and copper contacts (compared to the gold contacts in the PTW detector used in this study). Their response curve showed that the relative air-kerma response varied by about 50% over mean x-ray energies of $\sim 30-100$ keV, implying that reference/absolute dosimetry at these energies using the diamond detector is problematic.

3.2.1.5 Directional Dependence

An important consideration for beam profile measurements is the directional response of detectors to radiation. The diamond detector may respond differently to the scattered radiation reaching the front face of the detector compared to radiation incident from the cable side. The response in the plane of the detector axis of a PTW Riga diamond detector has been studied by Rustgi (1995) using ^{60}Co, 6 MV and 18 MV photon beams. No significant change in sensitivity with angle was found for angles up to 135° (with the 0°-180° line corresponding to the detector-cable axis). No measurements were made beyond 135°. Under the same geometry and using the same model detector, De Angelis et al. (2002) reported no significant change in response for $< 100°$ compared to the response at 0° and an increase in response (up to 2%) in the range 100° - 270°, as measured in a spherical PMMA phantom and a 6 MV beam. The PTW manual for the Riga detector states a $< 2\%$ change in relative air-kerma response over 0°-170° for measurements made in a ^{60}Co beam ($\overline{E} = 1.25$ MeV). There is no literature regarding the angular dependence of the PTW diamond detector at kilovoltage energies. However, as will be shown in the next chapter, the slight directional dependence of the PTW diamond detector contributes to a slight asymmetry in the measured SSDPs.

3.2.1.6 Dose Rate Dependence

Diamond detectors have been shown to display a slight sub-linearity with dose rate due to charge recombination in the high-density crystal (Hoban et al., 1994; Findanzio et al., 2000; Barnett, 2004; Hugtenburg et al., 2001). For solid state detectors in general, the relationship between the current I and the dose rate $\dot{D}$ has been shown as $I \propto \dot{D}^{\Delta}$ (Fowler, 1966), where the value of the exponent Δ depends on the concentration of crystal impurities. The main impurities in the PTW diamond detector are nitrogen and boron ($< 10^{-19}$

atoms cm^{-3})(Heydarian et al., 1993). For the same model PTW diamond detector as used in this study, Hugtenburg et al. (2001) found Δ values of 0.970 ± 0.015 and 0.975 ± 0.003 for 45 kVp and 100 kVp beams respectively and stated, based on their results and a literature review, that Δ values are energy independent in the range 50 kVp to 6 MV. For the actual PTW diamond detector used in our work, Barnett (2004) found an average Δ value of 0.995 ± 0.002 for energies in the range of ^{60}Co to 15 MV. Therefore assuming energy independence of Δ, the dose-rate dependence of the diamond detector can safely be neglected for the current work.

3.2.2 Pencil Ion Chamber

The pencil ionization chamber used in this study was a Capintec PC-4P which is described in detail by Suzuki and Suzuki (1978). As stated on the manufacturer's certificate accompanying our PC-4P chamber, the PC-4P cylindrical pencil chamber has an active length of 102 mm, a 3 mL active volume (air), 0.3 mm thick walls constructed from Shonka C552 air-equivalent plastic ($\rho = 1.76$ g/cm^3) and a 7.0 mm outer diameter. The central electrode is also made from air-equivalent plastic. Venting to the atmosphere is provided via a small canal to a hole near the detector tip. Jucius and Kambic (1977) showed $< 3\%$ change in energy response for the PC-4P over effective energies of 25 keV to 100 keV, and $< 5\%$ variation in response over the 10 cm active length when exposed to a 1 mm×25 mm x-ray beam covering the detector diameter. The manufacturer's certification sheet stated $< 2\%$ change in response over HVLs ranging from 1.85 mm Al to 18.00 mm Al (70 kVp to 250 kVp), measured using a GE Maxitron x-ray unit.

3.2.3 IC-10 Ion Chamber

A Wellhöfer IC-10 ionization chamber with a 0.14 cm^3 active volume was used in this study primarily for reference dosimetry measurements of the accumulated CT dose, i.e., $D_L(0)$. It was also used to measure a single relative SSDP to verify the profile shape measured using the diamond detector. As shown in Fig. 3.5, the nearly spherical active volume of the IC-10 has a 3.0 mm radius and a 3.3 mm active length along the 6 mm diameter cylindrical part. The effective center of the active volume lies 4.1 mm from the end of the chamber. The 1 mm diameter central electrode, 0.4 mm thick chamber wall and guard

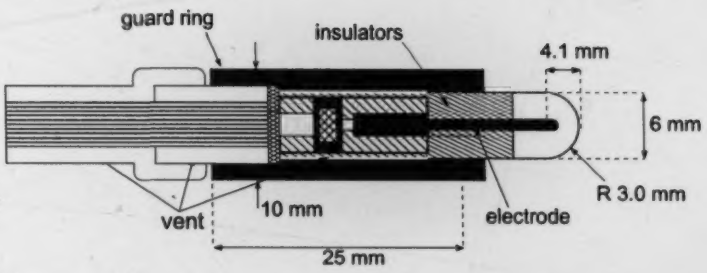

Figure 3.5: Schematic of the Wellhöfer IC-10 ion chamber used in this study for verification of the SSDP measured with the diamond detector, and for measuring accumulated dose.

ring are all constructed from Shonka C552 air-equivalent plastic. Venting to the atmosphere is provided through a hose in the chamber cable. The IC-10 chamber is traditionally used for relative dosimetry of therapeutic photon and electron beams in air or in phantom, including water phantoms since the chamber is fully water-proof. Example applications within our clinic are the measurement of treatment beam profiles and percent depth dose curves. Because of its relatively small active volume, it is increasingly being used for small-field dosimetry such as in IMRT fields. For the present work, the 3.3 mm active length was the motivating factor in choosing this particular detector over others for CT accumulated dose measurements since we wanted to minimize volume averaging effects when measuring the high dose gradient regions of the SSDP. The only other ion chamber available in our clinic with a comparable active length was the PTW Type 31006 PinPoint chamber (PTW, Freiburg, Germany) with a 5 mm active length. However, the PinPoint chamber is known to over-respond at low energies due to photoelectric interactions with the chamber's steel electrode as reported by Martens et al. (2000) who explored the use of the PinPoint chamber in 6 MV and 15 MV beams. Therefore, due to the over-response to low-energy photons and the larger active length, the PinPoint chamber was deemed inferior to the IC-10 for measuring accumulated CT dose and thus was not chosen for use in this study.

3.2.4 TLDs

The thermoluminescent dosimeters (TLDs) used in this study were purchased from Thermo Electron under the name TLD-100. These are 3 mm $\times$3 mm $\times$0.9 mm lithium fluoride (LiF) chips with a density of 2.64 g/cm^3 and an

effective atomic number of 8.2 (Khan, 1994). The crystalline LiF in TLD-100 chips is doped with small quantities of Mg and Ti and are thus denoted LiF:Mg, Ti. Davis et al. (2003) reported a relative dose response variation for TLD-100 of less than 3% over mean x-ray energies 32.5 - 82.6 keV and thus show only a minor energy dependence in the range of CT energies.

Due to their small size, TLDs are useful dosimeters in general for regions where ion chambers cannot be used. For example, TLDs may be directly inserted into patient cavities and tissues. They are also commonly used in personal dose monitors (badges). With regards to CT dosimetry, the small size of the TLD is beneficial for measuring SSDPs especially in the high dose gradient regions where larger volume ion chambers may introduce significant volume averaging effects. Since TLDs are essentially the only dosimeters currently used for measuring in-phantom SSDPs in CT, TLDs were utilized in this study for measuring a single SSDP in order to compare and thus verify the shape of a SSDP measured (for the same slice width) using the diamond detector. In other words, the TLD is taken here as the "gold standard" dosimeter for SSDP measurement with which to compare the method using the diamond detector that is introduced in this study.

3.3 Phantoms

3.3.1 CIRS Plastic Water Phantom

Relative SSDPs and accumulated doses were measured in a Computerized Imaging Reference Systems (CIRS) Model 002H5 homogeneous intensity modulated radiotherapy (IMRT) phantom (CIRS, Inc., Norfolk, VA) made from water-equivalent plastic. The phantom, shown in Fig. 3.6(a), is designed to approximate the body size of a real patient. It has an elliptical cross-section with major and minor axes of 30 cm and 20 cm respectively, and is comprised of two 15 cm long sections for a 30 cm total length. One section houses longitudinal (removable) rods for contrast media and rods with cavities for detectors (ion chambers, TLDs, etc.), while the other section is homogeneous. Both sections sit on a flat, water-equivalent alignment base which was present for all measurements. The surfaces of the phantom are etched which enables (reproducible) alignment of the cross-sectional $(x - y)$, sagittal $(y - z)$ and coronal $(x - z)$ phantom planes within the scanner using the scanner's laser

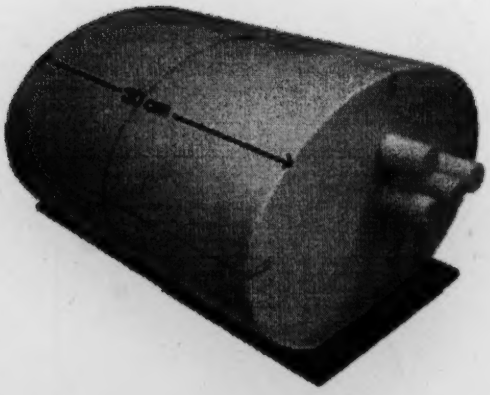

(a) The CIRS homogeneous phantom made from water-equivalent plastic. The rod shown at the center contains a cavity for insertion of a detector.

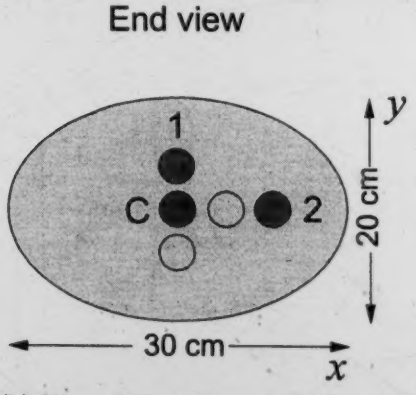

(b) The radial positions studied: center (C), off-axis positions (1) and (2).

Figure 3.6: CIRS homogeneous plastic water phantom used in this study.

alignment system. All plastic water rods used in this study for this phantom were purchased from CIRS including those containing cavities which are manufactured specifically for a given detector. The single exception was for the PC-4P pencil chamber where the rod designed for the PTW diamond detector was used since the nominal outer diameters of the detectors differ by only 0.3 mm. The CIRS phantom was chosen primarily because of its length, over twice as long as standard CTDI phantoms, thereby providing sufficient inward sidescatter to a detector located at the center of the scan length (and phantom) from scans centered near the phantom edges. An added benefit is the phantom's water-equivalence (0.8% difference from water in the linear attenuation coefficients for 60 keV photons as stated by the manufacturer) which provides a more realistic estimate of dose to a patient than the standard CTDI phantoms constructed from PMMA.

Three radial positions were studied and are shown in Fig. 3.6(b): the center (C), an off-axis position at 6 cm depth along the (vertical) minor axis ("Off-axis 1") and an off-axis position at 7 cm depth along the (horizontal) major axis ("Off-axis 2").

3.3.2 PMMA (CTDI) Phantoms

Relative SSDPs were also measured in standard CTDI phantoms to investigate the effects of phantom shape, length and composition on the measured SSDP and since these are the most common phantoms for measuring CT dose. The two cylindrical PMMA phantoms (Fig. 2.4) are 14 cm long with diameters of 32 cm (body) and 16 cm (head). The mid-point of the phantom lengths are etched on the surface around the entire perimeter. Both phantoms contain 1.3 cm diameter bores along the central and peripheral locations (parallel to the central axis) that accommodate detectors. Detector sleeves to be inserted in the CTDI phantom bores, shown in Fig. 3.7 for the Wellhöfer IC-10 ion chamber and the PTW diamond detector, were manufactured in house as 14 cm long, 1.3 cm outer diameter cylindrical PMMA rods with cylindrical cavities of sufficient diameter to snugly hold the detectors. The rods were designed such that when inserted into the phantoms, the mid-point of the active length of each detector coincided with the mid-point of the phantom length ($z = 0$) with the detectors completely inserted into the rod cavities. The PMMA rod for the PC-4P pencil chamber was supplied with the chamber

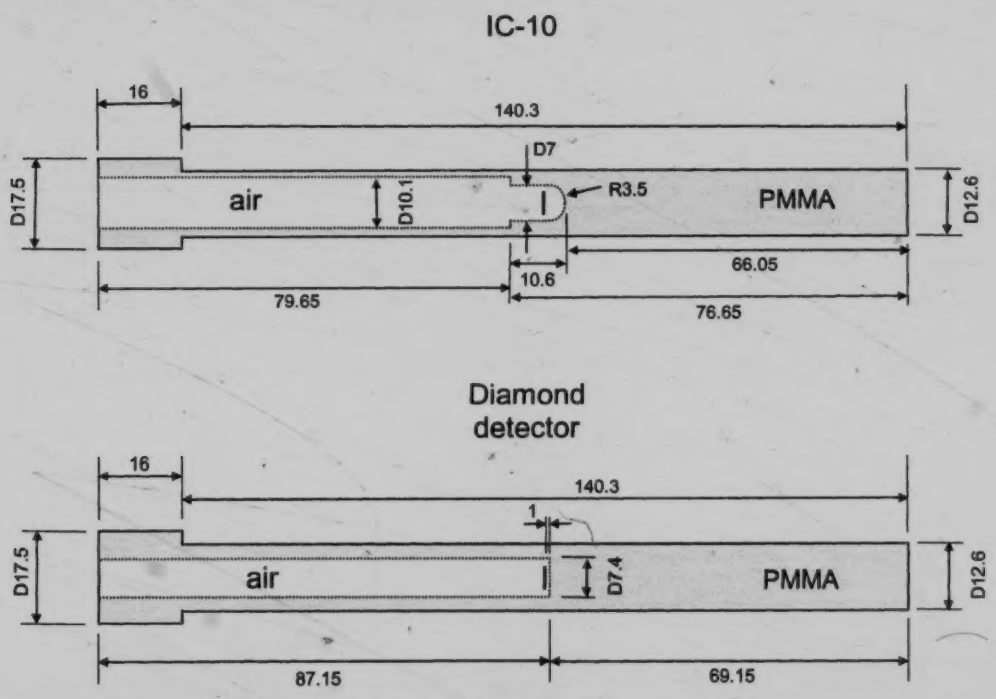

Figure 3.7: Schematic of the detector rods manufactured in house to be inserted into the PMMA CTDI phantoms for an IC-10 ion chamber and PTW diamond detector. All dimensions are in mm.

when purchased from Capintec and has the same outer dimensions as the rods built in house for the IC-10 and diamond detector (the Capintec rod was used as the prototype design for rods built in house). Phantom bores that did not contain a detector rod were filled with homogeneous PMMA rods supplied with the phantom.

For all measurements, the central axis of each phantom was aligned with the rotational axes of the CT scanners using the alignment lasers in the CT ring. Figure 3.8 shows the basic experimental set up for dose measurements, in this case for the PTW diamond detector at the central axis of the CIRS phantom on the PQ5000 scanner couch. The positive direction of the longitudinal z-axis is represented as the outward movement of the couch from the CT bore.

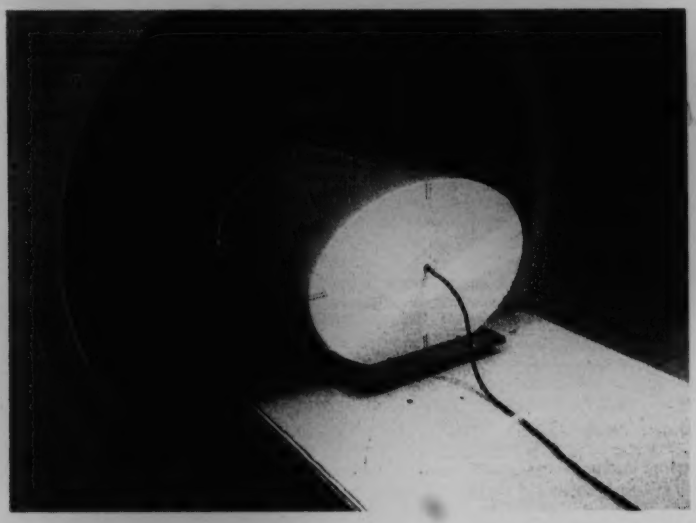

Figure 3.8: Experimental setup of the CIRS phantom and the PQ5000 CT scanner. The diamond detector is inserted along the central axis of the phantom.

3.4 Single Scan Dose Profile Measurements

3.4.1 Diamond Detector Operation

Relative SSDPs were measured using the PTW diamond detector connected to a Capintec Model 192 electrometer (Capintec, Inc., Ramsey, NJ), with the diamond detector biased at $+100.0 \pm 0.1$ V using a CNMC Model EB100 power supply (CNMC Company Inc., Nashville, TN). The bias voltage was confirmed using a Marcraft SE-1038 digital multi-meter (Marcraft International Corp., Kennewick, WA) and adjusted as necessary via a potentiometer in the power supply. Prior to any measurements, the diamond detector was irradiated in the CT beam to an air-kerma > 200 cGy to stabilize the response (as recommended by the manufacturer). This was performed by taping the detector directly to the couch (no phantom present) with the detector and CT rotational axes approximately coincident. The position of the diamond crystal within the detector housing (1 mm from the end) and the CT scanner isocenter were then approximately aligned using the bore alignment lasers. The largest collimator slice width on each scanner was usually chosen to ensure the diamond crystal was fully irradiated in the primary beam, thus speeding up the process. Since no exposure calibration factor was ever determined for the diamond detector

(relative dosimetry only), the air-kerma values (i.e., > 200 cGy) for the scan settings used for the diamond pre-irradiation were measured using the IC-10 chamber for which N_X *was* measured (see Sec. 3.5.1).

Due to the energy-dependent response of the diamond detector at kilovoltage energies (Section 3.2.1.4), obtaining absolute (i.e., non-relative) dose profiles is non-trivial due to: (1) any differences in the CT and calibration beam qualities, (2) changes in beam quality at depth in phantom due to beam hardening and increased scatter and (3) possible changes of quality with z along the profile since the scattered photons will be lower in energy than primary photons. Point (1) is especially relevant in this case since the only x-ray machine in our clinic with a beam quality similar to the CT beam, and for which the dose output is accurately known, has an HVL of 5 mm Al (see the end of Sec. 3.4.4) compared to $\sim$ 9 mm Al for the CT beams. However, absolute profiles were not the goal of this investigation and therefore all SSDPs to be presented will be normalized to the peak reading. This factors out points (1) and (2).

3.4.2 Measurement Method

3.4.2.1 CIRS Phantom

SSDPs were measured by fixing the diamond detector at the mid-point of the CIRS phantom length (and scan series, $z = 0$; Fig. 3.6) and axially scanning the entire length of the phantom at several discrete longitudinal positions to adequately sample the dose profile. This is illustrated in Fig. 3.9 where the phantom translates stepwise through the CT beam (by moving the couch between irradiations) measuring the primary and scattered radiation at each z position, thus building up the SSDP.

As a first step in the SSDP measurement process, the $z = 0$ position for the CIRS phantom was determined by first fully inserting the diamond detector (and rod) in the phantom and marking the detector cable at the point coincident with the end of the phantom. The detector was then removed and the distance between the end of the detector and the cable marking was measured with a ruler. A fiducial marker (line drawn on masking tape) was then placed on the phantom's top surface at the measured distance minus 1 mm (since the sensitive volume is recessed from the end of the housing by this amount) from the cable end of the phantom. After aligning the sagittal and

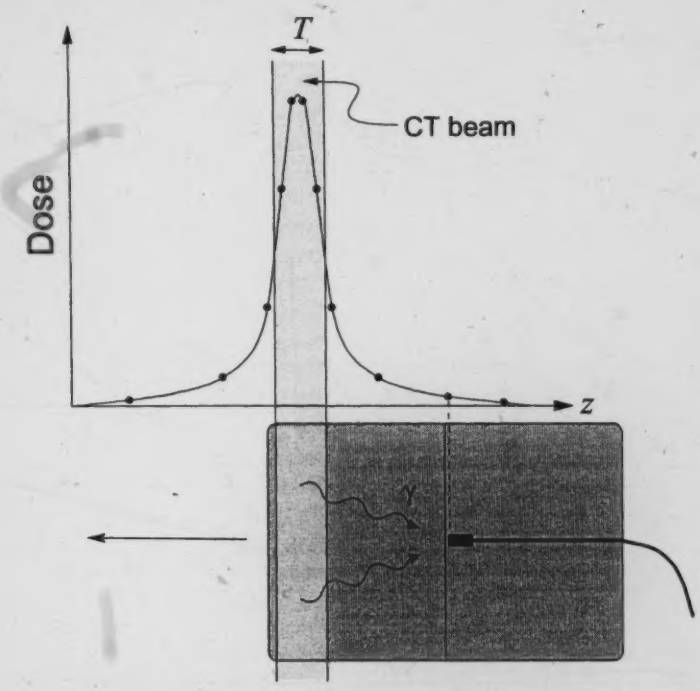

Figure 3.9: Illustration of the method used to measure a SSDP. The PTW diamond detector, at a position in the phantom corresponding to $z = 0$ of the profile, translates through the CT beam rotating at a fixed z position and measures the primary and scattered radiation at each z location.

coronal etched phantom markers and the (z-axis) fiducial detector marker with the CT lasers, final z adjustments were made by irradiating the phantom at 0.5 mm intervals on either side of the detector fiducial marker using the smallest slice width available on each scanner. The point of maximum detected signal was taken as the "true" $z = 0$ position.

For measuring the SSDP, five 1 s rotations of the source were used to produce 1000−2000 mAs at each z location, depending on the slice width. The large mAs used would not generally be required for routine SSDP acquisition but was chosen to improve statistics for the present work. The accumulated charge for five rotations was taken as the reading for each longitudinal position. For most slice widths studied, the scatter tail region of the SSDP was sampled at $5 - 10$ mm intervals and down to as little as 0.5 mm intervals around the peak. Note that the SSDP's measured value at a particular longitudinal position, for any radial position in an elliptical phantom, represents the relative

primary and scattered dose averaged over one 360° rotation of the source.[1]

The conventional method of measuring SSDPs is to arrange a large number of detectors (i.e., TLDs) in the phantom along the z-axis and irradiate the phantom at the center using only a single axial slice (see Sec. 2.3.5.2). The present method reciprocates the conventional experimental set up by instead using a single detector and irradiating the phantom at a large number of longitudinal positions. Therefore, the phantom must be homogeneous in the longitudinal direction. With the current method, the sampling interval is now determined only by the minimum couch increment (0.5 mm for our scanners) and not the thickness of a TLD chip (about 1 mm).

Ideally, the length of the phantom should be twice the width of the SSDP being measured. To illustrate why, assume we have a phantom equal in length to the SSDP width. When the left edge of the phantom, for example in Fig. 3.9, is aligned with the SSDP peak, only half of the SSDP is generating scatter. Therefore an additional phantom length equal to half the SSDP width would be required at each end of the phantom to ideally measure the full SSDP. This has a minimal effect however for most z positions of the SSDP since most of the scatter is generated in the primary beam. As will be shown in the next chapter, the unequal phantom length on either side of the CT beam *will* have an effect for points near the phantom edges. This was assessed by measuring a SSDP using only one 15 cm section of the CIRS phantom. The diamond detector rod was repositioned to the mid-point of the 15 cm phantom and the resulting volume of air in the phantom bore was filled with a homogeneous CIRS rod. The $z = 0$ position was determined using the methods described in the second paragraph of this section.

3.4.2.2 CTDI Phantoms

The method for measuring SSDPs in the CTDI phantoms was almost identical as for the CIRS phantom except for alignment in the CT beam. Since there were no sagittal or coronal fiducial marks on the CTDI phantoms, the intersection point of the sagittal and coronal lasers was aligned with the center of the end of a homogeneous rod inserted at the center of each phantom. The cross-sectional lasers were then aligned with phantoms' mid-points using the perimeter etchings. The homogeneous rod was then replaced with the diamond

[1]This is true in practice even for a cylindrical phantom unless it is perfectly homogeneous azimuthally.

detector rod which, in its design, had already incorporated the coincidence of the diamond crystal with the phantom mid-point ($z = 0$). Therefore, no further z adjustment was necessary although the $z = 0$ position was verified using the same irradiation method as for the CIRS phantom. To prevent shifting of the phantom, a thin rubber non-slip mat was placed between the phantom and couch. The mat was folded over at its ends forming a jam with the sides of the phantom to prevent lateral rolling.

3.4.3 Uncertainty Assessment

The random uncertainty in the data points of the relative SSDPs was assessed by measuring five points on the SSDP for the PQ5000, 10 mm slice width (henceforth denoted PQ-10): $z = 0, \pm 50, \pm 100$ mm. At each z position, ten readings were acquired consecutively and the standard deviation of the readings was taken as the uncertainty in SSDP data points. The uncertainty in the PQ-10 SSDP data is assumed to be representative of all SSDPs.

3.4.4 Verification using Alternate Dosimeters

The general shape of the SSDP acquired with the diamond detector was verified by measuring the central axis PQ-10 profile using two alternate detectors in the CIRS phantom (position (C) in Fig. 3.6(b)): the Wellhöfer IC-10 ion chamber (3.3 mm active length) and LiF TLD chips. The SSDP was measured with the IC-10 using the same method as used with the diamond detector.

Before measuring the SSDPs using TLDs, the sensitivities of the individual chips were first normalized by calibrating them as a batch using a Pantak Therapax 300 DXT orthovoltage x-ray unit (Pantak Inc., East Haven, CT) operating at 125 kVp (5 mm Al HVL). Chips were arranged in a 12.7 cm diameter, 5.9 mm thick circular lucite tray, shown in Fig. 3.10, which had circular slots around the perimeter to hold the TLD chips face down. The TLD tray was placed inside a $25 \times 25 \times 0.64$ cm^3 sheet of lucite which in turn was laid on eight $25 \times 25 \times 1$ cm^3 sheets of solid water as shown in Fig. 3.11. The solid water was included to provide backscatter to the TLDs upon irradiation. A 20×20 cm^2, 50 cm focus to surface distance (FSD) x-ray applicator cone was placed in contact with the top lucite tray and 100 MUs were delivered. Chips were pre-annealed at 400 °C for 1 hour using a RPD Model 128 TLD Annealing Furnace (Radiation Products Design, Inc., Albertville, MN) and at

Figure 3.10: Lucite 12.7 cm diameter circular tray for holding TLDs, inserted into a $25 \times 25 \times 0.64$ cm^3 sheet of lucite (white), used for the normalization of individual TLD chip sensitivities using the Pantak x-ray unit.

room temperature for > 30 min before each irradiation, and then read after irradiating using a Harshaw 5500 automatic TLD reader (Thermo Electron RM&P, Roswell, GA). The heating rates (time-temperature profile) in the reader consisted of a preheating stage at 125°C for 15 s followed by 75°C - 325°C at 15°C/s during TL signal (charge) acquisition. The integral charge reading for an individual chip Q_i was then used to calculate an element correction coefficient (ECC) for each chip which serves as the normalization factor. With $\overline{Q}$ the average charge integral of all the chips in the batch, the ECC_i is given by $Q_i/\overline{Q}$. All Q_i were within an acceptable 7% of $\overline{Q}$ (in our clinic 10% is often considered the limit before a TLD should be discarded) and therefore

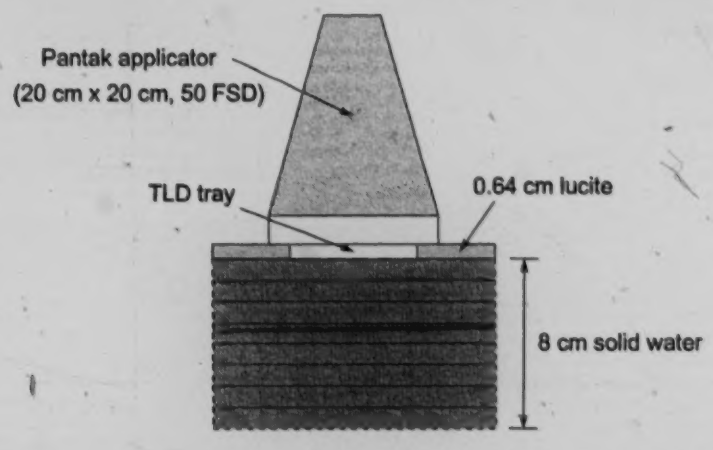

Figure 3.11: Experimental setup of the TLDs for normalizing chips sensitivities using the Pantak orthovoltage x-ray unit.

all chips were deemed usable.

Since only one of the two sections of the CIRS phantom was accessible to detectors (see Fig. 3.6(a)), obtaining the SSDP over the full 30 cm length using TLDs was not possible. The half-side of the SSDP was measured with TLDs in the standard way using a single axial scan located at the mid-point along the length of the CIRS phantom. The TLD chips of dimension $3 \times 3 \times 0.9$ mm^3 were arranged on edge in 50 mm long and 25.4 mm outside diameter CIRS plastic water rods designed for TLDs which are shown in Fig. 3.12. Three rods were abutted to fill the 15 cm long phantom cavity located at the central position denoted "C" in Fig. 3.6(b). TLDs were inserted into the 5 mm diameter cavities at the center of the rods and spaced $\sim$ 20 mm apart using CIRS plastic water plugs. The precise spacing between chips was determined as the sum of each spacer's length (measured with a digital-readout caliper) and half the chip thickness (0.45 mm). Near the center of the SSDP, eight chips were stacked face-to-face and sandwiched between the first spacer plug and the end of the homogeneous 15 cm half of the phantom. To ensure an adequate signal to the TLDs, the single scan consisted of $10 - 2$ s rotations at 350 mA producing a total of 7000 mAs. The TL signals were read within 24 hours after irradiation using the same heating rates in the TLD reader as in the calibration process. After applying the calculated ECC to the charge reading for each chip, the SSDP was normalized to the maximum charge reading corresponding to the peak of the SSDP ($z = 0$).

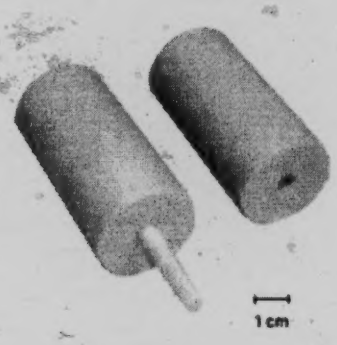

Figure 3.12: Plastic water TLD rods for insertion into the CIRS phantom. TLDs are placed on edge in the rod cavities and spaced apart using plastic water plugs.

3.5 Accumulated Dose Measurements

Maximum cumulative doses [$D_L(0)$] were measured in the CIRS plastic water phantom using the IC-10 ion chamber which measures the dose-length product while translating through the beam using an axial or helical scan series. Standard CTDIs were measured in the CIRS phantom with the Capintec PC-4P pencil ion chamber (102 mm active length) to integrate the dose-length product using a single axial scan. Both chambers were connected (separately) to the Capintec Model 192 electrometer providing a bias voltage of +300 V. No absolute dose measurements were measured in the CTDI phantoms; CTDI phantoms were only used for measuring relative SSDPs.

3.5.1 Ion Chamber Calibration

The fundamental relationship of exposure X is given by

$$X = \frac{dQ}{dm} \tag{3.1}$$

where dQ is the absolute value of the total charge of the ions of one sign produced in air when all the electrons liberated by photons in air of mass dm are completed stopped in air. A thimble-type ionization chamber, of which the IC-10 and pencil chambers are classified, could be used to directly measure exposure if they (1) were completely air-equivalent and did not affect the photon fluence, (2) the air cavity volume was accurately known and (3) the wall thickness was sufficiently thick to provide electronic equilibrium. Under these conditions, the exposure is given by

$$X = \frac{Q}{\rho V} \tag{3.2}$$

where Q is the ionization charge generated in the cavity gas of density ρ and volume V. It is difficult however to construct completely air-equivalent walls and to determine the volume of the gas accurately. Therefore for low-energy x-ray beams, thimble ion chambers are usually calibrated against free-air chambers in standards labs (such as the NRC in Canada) where the exposures can be accurately determined for several reference quality beams. In Canada, ion chambers and electrometers are calibrated at the standards lab together to determine an exposure calibration factor N_X for the combination. This con-

stitutes the calibrated dosimetry system for use in the clinic. All other clinical or field chambers are calibrated either directly to this primary system or a dosimetry system directly traceable to the primary. Performing dosimetry in this way is known as reference dosimetry as opposed to absolute dosimetry where dQ and dm can be measured. In this way dose can be reported in an "absolute" or non-relative sense using thimble chambers.

The ion chambers used in this study were calibrated in air on the Pantak x-ray unit at 125 kVp (5 mm Al HVL) using a 20 × 20 cm^2, 50 cm FSD applicator, referenced to the measured exposure X_{ref} using a Capintec PR-06C reference ion chamber (Capintec, Inc., Ramsey, NJ). Even though the 175 kVp setting had an HVL similar to that of the CT beams ($\sim$ 9 mm Al for both), the 125 kVp setting on the Pantak unit was deemed to be more appropriate for calibration of the ion chambers for dose measurements in the actual CT beams due to the similar kVp (125 kVp on Pantak compared to 120 kVp and 130 kVp for the PQ5000 and MX8000 respectively). The reference chamber and its Capintec 192 electrometer (different than the one previously mentioned) together had a N_X value traceable to the NRC Canada (Dec. 2003) with an uncertainty of 0.6% (McCaffrey and Rogers, 2003).

Formally, the exposure calibration factor N_X for each field chamber is given by

$$N_X = \frac{X_{ref}}{M} \tag{3.3}$$

$$= \frac{(M_{raw} \cdot C_{TP} \cdot IS \cdot N_X)_{ref}}{M_{raw} \cdot C_{TP} \cdot IS} \tag{3.4}$$

where M and M_{raw} are the fully-corrected and raw electrometer readings respectively. C_{TP} is a correction factor for temperature (T) and pressure (P) to the reference conditions (T=22 °C, P=760 mm Hg) given as

$$C_{TP} = \left(\frac{273+T}{295}\right)\left(\frac{760}{P}\right) \tag{3.5}$$

with T in Celsius and P in mm Hg. The inverse-square correction factor IS, which moves the effective point of measurement (taken to be the center of the chamber) for each chamber to the surface of the applicator window to which

the detectors were taped, is given by

$$IS = \left(\frac{FSD + \Delta x}{FSD} \right)^2 \tag{3.6}$$

where Δx is the distance between the applicator surface and the center of the detector (typically equal to the detector radius). The subscript "ref" denotes the corresponding quantities for the PR-06C reference ion chamber. The Δx values for the IC-10, PC-4P and PR-06C reference chamber were 5.0 mm, 3.5 mm and 6.2 mm respectively. All chambers were oriented perpendicular to the anode-cathode axis of the x-ray tube with the active centers aligned along the beam central axis. Each raw reading was obtained by delivering 200 monitor units (MU). Using output factors measured in our clinic for this machine, this corresponds to 212 cGy (tissue-kerma) to air at the applicator window. Three irradiation trials were used to obtain the average M_{raw} and $M_{raw,ref}$ before using them in Eq. (3.4) to calculate N_X. The resulting N_X values for the pencil and IC-10 ion chambers are the averages of calibrations performed on five consecutive days with random uncertainties σ_{N_X} determined as the standard deviations.

The field flatness of the Pantak calibration field was assessed by taping a package of Kodak XOmat-V ready-pack film (Eastman Kodak, Rochester, NY) to the applicator surface and delivering 10 MUs. The film was developed using a Kodak X-Omat 270 RA processor (Eastman Kodak, Rochester, NY) then scanned using a Vidar VXR film digitizer (Vidar Systems Corp., Herndon, VA) with a 71 dpi resolution and 8-bit depth. Optical density (OD) values on the film were approximately 1.9 as measured using a X-Rite Model 301 point densitometer (X-Rite Inc., Gradville, MI), within the range of OD values where OD is approximately linear with dose (OD values ranging from about 0 to 2.2 as reported by Zhu et al. (2003) for 100 kVp x-rays). Pixel values in the resulting digitized image varied by less than 4% over the field region corresponding to the location of the 10 cm long pencil chamber during calibration.

3.5.2 Dosimeter Energy Dependence

The energy spectrum of a CT scanner, in theory, is different from the energy spectrum of the Pantak therapy unit. Therefore, the determination of the N_X values discussed in the previous section are not strictly applicable to the CT

beams used in this work. The diagnostic CT beam is in general harder than the superficial therapy unit beam because the very low-energy x-ray photons are removed from the imaging beam to reduce the patient dose and to more closely approximate a monoenergetic beam for image reconstruction. Therefore, a study of relative energy dependence of the N_X value for each chamber is required. This was represented as the corrected chamber reading per unit exposure at each energy $\overline{E}$ and derived as follows.

The tissue-kerma K_{tissue} in air at each energy is related to the corrected chamber reading $M(\overline{E})$ by

$$K_{tissue}(\overline{E}) = M(\overline{E}) \cdot N_X(\overline{E}) \left(\frac{\overline{W}_{air}}{e}\right) \left(\frac{\overline{\mu}_{en}}{\rho}\right)^{tissue}_{air,\overline{E}} S_C \qquad (3.7)$$

where $\overline{E}$ is taken to represent the effective energy for the Pantak beam for each of its kVp-filter combinations. $\overline{W}_{air}$ is the mean energy required to produce an ion pair in dry air and has a value that is practically constant for all photon energies at 33.97 eV per ion pair (Boutillon and Perroche-Roux, 1987). With e the electronic charge, the ratio $(\overline{W}_{air}/e)$ is then the average energy per unit charge of ionization produced. It can be shown that $(\overline{W}_{air}/e)$ is 33.97 J/C (Attix, 1986). By using the definition of exposure (1 R= 2.58×10^{-4} C/kg) and radiation dose (1 Gy = 1 J/kg), $(\overline{W}_{air}/e)$ represents the radiation dose required to produce 1 R of exposure as 8.76 mGy/R. The factor $(\overline{\mu}_{en}/\rho)^{tissue}_{air}$ is the ratio of the average mass-energy absorption coefficients for tissue and air at a given kVp setting and is used to convert air-kerma to tissue-kerma. The factor S_C is the head scatter factor for a given field size at a given FSD defined as

$$S_C(\text{field size}, FSD) = \frac{\text{Exposure per MU (field size, FSD)}}{\text{Exposure per MU } (15 \times 20\,\text{cm}^2, 50\,\text{cm})}. \qquad (3.8)$$

S_C is included to correct for differences in output of the x-ray unit, due to scatter generated along the beam path, from the reference calibration conditions (denominator of Eq. (3.8) for 50 cm FSD applicators) for different applicators. Equation (3.7) can also be used to determine the tissue-kerma $K_{tissue,\,ref}$ using the reference chamber (PR-06C) with known $N_{X,\,ref}$ for each $\overline{E}$. If the same applicator is used for both the reference and field chambers, the relative chamber response ϵ for each kVp setting (hence each $\overline{E}$) is then determined

by equating K_{tissue} and $(K_{tissue})_{ref}$ as follows,

$$[K_{tissue}(\overline{E})]_{ref} = K_{tissue}(\overline{E}) \tag{3.9}$$

$$M_{ref}(\overline{E}) \cdot N_{X,\,ref}(\overline{E}) \left(\frac{\overline{W}_{air}}{e}\right) \left(\frac{\overline{\mu}_{en}}{\rho}\right)^{tissue}_{air,\,\overline{E}} S_C = M(\overline{E}) \cdot N_X(\overline{E}) \left(\frac{\overline{W}_{air}}{e}\right) \left(\frac{\overline{\mu}_{en}}{\rho}\right)^{tissue}_{air,\,\overline{E}} S_C. \tag{3.10}$$

Then

$$\epsilon(\overline{E}) \equiv \frac{1}{N_X(\overline{E})} \tag{3.11}$$

$$= \frac{M(\overline{E})}{M_{ref}(\overline{E}) \cdot N_{X,\,ref}(\overline{E})} \tag{3.12}$$

indicating that ϵ is defined here as the reciprocal of the exposure calibration factor for a given energy.

The relative energy responses of the pencil and IC-10 ion chambers, and the diamond detector were evaluated for each of the Pantak unit's five kVp settings listed in Table III.d, covering an effective energy range of 30 keV to 131 keV. The kVp-filtration values were supplied by the manufacturer while the HVL values were taken from the departmental treatment planning books. Since HVL= $\ln 2/\mu$, the effective energies (Khan, 1994) were determined as the energy of an equivalent monoenergetic beam having the same μ as the actual polyenergetic beam. These values were obtained from Berger et al. (1998).

The experimental setup used to measure $M(\overline{E})$ and $M_{ref}(\overline{E})$ was similar to

Table III.d: Energy and filtration combinations of the Pantak orthovoltage x-ray unit used in determining the energy-dependent responses of the detectors used in this study (excluding TLDs).

kVp	Filtration	First HVL	Effective Energy (keV)
75	2.4 mm Al	2.47 mm Al	29.9
125	3.12 mm Al	5 mm Cu	42.6
175	0.1 mm Cu + 2.5 mm Al	0.47 mm Cu	59.3
200	0.35 mm Cu + 1.5 mm Al	0.9 mm Cu	76.2
300	0.3 mm Sn + 0.5 mm Cu + 1.5 mm Al	2.83 mm Cu	131.3

that described in the previous section except a 15×20 cm^2, 50 cm FSD applicator cone was used. $M(\overline{E})$ and $M_{ref}(\overline{E})$ were the average of three readings, each obtained by delivering 200 MUs. The inverse-square correction factors and C_{TP}, if applicable, were applied to each detector reading to obtain corrected readings. Assuming the uncertainty in C_{TP} to be negligible, the random uncertainty in ϵ was determined as

$$\delta\epsilon = \epsilon \left[\left(\frac{\sigma_M}{M}\right)^2 + \left(\frac{\sigma_{M_{ref}}}{M_{ref}}\right)^2 + \left(\frac{\delta(IS)}{IS}\right)^2 + \left(\frac{\delta(IS_{ref})}{IS_{ref}}\right)^2 \right]^{1/2} \tag{3.13}$$

where σ_M and $\sigma_{M_{ref}}$ are the standard deviations of the raw (uncorrected) electrometer readings for the field and reference (PR-06C) chambers respectively. The inverse-square uncertainty $\delta(IS)$ was given as

$$\delta(IS) = IS \left(\frac{2\delta(\Delta x)}{FSD + \Delta x} \right) \tag{3.14}$$

where the uncertainty $\delta(\Delta x)$ in the chamber standoff distance Δx was 0.2 mm. The uncertainty in the FSD was assumed to be negligible.

3.5.3 $D_L(0)$ Measurements

For all slice widths T studied for each of the two CT systems, $D_L(0)$ was measured in the CIRS phantom for several nominal scan lengths L: 102, 140 and 250 mm, and $14T$. Justification of the scan length choices are given in Tab. III.e. The measured $D_L(0)$ for a scan length of 102 mm should be the same dose as measured with the pencil chamber ($CTDI_{100}$) and a single axial scan. This was taken as the primary verification of the small volume ion chamber method. It should be pointed out for clarity that the scan length

Table III.e: Justification of the choice of scan lengths L used in measuring $D_L(0)$.

L (mm)	Justification
102	Active length of pencil chamber; Integration limits of $CTDI_{100}$
140	Typical length of CTDI phantoms
250	Maximum usable length of CIRS phantom
$14T$	Integration limits of $CTDI_{14T}$ (FDA)

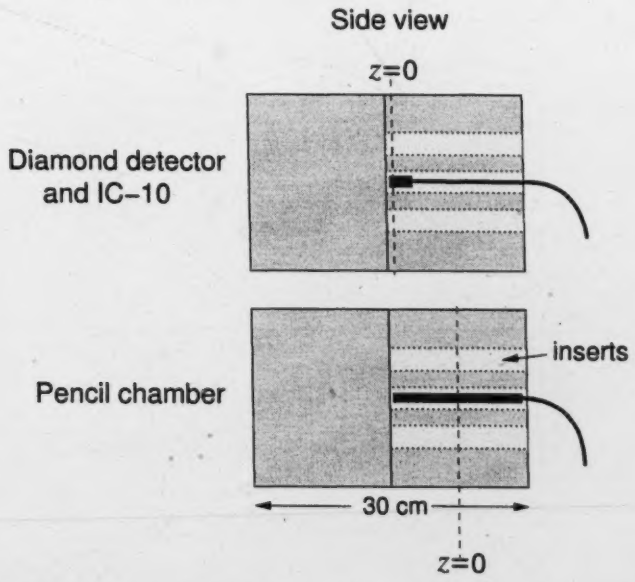

Figure 3.13: Approximate positions of the detectors within the CIRS phantom for measurements along the central axis.

L in measuring $D_L(0)$ corresponds to the distance between the centers of the first and last slices (with the active center of the IC-10 at $z = 0$, see Fig. 3.13) and does not include the extra $T/2$ at each end of the scan series.

Figure 3.13 shows the approximate positions of the detectors within the CIRS phantom. The diamond detector and IC-10 were located just off the mid-point along the phantom length (constrained by the phantom and detector rod designs) which limited the maximum scan length (symmetric about $z = 0$) to ~ 250 mm. In all instances, the actual scan lengths differed from the nominal values due to the following reasons. In helical scanning, extra rotations (1.5) are added by the PQ5000 system to the prescribed scan length since the slices reconstructed at the ends of nominal length require additional rotations for spiral interpolation. In axial scanning, a 4 mm slice spacing ($\sim$ active length of IC-10) was used in order to reduce sampling errors. Further discussion and justification for this choice of scan interval are provided in the next chapter (Sec. 4.4.1). The requirement for a slice at $z = 0$ and a 4 mm spacing resulted in total scan lengths slightly different than the nominal. A helical pitch ($P = \nu\tau/T$) of 1 was used for center-point (Fig. 3.6(b)) doses. For non-central axis points within the cross-section, the longitudinal dose profile resulting from a helical scan of length L, i.e. $D_L(z)$, fluctuates with z (similar to $D_{N,b}(z)$ shown

in Fig. 2.5) for large pitch values (Dixon, 2003). Therefore a pitch of 0.75 was used for off-axis points to reduce these fluctuations. The total mAs for a scan series in both the scanning modes was typically >4000 mAs, with mA settings and rotation times adjusted as necessary (though a 1 s rotation time was the most common). Values of $D_L(0)$, expressed as air-kerma per 100 mAs, can then be calculated as

$$D_L(0) = M \cdot N_X \left(\frac{\overline{W}_{air}}{e}\right) \frac{L}{\nu\tau} \cdot \frac{100}{\text{mAs}} \qquad \text{(helical)} \qquad (3.15)$$

$$= M \cdot N_X \left(\frac{\overline{W}_{air}}{e}\right) \frac{L}{b} \cdot \frac{100}{\text{mAs}} \qquad \text{(axial)} \qquad (3.16)$$

where M is the corrected IC-10 reading, $b = 4$ mm and the N_X value for 125 kVp was used. The average of three trials was taken as the final reading for each parameter set comprised of the CT scanner, slice width, scan length and phantom radial position.

3.5.4 CTDI_{100} Measurements

Pencil chamber readings (CTDI_{100}) were measured in the CIRS phantom by integrating the charge from five 1 s rotations (stationary couch), amounting typically to 1750 mAs per reading. CTDI_{100}, also expressed as air-kerma per 100 mAs, is then calculated as

$$CTDI_{100} = M \cdot N_X \left(\frac{\overline{W}_{air}}{e}\right) \cdot \frac{L}{T} \cdot \frac{100}{\text{mAs}} \qquad (3.17)$$

using the N_X value for 125 kVp. The average of three trials was taken as the final reading for each parameter set comprising the scanner, slice width and phantom radial position. As shown in Fig. 3.13, the pencil chamber could not be placed at the mid-point of the CIRS phantom so it was centered in its 15 cm section. The reduction in the scattering volume is expected to have a negligible effect on CTDI_{100} and the phantom length used is similar to CTDI phantoms.

3.5.5 Uncertainty Assessment for $D_L(0)$ and CTDI_{100}

Random uncertainties in measuring the integral dose using the IC-10 and pencil chambers, σ_{int}, were assessed by measuring the integral dose for the

PQ-10 (nominal $L = 100$ mm) five times on different days and taking the standard deviation of the measured doses. The total random uncertainty in each $D_L(0)$ and CTDI_{100} measurement is then given by

$$\sigma = \sqrt{\sigma_{int}^2 + \sigma_{N_X}^2}. \tag{3.18}$$

These uncertainties are representative of those occurring for all slice widths and scan lengths on both scanners.

Chapter 3 References

Attix, F. H. (1986). *Introduction to Radiological Physics and Radiation Dosimetry*. John Wiley & Sons, New York.

Barnett, E. (2004). Characterization of a diamond detector for intensity modulated point dose measurements. Master's thesis, University of Alberta.

Berger, M. J., Hubbell, J. H., Seltzer, S. M., Coursey, J. S., and Zucker, D. S. (1998). XCOM: Photon Cross Sections Database. http://physics.nist.gov/PhysRefData/Xcom/Text/XCOM.html.

Boutillon, M. and Perroche-Roux, A. M. (1987). Re-evaluation of the W value for electrons in dry air. *Phys. Med. Biol.*, 32(2):213–219.

Chen, X., Schaller, S., and Flohr, T. (2000). Multislice CT-Basics and Applications. In *Somatom Sessions*, volume 6, pages 3–8. Siemens Medical Systems.

Davis, S. D., Ross, C. K., Mobit, P. N., Van der Zwan, L., Chase, W. J., and Shortt, K. R. (2003). The response of LiF thermoluminescence dosemeters to photon beams in the energy range from 30 kV x rays to ^{60}Co gamma rays. *Radiat. Prot. Dosimetry.*, 106(1):33–43.

De Angelis, C., Onori, S., Pacilio, M., Cirrone, G. A. P., Cuttone, G., Raffaele, L., Bucciolini, M., and Mazzocchi, S. (2002). An investigation of the operating characteristics of two PTW diamond detectors in photon and electron beams. *Med. Phys.*, 29:248–254.

Dixon, R. L. (2003). A new look at CT dose measurement: Beyond CTDI. *Med. Phys.*, 30(6):1272–1280.

Findanzio, A., Azario, L., Miceli, R., Russo, A., and Piermattei, A. (2000). PTW-diamond detector: Dose rate and particle type dependence. *Med. Phys.*, 27:2589–2593.

Fowler, J. F. (1966). *Radiation Dosimetry*, volume 2, chapter Solid State Electrical Conductivity in Radiation Dosimetry, pages 291–324. Academic.

Heydarian, M., Hoban, P. W., Beckham, W. A., Borchardt, I. M., and Beddoe, A. H. (1993). Evaluation of a PTW diamond detector for electron beam measurements. *Phys. Med. Biol.*, pages 1035–1042.

Hoban, P. W., Heydarian, M., Beckham, W. A., and Beddoe, A. H. (1994). Dose rate dependence of a PTW diamond detector in the dosimetry of a 6 MV beam. *Phys. Med. Biol.*, 39:1219–1229.

Hugtenburg, R. P., Johnston, K., Chalmers, G. J., and Beddoe, A. H. (2001). Application of diamond detectors fo the dosimetry of 45 and 100 kVp therapy beams: comparison with a parallel-plate ionization chamber and Monte Carlo. *Phys. Med. Biol.*, 46:2489–2501.

Jucius, R. A. and Kambic, G. X. (1977). Radiation dosimetry in computed tomography. *Proc. SPIE*, 127:286–295.

Khan, F. M. (1994). *The Physics of Radiation Therapy*. Williams and Wilkins, Baltimore, MD, 2nd edition.

Mainwood, A. (2000). Recent developments of diamond detectors for particles and UV radiation. *Semicond. Sci. Technol.*, 15:R55–R63.

Martens, C., De Wagter, C., and De Neve, W. (2000). The value of the PinPoint ion chamber for characterization of small field segments used in intensity-modulated radiotherapy. *Phys. Med. Biol.*, 45:2519–2530.

McCaffrey, J. P. and Rogers, D. W. O. (2003). Calibration of a Capintec model 192 electrometer serial number 544761324, with a PTW model N30004 ionization chamber serial number 0010. Technical Report IRS-2003-0883, National Research Council (NRC) Canada.

Mobit, P. N. and Sandison, G. A. (1999). A Monte Carlo comparison of the response of the PTW-diamond and TL-diamond detectors in megavoltage photon beams. *Med. Phys.*, 26(11):2503–2507.

Planskoy, B. (1980). Evaluation of diamond radiation dosemeters. *Phys. Med. Biol.*, 25(3):519–32.

Ramo, S. (1939). *Proc. IRE*, 27:584.

Rustgi, S. N. (1995). Evaluation of the dosimetric characteristics of a diamond detector for photon beam measurements. *Med. Phys.*, 22(5):567–70. 0094-2405 Journal Article.

Seuntjens, J., Aalbers, A., Grimbergen, T., Mijnheer, B., Thierens, H., Van Dam, J., Wittkamper, F., Zoetlief, J., Piessens, M., and Piret, P. (1999). Suitability of diamond detectors to measure central axis depth kerma curves for low- and medium-energy x-rays. In *Kilovoltage X-Ray Dosimetry*, pages 227–238. Medical Physics Publishing, Madison.

Suzuki, A. and Suzuki, M. N. (1978). Use of a pencil-shaped ionization chamber for measurement of exposure resulting from a computed tomography scan. *Med. Phys.*, 5(6):536–9.

Tapper, R. J. (2000). Diamond detectors in particle physics. *Rep. Prog. Phys.*, 63:1273–1316.

Yin, Z., Hugtenburg, R. P., Green, S., and Beddoe, A. H. (2004). Dose responses of diamond detectors to monoenergetic x-rays. *Nucl. Instr. and Meth. in Phys. Res. B.*, 213:646–649.

Zhu, X. R., Yoo, S., Jursinic, P. A., Grimm, D. F., Lopez, F., Rownd, J. J., and Gillin, M. T. (2003). Characteristics of sensitometric curves of radiographic films. *Med. Phys.*, 30(5):912–919.

Chapter 4

Results and Discussion

This chapter presents the experimental results of the measurements obtained following the methods described in Chapter 3. Since several detectors (each with its own energy response characteristics) were used to measure dose and the results from each are often compared, the measured energy dependent response of the IC-10, pencil chamber and diamond detector are shown and discussed. Single scan dose profiles (SSDPs) measured using the PTW diamond detector in the long plastic-water phantom are then shown and numerically integrated to compare the integral dose for various scan lengths. A functional form for the SSDP is also presented and example fits are illustrated for selected profiles. One profile off the phantom central axis is also shown. A single central axis SSDP is then used as an example to highlight several observations, including an asymmetry in the profiles resulting from the measurement method, verification of the profile shape using TLDs and an IC-10 ion chamber, and the effect of the phantom length on the measured profile. The effects of the phantom composition and length on the measured SSDP are illustrated in SSDPs measured in 15 cm long PMMA CTDI phantoms. Predictions of the relative change in $D_L(0)$ with scan length, based on convolutions of the SSDPs with rectangular functions representing the scan length, are then made. Potential sources of errors introduced in measuring $D_L(0)$ with a small volume chamber for axial and helical scan modes are then discussed and quantitatively estimated using a diamond-measured SSDP. Finally, values of $D_L(0)$ measured using the IC-10 ion chamber at the center of the plastic-water phantom for short and long scan lengths are tabulated and compared to pencil ion chamber ($CTDI_{100}$) doses.

4.1 Detector Energy Response

The relative energy response curves of the two ion chambers and the diamond detector are shown in Fig. 4.1, normalized to the 175 kVp setting on the Pantak orthovoltage x-ray therapy unit. This setting corresponds to an effective energy of 59.3 keV which is approximately the effective energy of the CT beams. Effective energy (E_{eff}) is defined here as the energy of a monoenergetic photon beam having the same penetrating power as the actual polychromatic CT beam and thus is attenuated at the same rate (i.e., same μ) (Khan, 1994) in aluminum. For the PQ5000 for example,

$$\mu_{Al} = \frac{\ln 2}{\text{HVL}} = \frac{\ln 2}{8.5\text{ mm}} = 0.08155\text{ mm}^{-1} \tag{4.1}$$

which corresponds to $E_{eff} = 56.6$ keV using the attenuation data of Berger et al. (1998). The effective energy of the MX8000 is 59.8 keV for the 120 kVp setting used in the experiment. The five data points in the energy response graphs correspond to the five kVp settings on the Pantak unit. The HVL for aluminum measured for each setting has been converted to effective energy

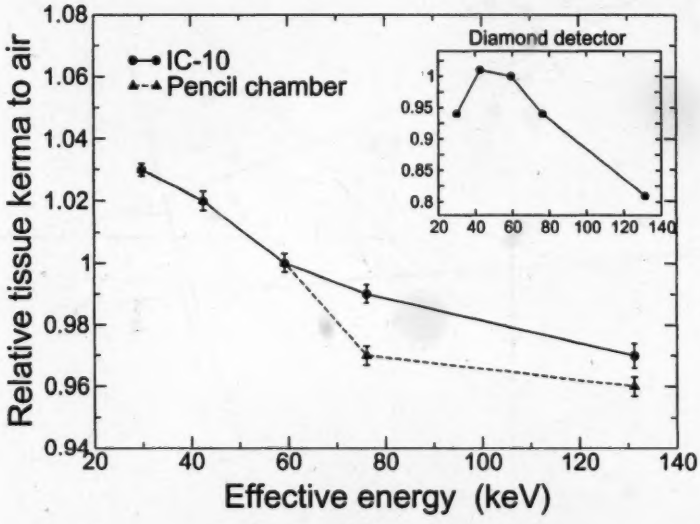

Figure 4.1: Relative energy response curves for the Wellhöfer IC-10 and Capintec PC-4P ionization chambers, and the PTW diamond detector (inset), normalized to an effective energy of 59 keV (approximate effective energy of the CT beams).

using Eq. (4.1) and the attenuation data for aluminum from Berger et al. (1998). The IC-10 and pencil chambers respond approximately the same at energies relevant to CT since both are composed primarily of air-equivalent plastic (Shonka C552). For energies < 59 keV characterizing the energy of scattered photons, the two curves are indistinguishable. However, for $E_{eff} > 59$ keV, the pencil chamber has a $1-2\%$ lower response compared to the IC-10. The response of the diamond detector is also shown in the inset of Fig. 4.1, illustrating the difficulty in its use for absolute dose measurements due to the variability in response (up to 20%) over the spectral range of primary photons in imaging beams. It is for this reason that the diamond detector was only used to measure the relative shape of the SSDPs. It should be noted that the effective energy of the beam at the center of the phantom does not vary significantly (Tsai et al., 2003), therefore the relative shape of the SSDPs should not be greatly affected. In reality, since the scattered photons do have a slightly lower energy, the diamond-measured SSDP scatter tails are lower than the true values due to its under-response at lower energies. The energy response curves for the PC-4P ion chamber and PTW diamond detector are qualitatively similar to those found by Jucius and Kambic (1977) and Yin et al. (2004); Seuntjens et al. (1999) respectively. For the PC-4P, the response curve of Jucius and Kambic (1977) peaks at $E_{eff} \approx 35$ keV, similar to our results, and drops steadily to a relative response of 0.75 at 14 keV. The relative air-kerma (response) curve of the diamond detector in Tsai et al. (2003) peaks at a mean x-ray energy of about 100 keV while the curve of Seuntjens et al. (1999) peaks at 80 keV. These results are quite different to the peak response at 43 keV determined here. This is most likely due to their use of a photon fluence spectral mean energy,

$$\overline{E} = \frac{\int \Phi(h\nu)(h\nu)d(h\nu)}{\int \Phi(h\nu)d(h\nu)}, \tag{4.2}$$

where $\Phi(h\nu)$ is the fluence of photons with energy $h\nu$, compared to effective energy used here, Eq. (4.1).

4.2 SSDPs

The relative SSDPs along the central axis of the CIRS phantom are shown in Figs. 4.2(a) and 4.2(b) for the PQ5000 and MX8000 CT scanners respectively.

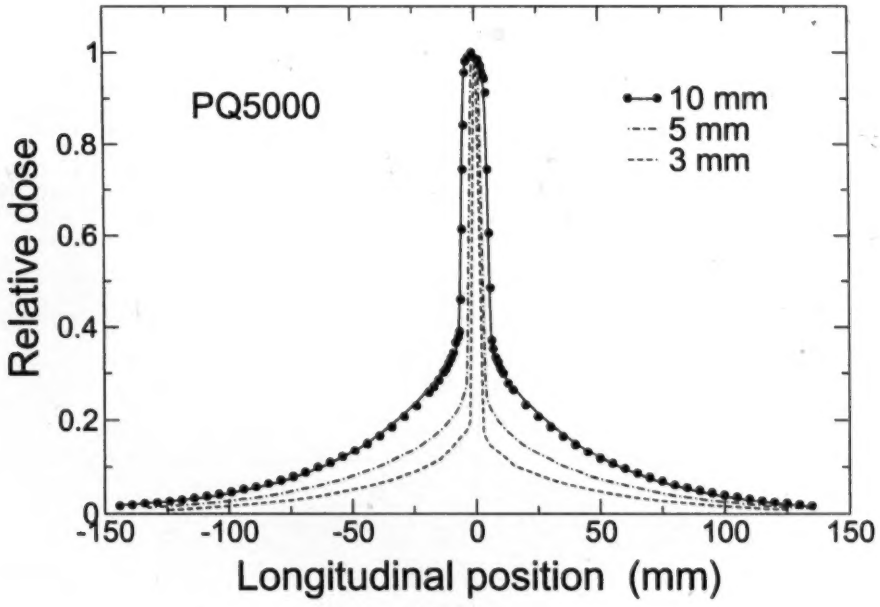

(a) PQ5000

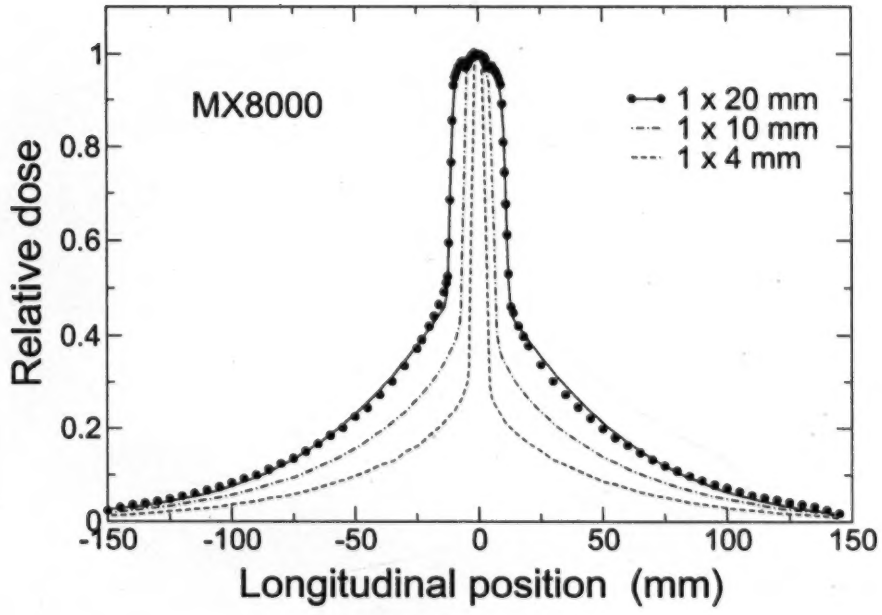

(b) MX8000

Figure 4.2: Relative SSDPs along the central axis of the CIRS phantom for the PQ5000 single-slice CT scanner for 3, 5 and 10 mm nominal slice widths (a) and for the MX8000 Quad multi-slice CT scanner for 1×4, 1×10 and 1×20 mm slice settings (b), measured using a PTW diamond detector. The curves through the 10 mm (a) and 1×20 mm (b) profiles are analytic fits (see Eq. (4.6)).

The data points, with random uncertainties $< 0.6\%$, are not shown for clarity on all profiles except for the PQ-10 and MX8000, 1×20 mm slice width where the (solid) curves are analytic fits to the data using the sum of two modified Gaussian functions (see Sec. 4.2.1). All other curves shown are simply lines connecting the data points since the sampling intervals were small and the deviations from analytic curves were negligible. The most important feature of all SSDPs is the non-negligible dose in the scatter tails at positions well beyond $z = \pm 50$ mm and $z = \pm 7T$, corresponding to the integration limits of CTDI_{100} and CTDI_{14T} respectively.

The extended scatter tails evident in the measured SSDPs can be understood by looking at the breakdown of x-ray photon interactions in water. Assuming 59 keV incident photons, the dominant interaction mechanism is Compton scattering with the interaction cross section σ representing 85% of the total interaction cross section μ. The other interactions are Rayleigh (coherent) scattering and the photoelectric effect with their respective cross sections comprising 6.9% and 7.6% of the total. Cross section data has been taken from Berger et al. (1998). Rayleigh scattered photons are primarily forward scattered (Johns and Cunningham, 1983) and therefore contribute little to the measured scatter tails of the SSDP. Using the continuous slowing down approximation (CSDA) range for electrons (Johns and Cunningham, 1983) in water and a 59 keV upper limit on the initial photoelectron energy, the emitted photoelectrons will deposit their energy within less than 0.06 mm (Berger et al., 2000). Therefore photoelectrons created in the primary CT beam do not contribute to the measured scatter tails of the SSDP. However if we look at the Compton scattering relations (Khan, 1994), the minimum energy of a Compton scattered photon $h\nu'_{min}$ with incident energy $h\nu = 0.059$ MeV is given by

$$h\nu'_{min} = h\nu \frac{1}{1+2\alpha} \tag{4.3}$$

where $\alpha = h\nu/m_o c^2$ and $m_o c^2$ is the rest mass energy of an electron (0.511 MeV). Therefore $h\nu'_{min} = 48$ keV. The maximum energy of the ejected electron is

$$E_{max} = h\nu \frac{2\alpha}{1+2\alpha} \tag{4.4}$$

which for a 59 keV incident photon corresponds to $E_{max} = 11$ keV. For a second scattering process, $h\nu'_{min} = 40$ keV and $E_{max} = 7$ keV. Therefore most of the energy is transferred to the scattered photons which can travel

significantly farther than the scattered electrons before interacting. For $h\nu <$ 100 keV, the differential cross section for Compton scattering $d\sigma/d\Omega$ is nearly the same for all scattered photon angles ϕ, passing through a shallow minimum at $\phi = 90°$(Johns and Cunningham, 1983). Therefore the angular distribution of Compton scattered photons in the CT primary beam is almost isotropic allowing for measurable dose at 12.5 cm from the scan center as observed in this work. Roughly 6% of the photons scattered from the primary beam will reach this distance in water.

To determine the integral dose from the profiles, SSDPs were first interpolated using an Akima spline (Akima, 1970) for higher and evenly-spaced sampling, then integrated using the trapezoidal rule (Burden and Faires, 1997). Dividing $f(z)$ into n strips ($n+1$ samples) of width $h = L/n$, we have

$$\int_{-L/2}^{+L/2} f(z)dz \approx \frac{h}{2}\sum_{i=1}^{n} f(-L/2+(i-1)h) + f(-L/2+ih) \tag{4.5}$$

with h typically 0.1 mm (from the interpolation). For *all* central axis SSDPs measured in the CIRS phantom, the integral dose over 250 mm was $\sim$ 30% higher than over 100 mm (i.e., CTDI_{100}) for the PQ5000 and $\sim$ 32% higher for the MX8000. It is interesting to note that for a given scanner, the relative difference in integral dose over 250 mm and 100 mm is always approximately the same independent of the slice width. The integral dose over 250 mm was approximately 2.2 times higher (113%) than over $14T$ for the PQ5000, 3 mm slice width, since $14T$ only corresponds to 42 mm.

4.2.1 Analytic Profile Fitting

On occasions where the sampling intervals are larger than what is needed to adequately represent the profile, e.g., due to time or x-ray tube workload constraints, an analytic fit to the data may be useful to interpolate the SSDP data. SSDPs have previously been modelled as the sum of two Gaussians (Shope et al., 1981), a combination of a Gaussian and a Lorentzian (Tsai et al., 2003), and a product of exponentials (Oliveira et al., 1995). In all these cases, SSDPs were measured using TLDs in standard CTDI phantoms of 15 cm length. In Shope et al. (1981), the SSDPs are in general poorly sampled, especially around the peak. The profiles of Tsai et al. (2003) were sampled at a much smaller interval over the profile as a whole but the sampling in the peak

Table IV.a: Parameter values of the central axis SSDP fits using Eq. (4.6) for the PQ5000, 10 mm slice width (PQ-10) and the MX8000, 1 × 20 mm slice selection (MX-20).

SSDP	a_0	a_1	a_2	a_3	a_4	a_5	a_6	a_7	a_8
PQ-10	0.589	-0.0232	5.14	7.93	0.423	-1.35	19.2	1	-1.97E-5
MX-20	0.460	-0.217	10.9	12.3	0.551	-1.56	30.0	1.2	-3.53E-5

region was still limited by the 0.9 mm TLD chip thickness. The fits of Oliveira et al. (1995) were poor in general. We found the sum of two modified Gaussians and an asymmetry term work best for modelling the SSDPs measured with the diamond detector in the plastic water phantom,

$$f(z) = a_0 \exp\left[-\frac{1}{2}\left(\frac{|z-a_1|}{a_2}\right)^{a_3}\right] + a_4 \exp\left[-\frac{1}{2}\left(\frac{|z-a_5|}{a_6}\right)^{a_7}\right] + a_8 z. \quad (4.6)$$

The parameters of the first term on the right of Eq. (4.6) were constrained to primarily model the flat-topped peak of the SSDP while the exponent of the second term (a_7) was kept near a value of 1 (i.e., a pointed peak) in order to model the scatter tails. The solid curves in Fig. 4.2 show analytic fits to the central axis SSDP data sets for the PQ-10 and MX8000, 1 × 20 mm width, with correlation coefficients (R^2) of 0.9997 and 0.9999 respectively. The fitting parameters for the two curves shown are given in Tab. IV.a. The goodness of these two fits is representative of all slice widths and scanners studied. The necessity of a functional form for $f(z)$ different than previously reported is most likely a result of the fundamental difference in the shape of the SSDP due to the different scattering properties of water-equivalent and PMMA phantoms as discussed in Section 4.2.6. The longer phantom length is also a contributing factor.

4.2.2 Profile Asymmetry

A slight asymmetry is evident in the SSDPs of Fig. 4.2. Figure 4.3(a) highlights the extent of the asymmetry where the PQ-10 SSDP values for $z < 0$ have been geometrically transformed ("mirrored") about $z = 0$ and compared to the measured SSDP for $z > 0$. This decrease in the SSDP values for $z > 0$ is due to the reduction in scattered photons reaching the sensitive volume of the diamond detector caused by self-shielding (angular sensitivity), and because

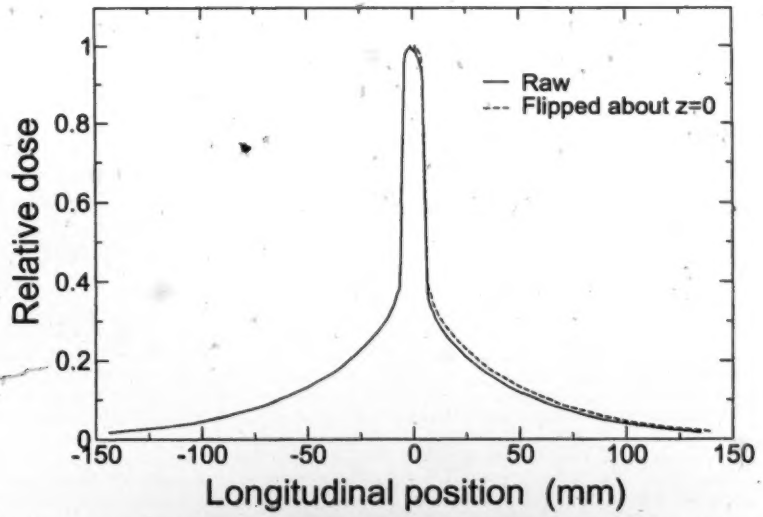

(a) SSDP highlighting the extent of the asymmetry due to self-shielding of the diamond detector and air gaps in the phantom (see Fig. 4.3(b)).

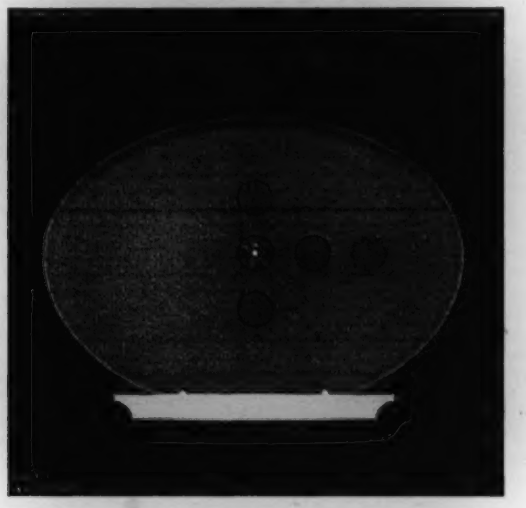

(b) CT image showing the air gaps surrounding the rods and cable in the CIRS phantom leading to a reduction in the SSDP values for $z > 0$.

Figure 4.3: Extent and causes of the slight asymmetry when measuring SSDPs with the diamond detector in the CIRS phantom. The PQ-10 SSDP is used here as an example.

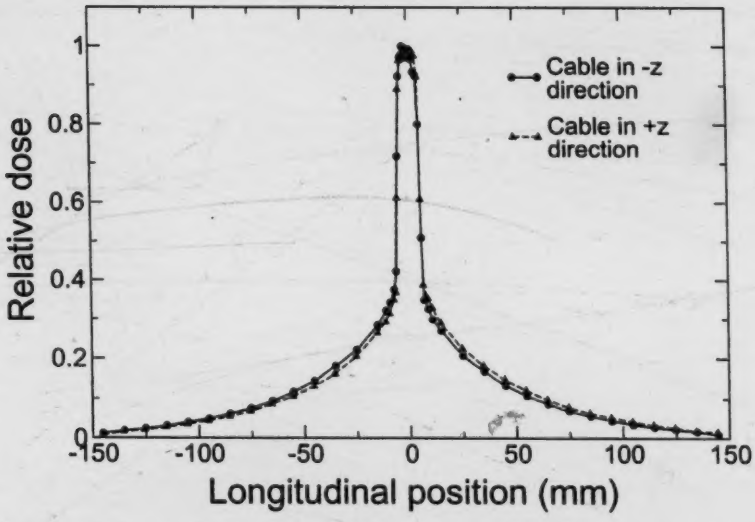

(c) Comparison of the original SSDP (with cable in $-z$ direction) and the SSDP with the phantom rotated by 180° (cable in $+z$ direction).

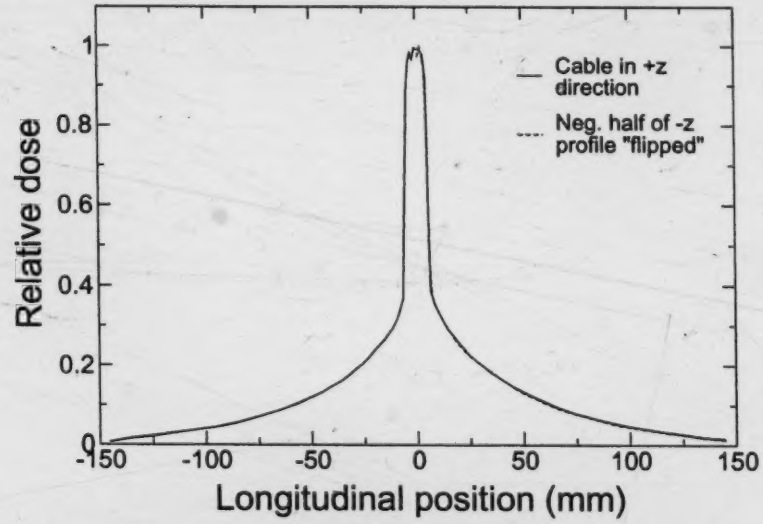

(d) Comparison of the original SSDP (with cable in $-z$ direction) and the negative half of the SSDP measured with the phantom rotated by 180° (cable in $+z$ direction) flipped about $z = 0$.

Figure 4.3: Extent and causes of the slight asymmetry when measuring SSDPs with the diamond detector in the CIRS phantom. The PQ-10 SSDP is used here as an example.

of air gaps surrounding the cable and rods as shown in Fig. 4.3(b). The net effect is a $3-4\%$ reduction in the integral dose for $z = \pm 100$ mm ($L = 200$ mm) compared to integrating the symmetrized SSDP over the same interval. Measurement of the SSDP with the phantom rotated by 180° (end-to-end) resulted in a nearly identical "mirror image" of the original SSDP as shown in Fig. 4.3(c). When the negative portion of the SSDP obtained in the rotated phantom is flipped about $z = 0$, it almost perfectly matches the original SSDP for $z > 0$ as shown in Fig. 4.3(d). This confirms that the phantom and detector are the major sources of the slight asymmetry and also shows that the *beam* profile (before entering the phantom) is symmetric. Therefore, only a half-profile is really required. The "missing" half-profile can be mathematically reconstructed, thereby circumventing any profile asymmetries due the phantom and detectors. One additional conclusion is that for this scanner where the anode-cathode axis of the x-ray tube is parallel to the rotational (z) axis, the heel effect (the reduction in photon fluence on the anode side due to self-attenuation) is minimal.

4.2.3 Off-Axis

As an example of a SSDP off the central axis of the CIRS phantom, Fig. 4.4 shows the SSDP for position 2 (see Fig. 3.6(b)) at 7 cm depth for the PQ-10, compared to the central axis SSDP. In Fig. 4.4(a), the SSDPs are shown as electrometer readings per 100 mAs to show the difference in the relative peak heights with the off axis peak height being larger due to less attenuation of the primary beam at the shallow depth. When normalized to the peak electrometer reading, the profile at the peripheral location (full-width at tenth-maximum, FWTM = 83.4 mm) shown in Fig. 4.4(b) is narrower than at the phantom center (FWTM = 128.2 mm) due to less scatter at the shallower depth. Numerically integrating the off-axis profile over 250 mm using Eq. (4.5) resulted in a dose 22% higher than over 100 mm. The results were similar for the 3 mm and 5 mm slice widths on the PQ5000 at off-axis position 2. The SSDPs for position 1 were not measured since they are not expected to be noticeably different and therefore should not provide any additional insights.

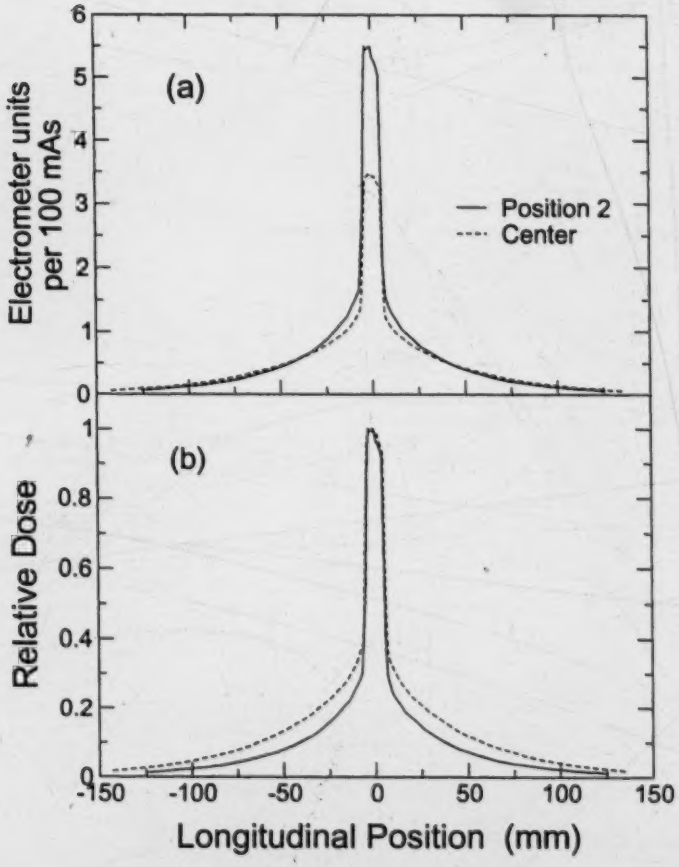

Figure 4.4: Comparison of the SSDPs along the central axis and off-axis position 2 (see Fig. 3.6(b)) of the CIRS phantom for the PQ5000 scanner, 10 mm slice width. (a) Readings are electrometer units ($\propto$ charge) per 100 mAs (b) Relative to the peak doses.

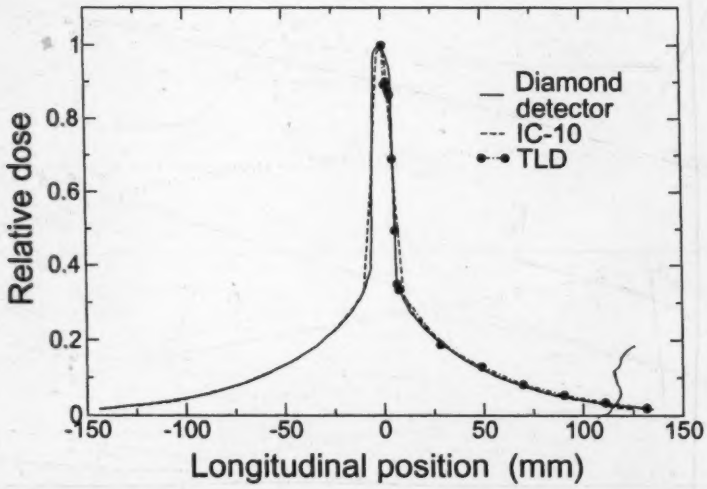

Figure 4.5: Comparison of the central axis SSDP in the CIRS phantom measured using the PTW diamond detector, IC-10 ion chamber and LiF TLDs (TLD-100) for the PQ5000, 10 mm slice width.

4.2.4 Detector Comparison

The relative SSDP for the PQ-10 as measured by the diamond detector, IC-10 ion chamber and TLDs is shown in Fig. 4.5. Apart from the averaging due to the 3.3 mm active length of the IC-10 near the peak, the SSDPs measured using all three detectors are in very good agreement. This is true even for $z > 0$ meaning that the SSDP asymmetry due to phantom and detector affects is similar for all detectors. Therefore the dominant source of the asymmetry effect is most likely the air spaces around the phantom rods. Although the three detectors may exhibit different responses for the energy spectrum in CT, the profiles measured by each detector have been normalized to the peak value. In addition, the change in spectrum along the z-axis at the center of the phantom is not large, as indicated by Tsai et al. (2003) who showed that the spread of effective photon energies is less than ± 5 keV. Since the response curves of Fig. 4.1 do not change very much near 60 keV, the profiles measured by IC-10 and diamond detector are similar. This implies that energy response corrections would depend on depth in phantom and changes from calibration conditions, and it will be nearly independent of the z-position, if the goal was to obtain absolute (non-relative) SSDPs using the diamond detector.

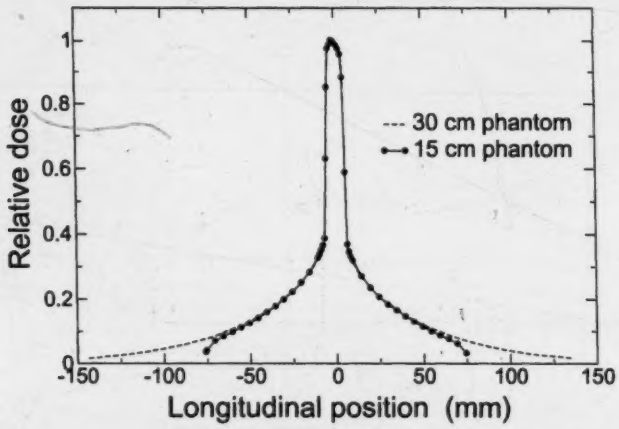

Figure 4.6: Comparison of the central axis SSDP measured in one half (15 cm) and full (30 cm) CIRS phantom for the PQ5000 scanner, 10 mm slice width.

4.2.5 Effect of Phantom Length

Since SSDPs are usually measured in 15 cm long phantoms, the SSDP for the PQ-10 case was measured with the diamond detector in only a 15 cm section of the CIRS phantom. This was achieved by repositioning the detector insert in the middle of the 15 cm long phantom and filling the resulting air space with another homogeneous water-equivalent CIRS rod. The resulting SSDP is shown in Fig. 4.6 compared to the SSDP measured in the full 30 cm phantom. In the central region, the two profiles are indistinguishable. As expected, the scatter tails of the 15 cm SSDP fall to zero faster than in the 30 cm phantom due to the reduction of inward sidescatter near the edges of the phantom. Therefore, extrapolating the SSDPs measured in a 15 cm long phantom to zero (as is commonly done) leads to an underestimation of the true profile width (by about 30% for the PQ-10).

4.2.6 CTDI Phantoms

Figure 4.7 shows the SSDPs measured along the central axis in the CTDI body (Fig. 4.7a) and head (Fig. 4.7b) phantoms for slice widths of 5 mm and 3 mm respectively. The profiles are similar to those in the literature (McNitt et al. (1999) for example) but are now scaled to the peak dose to highlight the non-negligible relative dose outside the limits of $CTDI_{100}$, namely 13% relative dose at $z = \pm 50$ mm and 9% near $z = \pm 75$ mm for the body phantom. This

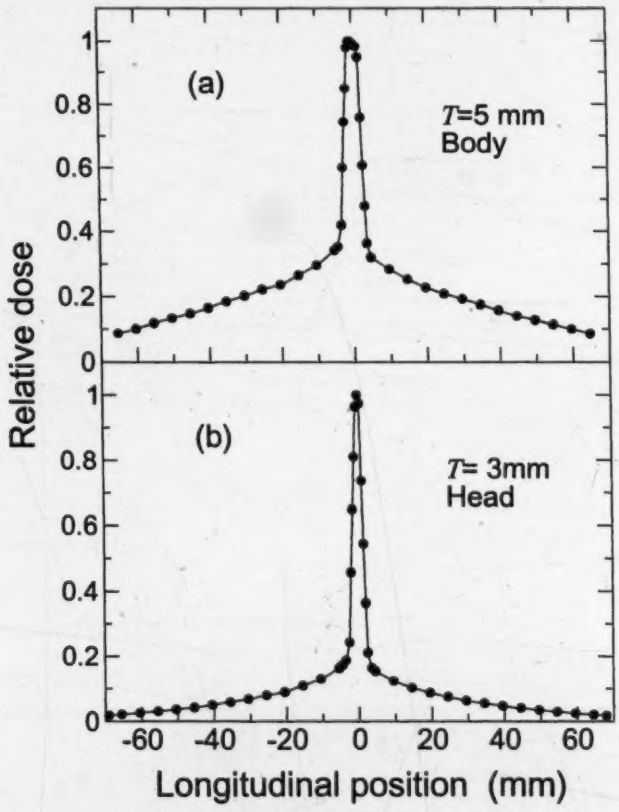

Figure 4.7: SSDPs in the body (a) and head (b) CTDI phantoms for nominal slice widths of 5 and 3 mm respectively, PQ5000 CT scanner.

translates to an integral dose about 16% higher over 140 mm than 100 mm. Therefore even in conventional body CT phantoms, $CTDI_{100}$ underestimates the cumulative dose for $L > 10$ cm. For the 3 mm slice width SSDP in the head phantom, the phantom length is probably adequate for measuring the SSDP. However, it is seen that the relative dose at $z = \pm 50$ mm is about 3% meaning that $CTDI_{100}$ still underestimates the equilibrium dose. Looking at the basic shape of the SSDPs, the scatter tails measured in the PMMA phantoms fall off much more linearly than the roughly slow exponential drop in dose seen for SSDPs measured in the plastic water phantom (Fig. 4.2), illustrating that PMMA phantoms ($Z = 6.56$, $\rho = 1.19$ g/cm^3) do not accurately represent the scatter conditions in a real patient ($Z = 7.4$ for soft tissue, $\rho = 1.00$ g/cm^3).

4.3 Cumulative Dose Profiles

Cumulative dose profiles $D_L(z)$ can be generated by convolving the central axis SSDP measured in the plastic water phantom with rectangular functions for several widths L (100 – 400 mm). Examples of $D_L(z)$ for helical scan series of several total lengths L are shown in Fig. 4.8 for the PQ-10. Equation (2.25) was used for these calculations except the integration limits were $(z \pm L/2)$. The SSDP had been symmetrized prior to the convolution (using the SSDP values for $z \leq 0$) and extrapolated to zero using an Akima spline to approximate the "true" profile (no detector or rods in the phantom). The curves are normalized to the equilibrium dose at the center of the scan series $D_{eq}(0)$, which is equivalent to the integral over an interval greater than or equal to the width of the extrapolated SSDP. For the PQ-10, dose equilibrium was reached for $L > 370$ mm (i.e., $D_{eq}(0) = D_{400}(0)$ in Fig. 4.8). The actual cumulative dose profile for an axial scan series would exhibit periodic maxima and minima with magnitudes dependent on the spacing between scans (similar to Fig. 2.5). Therefore, for axial scanning, the curves in Fig. 4.8 represent the running mean of the actual cumulative dose profile over a period b (Sec. 2.3.8.2). Note that these are cumulative dose curves for the actual scan length, i.e, the actual

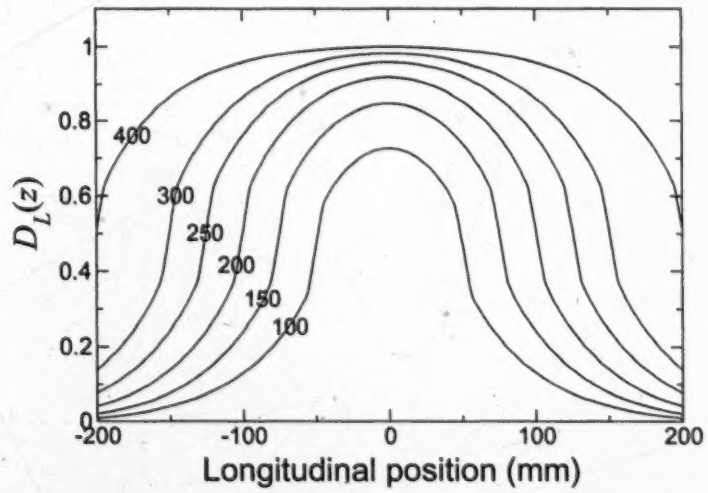

Figure 4.8: Cumulative dose $D_L(z)$ along the central axis of the CIRS phantom, normalized to the equilibrium dose at the center of the scan series $D_{eq}(0)$, generated using convolutions of the symmetrized SSDP for various scan lengths (in mm) for the PQ5000 scanner, 10 mm slice width.

irradiated volume. In practice, the helical dose would be slightly larger than an axial scan for the same *imaged* length and $b = \nu\tau$ (Boone et al., 2000) due to the extra rotations needed for spiral interpolation (1.5 for the PQ5000).

Figure 4.9 shows the predicted ratio of the maximum to the equilibrium dose at the center of the scan series $D_L(0)/D_{eq}(0)$ as a function of scan length for all central axis SSDPs studied in the CIRS phantom. It should be re-stated that these curves are solely derived from integrating the SSDPs and do not correspond to integrated dose measured using the small volume chamber. It can be seen that CTDI_{100} (corresponding to $L = 100$ mm) underestimates the equilibrium dose by 25−30% depending on the slice width for the PQ5000, and up to 30% for the MX8000. Also evident is that CTDI_{14T} could underestimate the equilibrium dose by up to 50% for small slice widths. There appears to be a reduced slice width dependence of $D_L(0)/D_{eq}(0)$ for the MX8000 compared to the PQ5000. No concrete explanation can be given at this time. However, this could be an artifact of the SSDP extrapolation used in calculating $D_L(0)$ for $L > 250$ mm.

4.4 Measuring $D_L(0)$ using a Small Volume Ion Chamber

The general approach taken is that measuring $D_L(0)$ with a small volume chamber is equivalent to estimating $\int_{-L/2}^{+L/2} f(z)dz$ by first averaging $f(z)$ over the active length of the finite-sized detector, and then sampling and integrating $f(z)$ as one performs an axial or helical scan series. For axial scanning, the source rotates at discrete couch positions introducing both sampling and detector averaging errors while integrating the SSDP. For helical scanning, the couch moves continuously while the source rotates and thus the measured integral dose suffers only from detector averaging for points along the central axis of a cylindrical phantom. For points off the central axis or for an elliptical phantom, the relative positions of the detector and source may introduce additional errors for helical scanning due to the change in path length from the source to the detector. The effects of the phantom ellipticity on measuring $D_L(0)$ along the central axis are discussed in Sec. 4.4.2.

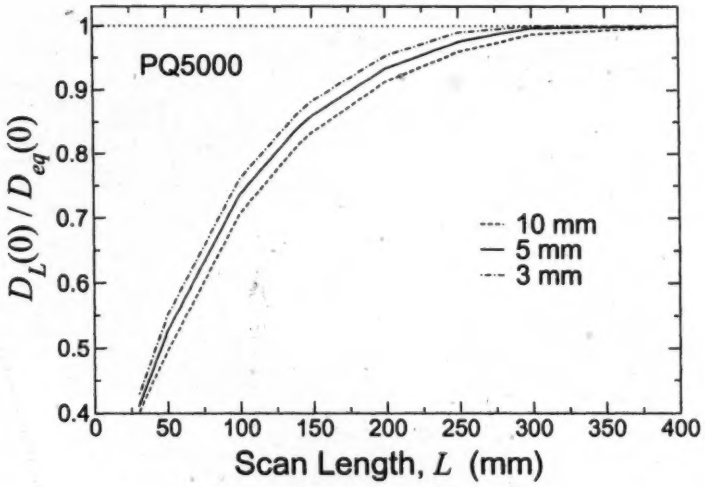

(a) PQ5000

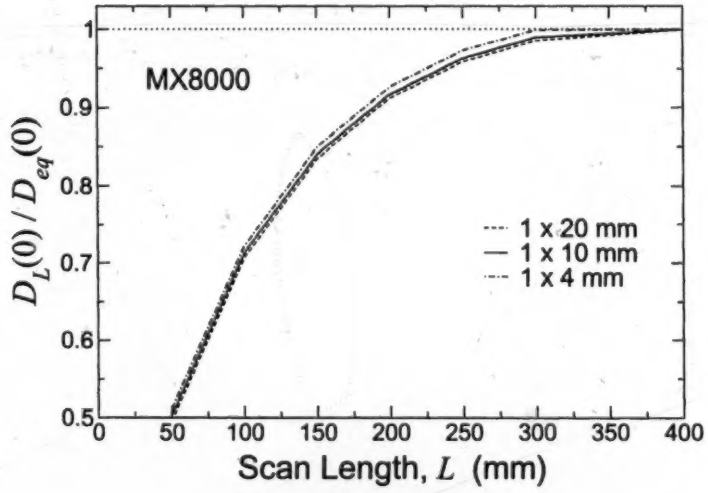

(b) MX8000

Figure 4.9: Predicted ratios of the maximum to equilibrium central axis dose in the CIRS phantom at the center of the scan series of various lengths, for the PQ5000 (a) and MX8000 (b) scanners. The legends state the nominal slice widths (a) and the slice settings in single slice mode (b).

4.4.1 Axial Mode Considerations

Since an axial scan series is a "step and shoot" procedure, significant sampling errors (aliasing) in $D_L(0)$ due to the high dose gradient region near the peak of the SSDP may be introduced if b is much larger than the active length of the detector. An alternate viewpoint is that if the scan interval is too large, the representation of $D_L(z)$ as a running mean dose for an axial scan series becomes less meaningful since the variation of the actual cumulative dose profile about the mean becomes so large. The final choice of scan interval for measurement is then a compromise between tolerance for sampling errors and acceptable total x-ray tube workload in an axial scan series, keeping in mind that $D_L(0)$ scales with b according to Eq. (2.30). These sampling and detector averaging effects are illustrated in Fig. 4.10 where a moving-average filter (equal to the active length of IC-10) has been applied to the PQ-10 SSDP measured with the diamond detector (simulated helical curve), and the resulting curve sampled at 4 mm intervals (simulated axial curve). Here the reasonable assumption has been made that the diamond detector best represents the "true" SSDP. Only the peak region of the SSDP and simulated curves is shown since any errors would only be significant where the dose gradient is large. For the interval $z = \pm 10$ mm, the difference in the (numeric) integral doses for the diamond SSDP and detector-averaged curve is $< 0.1\%$ implying that at the center of

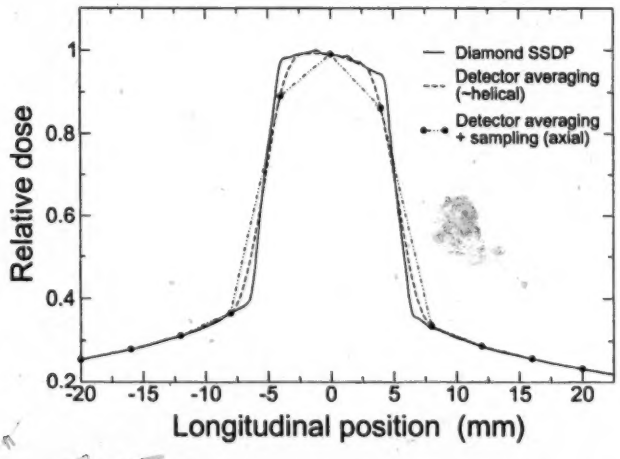

Figure 4.10: Simulated effects of detector (volume) averaging (helical and axial mode) and a 4 mm sampling interval (axial mode) on measuring the PQ-10 SSDP with the IC-10 ion chamber.

the phantom and a helical scan series, detector averaging changes $D_L(0)$ only negligibly. By comparing the sampled-averaged curves, i.e., simulating axial scanning, to the averaged-only curves for all measured SSDPs at the center of the phantom, it was found that measuring $D_L(0)$ for axial scans with $b = 4$ mm using the IC-10 would introduce $< 1\%$ error compared to contiguous helical scanning (pitch=1) for the same scan length (ignoring effects of the phantom shape on helical scanning, see next Section). If a 10 mm interval was used for axial scanning (contiguous slices for the PQ-10), this error would inflate to as much as 4%.

4.4.2 Helical Mode Considerations

Assuming ideal alignment of the phantom and scanner rotational axes, and that the CT beam output does not change substantially with the source angle, any errors introduced in measuring $D_L(0)$ at the center of a *cylindrical* phantom using a helical scan series result from detector averaging alone. For a helical scan in an elliptical phantom however, the signal measured depends on the relative positions of the detector (phantom) and x-ray source, resulting in a variation in $D_L(0)$ depending on the starting angle of the source. For example, if the angular position of the x-ray source is on the minor axis of the phantom when the detector is at $z = 0$, the primary radiation detected will be larger than if the source is on the major axis. To investigate this variability, consider an elliptical phantom with semi-major axis a and semi-minor axis c translating through a CT gantry as illustrated in Fig. 4.11. With the eccentricity of an ellipse defined as

$$e \equiv \sqrt{1 - \frac{c^2}{a^2}} \tag{4.7}$$

and $0 \leq e < 1$, the distance r from the center of the phantom to the surface in terms of the eccentric angle θ is given in polar coordinates (Weisstein, 2004) by

$$r = a\sqrt{\frac{1 - e^2}{1 - e^2 \cos^2 \theta}}. \tag{4.8}$$

The source angle and eccentricity angle are seen from Fig. 4.11 to be equivalent. The dose deposited at the center of the phantom is proportional to the intensity $I(r)$ of photons reaching the center. From the exponential attenuation law and

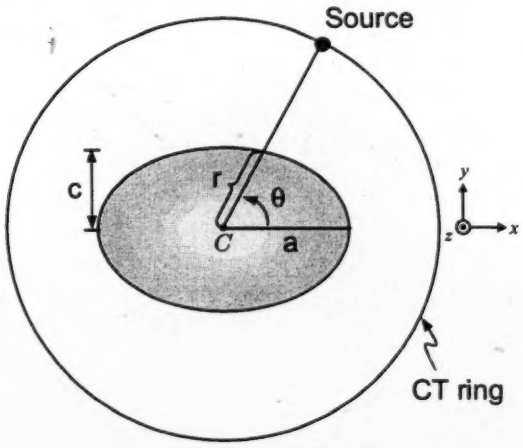

Figure 4.11: Definition of the geometry of an elliptical phantom translating through a CT scanner (z direction) in terms of the center (C) of the phantom and the eccentric/source angle θ. The semi-major and semi-minor axes are denoted as a and c respectively and r is the distance from the phantom center to its surface.

using Eq. (4.8) we have

$$I(r(\theta)) \cong I_o \exp(-\overline{\mu}\, r(\theta)) \tag{4.9}$$

$$= I_o \exp\left(-\overline{\mu}\, a\sqrt{\frac{1-e^2}{1-e^2\cos^2\theta}}\right) \tag{4.10}$$

where I_o is the incident intensity of photons and $\overline{\mu}$ is the average attenuation per unit length over the path $r(\theta)$ in the medium considering the photon energy spectrum of the CT beam. It should be noted that Eq. (4.9) ignores the effect of beam hardening for a polychromatic spectrum in the CT beam. First order inclusion of beam hardening would, at least, require $\overline{\mu}$ to be a function of θ due to $r(\theta)$. However, the derivation as presented was done specifically to understand the phantom shape and helical starting angle effect without complicating the mathematical treatment too much. Since the table position and source angle are related linearly,

$$z = z_o + \frac{\nu\tau}{2\pi}(\theta - \theta_o) \tag{4.11}$$

where θ_o is the source angle at the point z_o, the primary radiation reaching the detector at the center as a function of couch position can be written as

$$I(z) = I_o \exp\left[-\overline{\mu} \cdot a \left(\frac{1-e^2}{1-e^2\cos^2(2\pi z/\nu\tau)}\right)^{1/2}\right] \tag{4.12}$$

We have arbitrarily chosen $\theta_o = 0$ at $z_o = 0$ (the center of the scan length). The use of a rectangular function in generating $D_L(z)$ from the convolution with $f(z)$ assumes a cylindrical phantom since the primary radiation reaching the center of the phantom does not change with z since r is a constant. Therefore the maximum variance in $D_L(0)$, which depends on the relative positions of the detector and source, can be assessed by convolving $f(z)$ with Eq. (4.12).

Figure 4.12 shows the variation with z of the relative intensity of primary photons at the center of an elliptical phantom with dimensions equivalent to the CIRS phantom, for $L = 100$ mm, $\nu\tau = 10$ mm and $\theta_o = 0$ at $z_o = 0$. A value of μ(water, 70 keV)= 0.193 cm^{-1} has been used (Berger et al., 1998). The peaks of the approximately cosine function correspond to the coincidence of the source with the minor axis, $\theta = \pi/2,\ 3\pi/2$ ($r = c$). The horizontal line (i.e., rectangular function) represents the average intensity over one rotation of the source ($1/2\pi \int_0^{2\pi} \exp(-\mu r(\theta))d\theta$) to simulate the ($z$-independent) signal detected in a cylindrical phantom with an equivalent effective attenuation radius (path length) r'. For the equivalent cylindrical phantom, $I/I_o = 0.102$

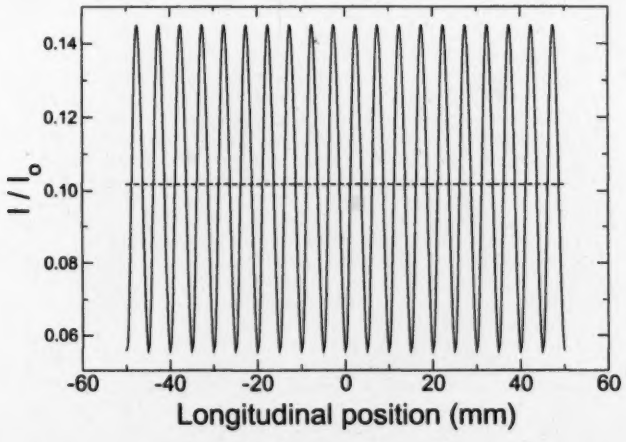

Figure 4.12: Simulated relative intensity of photons reaching the center of elliptical (oscillating curve) and cylindrical (horizontal line) plastic water phantoms as a function of z position for a helical scan series.

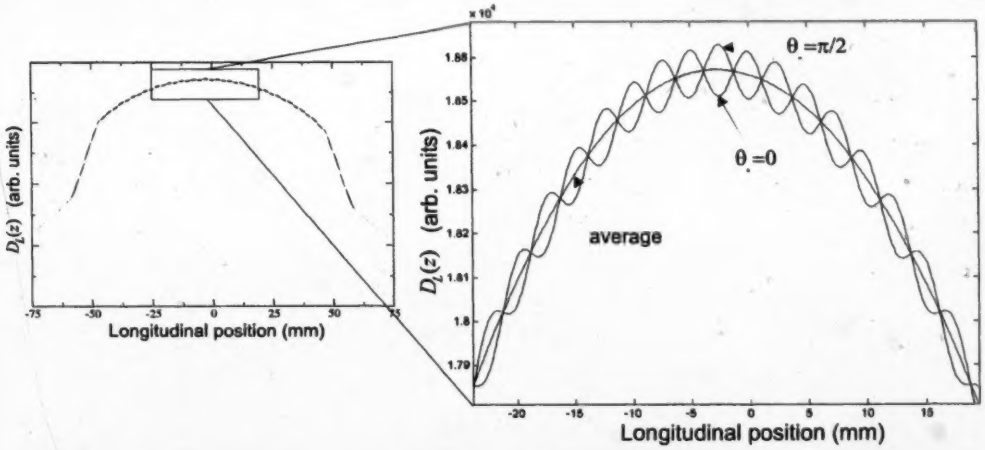

Figure 4.13: Simulated accumulated dose $D_L(z)$ at the center of a elliptical plastic water phantom compared to a cylindrical phantom with an equivalent effective attenuation radius (marked "average"). The oscillating curves are for starting angles of the source 90° out of phase to show the maximum deviation in $D_L(0)$.

corresponding to an effective radius of 11.8 cm ($r' = \ln(I/I_o)/\mu$).

The convolutions $f(z) \otimes I_L(z)$ for the PQ-10 with $\theta_o = 0$ ($r = a$) and $\theta_o = \pi/2$ ($r = c$) are shown on the left of Fig. 4.13 compared to $f(z) \otimes \Pi(z/L)$, both for $L = 100$ mm . Since the difference between the curves is qualitatively negligible, the central region has been enlarged on the right of Fig. 4.13 to show the $< 0.3\%$ maximum variation about the average dose at the center of the scan length. Even though the peak primary intensity at the center of the elliptical phantom changes by about 40% from the average (Fig. 4.12), performing the convolution with the SSDP "smears out" the cumulative dose profile due to the scatter tails of the SSDP. Thus for the PQ-10 at the center of the CIRS phantom, the ellipticity of the phantom can safely be ignored for measuring $D_L(0)$. This can be assumed to be valid in general since all the SSDPs measured in this work are qualitatively similar. For points near the surface however, this assumption may not be valid since the SSDPs would be narrower and the cumulative dose variation with z more pronounced. This was not explored in this work since SSDPs nearer the surface than 6 cm could not be measured in the CIRS phantom.

4.4.3 $D_L(0)$ Results

Values of $D_L(0)$ measured using the IC-10 for axial and helical scans are shown in Tab. IV.b for the PQ5000 and in Tab. IV.c for axial scans on the MX8000. Although doses were measured using the slice widths, scan interval (= 4 mm for all T in axial mode) and pitches (1 and 0.75 for central and off-axis points respectively for all T) previously mentioned, quoted values in Tabs. IV.b and IV.c have been calculated with $\nu\tau = b = T$ in Eqs. (2.25) and (2.30) to facilitate comparison to pencil chamber ($CTDI_{100}$) readings in brackets. Note that in the calculation of $CTDI_{100}$, a value of $L = 102$ mm (active length of the pencil chamber) was used. Both $D_L(0)$ and $CTDI_{100}$ are reported as air-kerma per 100 mAs using a conversion factor from exposure of 8.76 mGy/R. The estimated random uncertainties in $D_L(0)$ and $CTDI_{100}$ are 0.8% and 0.4%, with a systematic uncertainty in both from detector calibration of $\pm 0.6\%$. The measured exposure calibration coefficients (N_X) at 125 kVp (5 mm Al HVL) were 2.065 R per unit corrected electrometer reading and 41.31 R per unit corrected electrometer reading for the PC-4P (pencil) and IC-10 ion chambers respectively. No energy response corrections have been made to $D_L(0)$ and $CTDI_{100}$. Referring back to Fig. 4.1 however, it is evident that moving from the calibration beam ($E_{eff} \approx 43$ keV) to the CT beams ($E_{eff} \approx 59$ keV) may lead to doses, measured using the IC-10 and pencil chambers, systematically $\sim 1 - 2\%$ higher than are reported in Tab. IV.b and IV.c.

A few general observations can be made from Tabs. IV.b and IV.c that are not necessarily new but will be included for completeness. First is that $D_L(0)$ does not change significantly with slice width. Along the central axis, $D_{248}(0)$ for axial scanning on the PQ5000 decreases by only 5% between 10 mm and 3 mm slice widths even though the area under the 10 mm SSDP of Fig. 4.2(a) is obviously larger than the 3 mm SSDP. This is simply because the dose length product has been divided by the nominal slice width ($b = T$) instead of the actual scanning interval of 4 mm. Of course for constant b or $\nu\tau$, $D_L(0)$ will be highly dependent on T. In practice however, contiguous scanning is common and under this condition, $D_L(0)$ decreases only slightly with slice width due to the minor reduction in the relative scatter volume. For the MX8000 scanner, the slice width dependence of $D_L(0)$ is slightly higher with $D_{248}(0)$ for $T = 1 \times 10$ mm about 8% lower than for $T = 1 \times 20$ mm. This is possibly due to the design of a multi-slice system where the radiation

Table IV.b: Accumulated dose at the center of the scan series $D_L(0)$ for the PQ5000 CT scanner. Pencil chamber/$CTDI_{100}$ readings (equivalent to $L = 102$ mm) for comparison are in brackets. Measurement settings: 130 kVp, Axial: $b = 4$ mm for all T, Helical: $\nu\tau = P \cdot T$. Note that the quoted values of $D_L(0)$ have been calculated with $\nu\tau = b = T$ and expressed as air-kerma per 100 mAs.

Slice width, T (mm)	Scan length, L (mm)	$D_L(0)$ (mGy) Center	Off-axis 1	Off-axis 2
Axial				
10	104	8.50 (8.59)	10.8 (11.2)	10.4 (10.8)
	144	9.65	12.0	11.5
	248	11.1	13.3	12.8
5	104	8.19 (8.25)	10.5 (10.6)	10.1 (10.3)
	72	6.88	9.13	8.91
	144	9.30	11.6	11.1
	248	10.7	12.9	12.5
3	104	8.06 (8.17)	–	–
	40	4.93	–	–
	144	9.15	–	–
	248	10.5	–	–
Helical				
10[a]	105	8.45 (8.61)	–	–
	145	9.51	–	–
	245	10.8	–	–
10[b]	101.3	–	10.8 (11.0)	10.4 (10.7)
	146.3	–	11.9	11.5
	251.3	–	13.0	12.5
5[a]	102.5	7.95 (8.29)	–	–
	72.5	6.82	–	–
	142.5	8.99	–	–
	237.5	10.2	–	–
5[b]	103.1	–	10.3 (10.5)	9.99 (10.5)
	69.4	–	8.90	8.77
	140.6	–	11.2	10.9
3[a]	103.5	7.87 (8.17)	–	–
	40.5	5.03	–	–
	139.5	8.80	–	–

[a]pitch = 1
[b]pitch = 0.75

Table IV.c: Accumulated dose at the center of the scan series $D_L(0)$ for the MX8000 Quad multi-slice CT scanner (120 kVp) at the center of the CIRS phantom for axial scans (b = 4 mm for all T). Pencil chamber/$CTDI_{100}$ readings (equivalent to L = 102 mm) for comparison are in brackets. Note that the quoted values of $D_L(0)$ have been calculated with b = slice width and expressed as air-kerma per 100 mAs.

Slice width, T (mm)	Scan length, L (mm)	$D_L(0)$ (mGy)
20	104	6.15 (6.23)
	144	7.09
	248	8.27
10	104	6.62 (6.75)
	144	7.59
	248	8.92

profile is generally larger than the detector array in order to achieve equal intensities to all detector rows. Therefore the change in scatter volume with slice width may not scale the same as single-slice systems. Secondly, the $D_L(0)$ values for the MX8000 are lower than the PQ5000 simply due to the lower kVp (Sec. 2.3.10.1) used in the MX8000 system. All else being equal, $CTDI_{100}$ for modern multi-slice systems is in fact about 10% larger than single slice systems due again to the extended radiation profiles (Lewis, 2001). Lastly, the $CTDI_{100}$ values for a given slice width are slightly different between axial and helical modes. This is simply due to day-to-day variations in scanner output since the $CTDI_{100}$ value to which $D_L(0)$ is compared in Tab. IV.b was always measured immediately after $D_L(0)$.

4.4.3.1 Comparison to Pencil Chamber/$CTDI_{100}$

Since it was never possible to scan a length equal to the active length of the pencil chamber, a 1:1 comparison between $D_{100}(0)$ and $CTDI_{100}$ can not be made. For all scans with nominal L = 100 mm, the IC-10 doses along the central axis were $1-4\%$ lower than the pencil chamber measured $CTDI_{100}$, even though the effective scan lengths were longer. This is again due to the phantom/detector perturbation effects and, to a lesser extent, sampling and averaging effects for the IC-10 case discussed earlier. Under the reasonable assumption that the IC-10 accumulates $D_L(0)$ from the asymmetric SSDP while the pencil chamber integrates the symmetric SSDP (e.g., Fig. 4.3(a)), values of $D_{100}(0)$ and pencil chamber $CTDI_{100}$ agreed to within 1% when the

slightly longer scan lengths ($\sim$ 0.4%/mm in the region $z = \pm 50$ mm) are taken into account. Thus if this particular phantom was to be used for further clinical dose measurements, a correction factor to $D_L(0)$ of $1.03 - 1.04$ may be warranted and would have a slight dependence on the scan length. It may be more beneficial to purchase or manufacture a phantom better suited to this particular application such that the air spaces around the phantom rods have been minimized, similar to PMMA CT phantoms where the rods are designed to fit snugly. The reduction in measured dose due to self-shielding of the detector is unavoidable however and should be taken into account in the final quantification of dose.

4.4.3.2 Helical vs. Axial Modes

The helical values of $D_L(0)$ were slightly lower than the axial values ($0.5 - 1\%$) for similar scan lengths due to axial sampling errors which, although minimized using $b = 4$ mm, were still present. This is consistent with the prediction based on integration of the peak region of the SSDP discussed in Sec. 4.4.1.

4.4.3.3 Long Scan Lengths

Central axis doses for the PQ5000 scanner for $L \approx 250$ mm were up to 29% higher than CTDI_{100} and up to 2.1 times higher than CTDI_{14T} ($T = 3$ mm). The dose difference was even larger for the multi-slice system (MX8000) with $D_{248}(0)$ exceeding CTDI_{100} by 32% for both slice widths studied. These results are consistent with the predictions of Figs. 4.9(a) and 4.9(b). Off-axis point doses for $L = 250$ mm were as much as 22% greater than CTDI_{100} and 41% higher than CTDI_{14T} for the PQ5000.

Based on the results found in this investigation, the dose contribution to the volume adjacent to the scan plane at the center of a trunk phantom, due to scattered radiation, extends significantly further than has been previously reported formally. Clearly, 15 cm long CTDI phantoms and 10 cm long pencil chambers are inadequate to properly measure the accumulated dose from a CT body scan series. These and other conclusions are discussed in the next chapter.

Chapter 4 References

Akima, H. (1970). A new method of interpolation and smooth curve fitting based on local procedures. *J. ACM.*, 17:589–602.

Berger, M. J., Coursey, J. S., and Zucker, M. A. (2000). Stopping-power and range tables for electrons, protons, and helium ions. http://physics.nist.gov/PhysRefData/Star/Text/contents.html.

Berger, M. J., Hubbell, J. H., Seltzer, S. M., Coursey, J. S., and Zucker, D. S. (1998). XCOM: Photon Cross Sections Database. http://physics.nist.gov/PhysRefData/Xcom/Text/XCOM.html.

Boone, J. M., Cooper III, V. N., Nemzek, W. R., McGahan, J. P., and Seibert, J. A. (2000). Monte carlo assessment of computed tomography dose to tissue adjacent to the scanned volume. *Med. Phys.*, 27(10):2393–407.

Burden, R. L. and Faires, J. D. (1997). *Numerical Analysis.* Brooks/Cole, Pacific Grove, CA, 6th edition.

Johns, H. E. and Cunningham, J. R. (1983). *The Physics of Radiology.* Charles C. Thomas, Springfield, Illinois, 4th edition.

Jucius, R. A. and Kambic, G. X. (1977). Radiation dosimetry in computed tomography. *Proc. SPIE*, 127:286–295.

Khan, F. M. (1994). *The Physics of Radiation Therapy.* Williams and Wilkins, Baltimore, MD, 2nd edition.

Lewis, M. A. (2001). Multislice CT: opportunities and challenges. *Br. J. Radiol.*, 74:779–781.

McNitt, M., Cagnon, C., Solberg, T., and Chetty, I. (1999). Radiation dose in spiral CT: The relative effects of collimation and pitch. *Med. Phys.*, 26:409–414.

Oliveira, A. D., Alves, J. G., Carvalho, A. F., and Carreiro, J. V. (1995). Dose profile and dose index analysis in computed tomography. *Radiat. Prot. Dosimetry*, 57:387–391.

Seuntjens, J., Aalbers, A., Grimbergen, T., Mijnheer, B., Thierens, H., Van Dam, J., Wittkamper, F., Zoetlief, J., Piessens, M., and Piret, P. (1999). Suitability of diamond detectors to measure central axis depth kerma curves for low- and medium-energy x-rays. In *Kilovoltage X-Ray Dosimetry*, pages 227–238. Medical Physics Publishing, Madison.

Shope, T. B., Gagne, R. M., and Johnson, G. C. (1981). A method for describing the doses delivered by transmission x-ray computed tomography. *Med. Phys.*, 8(4):488–495.

Tsai, H. Y., Tung, C. J., Huang, M. H., and Wan, Y. L. (2003). Analyses and applications of single scan dose profiles in computed tomography. *Med. Phys.*, 30(8):1982–1989.

Weisstein, E. W. (2004). Ellipse. *Mathworld-A Wolfram Web Resource.* http://mathworld.wofram.com/Ellipse.html.

Yin, Z., Hugtenburg, R. P., Green, S., and Beddoe, A. H. (2004). Dose responses of diamond detectors to monoenergetic x-rays. *Nucl. Instr. and Meth. in Phys. Res. B.*, 213:646–649.

Chapter 5

Conclusions

Single Scan Dose Profile Measurements Using a PTW Diamond Detector

An investigation of the use of a PTW Riga Type 60003 diamond detector for measuring relative single scan dose profiles (SSDPs) in CT has been conducted in this work. The small active length of the diamond detector (0.25 mm) potentially provides an almost four-fold improvement over 0.9 mm LiF TLDs conventionally used for SSDP measurement. SSDPs were measured with the diamond detector in a 30 cm long CIRS elliptical, plastic-water phantom and standard 15 cm long cylindrical PMMA CTDI head and body phantoms by axially scanning over the length of the phantoms. This was performed for several slice widths on two CT systems: a Philips PQ5000 single-slice scanner and a Philips MX8000 Quad multi-slice scanner. Using this method, the maximum attainable spatial resolution is determined by the minimum z increment of the couch, which was 0.5 mm for the two scanners.

Significant dose to the volume adjacent to the scan plane was observed in the plastic-water phantom and to a lesser extent in the CTDI phantoms. The dose at $z = \pm 50$ mm at the center of the plastic-water phantom, relative to the SSDP peak dose, ranged from $11 - 14\%$ for 3 mm - 10 mm slice widths on the PQ5000 scanner and from $10 - 23\%$ for 1×4 mm - 1×20 mm slice selections on the MX8000 scanner. Clearly the historical assumption that most of the SSDP is contained within the 10 cm active length of pencil ion chambers is invalid at the center of a trunk phantom. Even at the center of the CTDI body phantom, the relative dose at $z = \pm 50$ mm was about 12% for a 5 mm slice

width. More importantly, the scatter tails of SSDPs measured at the center of the plastic-water phantom extended significantly farther (up to $z = \pm 125$ mm) than previously reported, due most likely to the insufficient length of 15 cm long CTDI phantoms used for measurement. Numeric integration of the central axis SSDPs over 250 mm lead to integral doses about 30% higher than the integrals over 100 mm for all slice widths and scanners studied. The differences in integral dose over the same interval for off-axis points ($6 - 7$ cm depth) in the CIRS phantom was about 20%.

A single SSDP was measured at the center of the CIRS phantom using LiF TLDs and a Wellhöfer IC-10 small volume ion chamber (3.3 mm active length), and compared to the diamond-measured SSDP. All three profiles were nearly identical apart from the volume averaging of the IC-10 near the SSDP peak. Therefore the observation of the long scatter tails in the SSDPs does not depend on the detector used for measurement but is mostly due to the length of the phantom.

An analytic form consisting of the sum of two modified Gaussians plus an asymmetry term was developed and applied to all the diamond-measured SSDPs. Correlation coefficients (R^2) for two example SSDPs were 0.9996 and 0.9999 which were representative of all the profile fits. The qualitative shape and therefore the functional form of the SSDPs were different than those reported in the literature. This is most likely a result of the different scattering properties and longer length of the plastic-water phantom used in this study compared to conventional PMMA CTDI phantoms. Therefore, standard CTDI phantom should really only be used to monitor the output of a CT scanner since they do not adequately represent the scatter conditions in a real patient.

Although SSDP data acquisition time using the diamond detector is longer than the TLD method, the total time (after incorporating TLD preparation and annealing times) to obtain a SSDP using the diamond detector is shorter (< 30 min) and produces equal or perhaps better precision than TLDs. If this particular CIRS phantom were to be used, one would have to account however for the reduction in scatter due primarily to the air spaces around the phantom rods and to a lesser extent, the self-shielding of the diamond detector to large-angle scatter. Both factors lead to an asymmetry in the measured profiles. The asymmetry could be minimized by purchasing or manufacturing a phantom for specific use in CT dosimetry where the air spaces are reduced. However, it was

observed that the actual CT beam profiles were symmetric. Therefore it would only be necessary to measure half the SSDP and mathematically reconstruct the other half. Ideally one should choose a phantom equal to twice the width of the SSDP such that the SSDP does not change over the scan length due to insufficient inward sidescatter near the phantom edges. This is probably not practical but the phantom should be at least 25 cm long, considerably longer than the 15 cm long CTDI phantoms currently in use.

Accumulated Dose Measurements Using a Small Volume Ion Chamber

The absolute accumulated dose from a series of axial or helical CT scans, measured using a small volume ion chamber, was investigated. The maximum accumulated dose at the center of axial and helical scan series of length L, $D_L(0)$, was measured at the center and off-axis points of the CIRS plastic-water phantom using the IC-10 ion chamber. Under the $D_L(0)$ formalism, $D_{100}(0) = \text{CTDI}_{100}$. For a nominal scan length of 100 mm, values of $D_L(0)$ agreed with CTDI_{100} doses, measured using a Capintec PC-4P 102 mm long pencil ion chamber, to within 4% for slice widths of 3 mm, 5 mm and 10 mm on the PQ5000 single-slice scanner and 1×10 mm and 1×20 mm slice selections on the MX8000 multi-slice scanner. After correcting for differences between the effective scan lengths of the two methods, and phantom/chamber perturbation effects introduced using the IC-10 chamber, results agreed to within 1%. When scanning a length of 250 mm, the center point doses (i.e., $D_{250}(0)$) measured using the IC-10 were consistently about 30% higher than CTDI_{100} for all slice widths studied. This was in general agreement with the numeric integration of the SSDPs measured using the diamond detector. For the PQ5000, $T = 3$ mm, $D_{250}(0)$ was over two times higher than D_{14T} which highlights the inadequacy of CTDI_{14T} for small slice widths. For off-axis points at 6 cm and 7 cm depth in the phantom, $D_{250}(0)$ values were about $18 - 20\%$ higher than CTDI_{100}. For a given slice width and scan length, $D_L(0)$ measured for axial scanning was slightly larger than for helical scanning due to sampling errors introduced in using a 4 mm slice interval for axial mode.

The accumulated dose at the center of the scan series in CT depends on the scan length and width of the SSDP. Therefore the dose reported using

a 100 mm long pencil chamber would be "correct" only for a scan length of 100 mm. Clinical scan lengths >250 mm are not uncommon. In our clinic, the average body scan lengths on the PQ5000 system used for radiotherapy treatment planning is 400 mm while body scan lengths on the MX8000 used for diagnostic radiology are typically 800 mm. This means that the dose delivered to the patient is larger than what is reported based on a 100 mm scan length ($CTDI_{100}$). The equilibrium dose at the phantom center for most slide widths was reached for scan lengths > 300 mm which would result in patient dose becoming even higher for longer scan lengths. Therefore, it has been shown that for long body scan lengths, reporting the dose as $CTDI_{100}$ or $CTDI_{14T}$ can greatly underestimate the actual accumulated dose. One important utility of the method of calculating $D_L(0)$ is that the dose for a CT scan series of *any* length (including the equilibrium case when the scan length is longer than the width of the SSDP) or scan spacing can be calculated using Eq. (2.25) once the SSDP has been acquired. An accurate relative SSDP can be measured quite quickly using the diamond detector. If correction factors for energy response for the diamond detector were determined, absolute dose profiles could be obtained as well. However, for routine QA, the small ion chamber method is much easier and can be used for any scan and phantom lengths. Measuring $D_L(0)$ using a small ion chamber is not considerably more time consuming than the pencil chamber method and is much more flexible.

List of Citations

AAPM (1993). Task group 2: Diagnostic x-ray imaging, report no. 39: Specification and acceptance testing of computed tomography scanners. Technical report, American Institute of Physics, . . . 1, 27

Akima, H. (1970). A new method of interpolation and smooth curve fitting based on local procedures. *J. ACM.*, 17:589–602, . . . 93

Atherton, J. V. and Huda, W. (1995). CT doses in cylindrical phantoms. *Phys. Med. Biol.*, 40(5):891–911, . . . 16, 35, 47

Atherton, J. V. and Huda, W. (1996). Energy imparted and effective doses in computed tomography. *Med. Phys.*, 23(5):735–41, . . . 35

Attix, F. H. (1986). *Introduction to Radiological Physics and Radiation Dosimetry.* John Wiley & Sons, New York, . . . 25, 26, 54, 79

Avilés Lucas, P., Dance, D. R., Castellano, I. A., and Vañó, E. (2004). Monte Carlo simulations in CT for the study of the surface air kerma and energy imparted to phantoms of varying size and position. *Phys. Med. Biol.*, 49:1439–1454, . . . 2

Barnett, E. (2004). Characterization of a diamond detector for intensity modulated point dose measurements. Master's thesis, University of Alberta, . . . 62, 63

Berger, M. J., Coursey, J. S., and Zucker, M. A. (2000). Stopping-power and range tables for electrons, protons, and helium ions. http://physics.nist.gov/PhysRefData/Star/Text/contents.html, . . . 18, 80, 89, 90, 92, 108

Berger, M. J., Hubbell, J. H., Seltzer, S. M., Coursey, J. S., and Zucker, D. S. (1998). XCOM: Photon Cross Sections Database. http://physics.nist.gov/PhysRefData/Xcom/Text/XCOM.html, . . . 92

Bochud, F. O., Grecescu, M., and Valley, J. (2001). Calibration of ionization chambers in air kerma length. *Phys. Med. Biol.*, 46:2477–2487, . . . 30

Boone, J. M., Cooper III, V. N., Nemzek, W. R., McGahan, J. P., and Seibert, J. A. (2000). Monte carlo assessment of computed tomography dose to tissue adjacent to the scanned volume. *Med. Phys.*, 27(10):2393–407, . . . 3, 35, 46, 47, 103

Boutillon, M. and Perroche-Roux, A. M. (1987). Re-evaluation of the W value for electrons in dry air. *Phys. Med. Biol.*, 32(2):213–219, . . . 58, 79

Brooks, R. A. and Di Chiro, G. (1976). Statistical limitations in X-ray reconstructive tomography. *Med. Phys.*, 3:237–240, . . . 42

Burden, R. L. and Faires, J. D. (1997). *Numerical Analysis*. Brooks/Cole, Pacific Grove, CA, 6th edition, . . . 93

Bushberg, J. T., Seibert, J. A., Leidholt, J. E. M., and Boone, J. M. (2002). *The Essential Physics of Medical Imaging*. Lippincott Williamn & Wilkins, Philadelphia, . . . 8, 42

Chen, X., Schaller, S., and Flohr, T. (2000). Multislice CT-Basics and Applications. In *Somatom Sessions*, volume 6, pages 3–8. Siemens Medical Systems, . . . 56

Cheung, T., Cheng, Q., Feng, D., and Stokes, M. J. (2001). Study on examinee's dose delivered in computed tomography. *Phys. Med. Biol.*, 46(3):813–20, . . . 26, 47

Conway, B. J., McCrohan, J. L., Antonsen, R. G., Rueter, F. G., Slayton, R. J., and Suleiman, O. H. (1992). Average radiation dose in standard CT examinations of the head: Results of the 1990 NEXT survey. *Radiology*, 184:135–140, . . . 21

Davis, S. D., Ross, C. K., Mobit, P. N., Van der Zwan, L., Chase, W. J., and Shortt, K. R. (2003). The response of LiF thermoluminescence dosemeters

to photon beams in the energy range from 30 kV x rays to ^{60}Co gamma rays. *Radiat. Prot. Dosimetry.*, 106(1):33–43, . . . 26, 65

De Angelis, C., Onori, S., Pacilio, M., Cirrone, G. A. P., Cuttone, G., Raffaele, L., Bucciolini, M., and Mazzocchi, S. (2002). An investigation of the operating characteristics of two PTW diamond detectors in photon and electron beams. *Med. Phys.*, 29:248–254, . . . 58, 62

Dixon, R. L. (2003). A new look at CT dose measurement: Beyond CTDI. *Med. Phys.*, 30(6):1272–1280, . . . 3, 23, 36, 39-41, 46-48, 83

Dixon, R. L. and Ekstrand, E. E. (1978). A film dosimetry system for use in computed tomography. *Radiology*, 127:255–258, . . . 1, 25

FDA (2003). Code of federal regulations: Performance standards for ionizing radiation emitting products. Technical Report 21CFR 1020.33, . . . 12, 19, 23, 26, 31

Findanzio, A., Azario, L., Miceli, R., Russo, A., and Piermattei, A. (2000). PTW-diamond detector: Dose rate and particle type dependence. *Med. Phys.*, 27:2589–2593, . . . 62

Fowler, J. F. (1966). *Radiation Dosimetry*, volume 2, chapter Solid State Electrical Conductivity in Radiation Dosimetry, pages 291–324. Academic, . . . 62

Goldman, L. W. and Fowlkes, J. B., editors (1995). *Medical CT and Ultrasound.* Advanced Medical Publishing, . . . 8

Herman, G. T. (1980). *Image Reconstruction from Projections: The Fundamentals of Computerized Tomography.* Academic Press, New York, . . . 10

Heydarian, M., Hoban, P. W., Beckham, W. A., Borchardt, I. M., and Beddoe, A. H. (1993). Evaluation of a PTW diamond detector for electron beam measurements. *Phys. Med. Biol.*, pages 1035–1042, . . . 63

Hoban, P. W., Heydarian, M., Beckham, W. A., and Beddoe, A. H. (1994). Dose rate dependence of a PTW diamond detector in the dosimetry of a 6 MV beam. *Phys. Med. Biol.*, 39:1219–1229, . . . 61, 62

Hounsfield, G. N. (1973). Computerized transverse axial scanning (tomography). *Br. J. Radiol.*, 46:1023–1047, . . . 8

Huda, W. and Atherton, J. V. (1995). Energy imparted in computed tomography. *Med. Phys.*, 22(8):1263–1269, . . . 35

Hugtenburg, R. P., Johnston, K., Chalmers, G. J., and Beddoe, A. H. (2001). Application of diamond detectors fo the dosimetry of 45 and 100 kVp therapy beams: comparison with a parallel-plate ionization chamber and Monte Carlo. *Phys. Med. Biol.*, 46:2489–2501, . . . 61-63

ICRP60 (1991). 1990 recommendations of the International Commission on Radiological Protection. Technical Report 60, Internation Commission on Radiological Protection, Oxford: Pergamon Press, . . . 34

ImPACT (2001). Information leaflet no. 1: CT scanner acceptance testing. Technical report, Imaging Performance Assessment of CT Scanners, Medicines and Health Care Products Regulatory Agency, St. George's Hospital, London, UK. Available from http://www.impactscan.org, . . . 48

ImPACT (2004). ImPACT CTDI Tables. Technical report, Imaging Performance Assessment of CT Scanners, Medicines and Health Care Products Regulatory Agency, St. George's Hospital, London, UK. http://www.impactscan.org, . . . 31, 32

Johns, H. E. and Cunningham, J. R. (1983). *The Physics of Radiology*. Charles C. Thomas, Springfield, Illinois, 4th edition, . . . 92, 93

Jones, D. G. and Shrimpton, P. C. (1993). Survey of CT practice in the UK-part 3: normalized organ doses calculated using Monte Carlo techniques. Technical Report R250, National Radiological Protection Board (NRBP), London:HMSO, . . . 34

Jucius, R. A. and Kambic, G. X. (1977). Radiation dosimetry in computed tomography. *Proc. SPIE*, 127:286–295, . . . 1, 16, 22, 28, 30, 63, 90

Kachelriess, M., Ulzheimer, S., and Kalendar, W. (2000). ECG-correlated image reconstruction from subsecond multi-slice spiral CT scans of the heart. *Med. Phys.*, 27(8):1881–1902, . . . 12

Kalendar, W. A. (2000). *Computed Tomography.* Publicis MCD Verlag, Munich, . . . 8, 10, 16, 31

Khan, F. M. (1994). *The Physics of Radiation Therapy.* Williams and Wilkins, Baltimore, MD, 2nd edition, . . . 18, 19, 58, 65, 80, 89, 92

Knox, H. H. and Gagne, R. M. (1996). Alternative methods of obtaining the computed tomography dose index. *Health Phys.*, 71(2):219–224, . . . 31, 32

Laub, W. U. and Wong, T. (2003). The volume effect of detectors in the dosimetry of small fields used in IMRT. *Med. Phys.*, 30(3):341–7, . . . 2

Leitz, W., Axelsson, B., and Szendro, G. (1995). Computed tomography dose assessment-a practical approach. *Radiat. Prot. Dosimetry*, 57:377–380, . . . 17, 28, 32, 33

Lewis, M. A. (2001). Multislice CT: opportunities and challenges. *Br. J. Radiol.*, 74:779–781, . . . 45, 112

Mainwood, A. (2000). Recent developments of diamond detectors for particles and UV radiation. *Semicond. Sci. Technol.*, 15:R55–R63, . . . 58, 60

Martens, C., De Wagter, C., and De Neve, W. (2000). The value of the PinPoint ion chamber for characterization of small field segments used in intensity-modulated radiotherapy. *Phys. Med. Biol.*, 45:2519–2530, . . . 64

McCaffrey, J. P. and Rogers, D. W. O. (2003). Calibration of a Capintec model 192 electrometer serial number 544761324, with a PTW model N30004 ionization chamber serial number 0010. Technical Report IRS-2003-0883, National Research Council (NRC) Canada, . . . 77

McCrohan, J. L., Patterson, J. F., Gagne, R. M., and Goldstein, H. A. (1987). Average radiation doses in a standard head examination for 250 CT systems. *Radiology*, 163:263–268, . . . 30

McGhee, P. L. and Humphreys, S. (1994). Radiation dose associated with spiral computed tomography. *Can. Assoc. Radiol. J.*, 45(2):124–9, . . . 21, 28, 47

McNitt, M., Cagnon, C., Solberg, T., and Chetty, I. (1999). Radiation dose in spiral CT: The relative effects of collimation and pitch. *Med. Phys.*, 26:409–414, . . . 24, 43, 44, 47, 100

Mettler, F. A., J., Wiest, P. W., Locken, J. A., and Kelsey, C. A. (2000). CT scanning: Patterns of use and dose. *J. Radiol. Prot.*, 20(4):353–9, . . . 1

Mobit, P. N. and Sandison, G. A. (1999). A Monte Carlo comparison of the response of the PTW-diamond and TL-diamond detectors in megavoltage photon beams. *Med. Phys.*, 26(11):2503–2507, . . . 58

Nagel, H. D. (2000). *Radiation Exposure in Computed Tomography.* European Coordination Committee of the Radiological and Electromedical Industries, . . . 34

Nickoloff, E. L., Dutta, A. K., and Lu, Z. F. (2003). Influence of phantom diameter, kVp and scan mode upon computed tomography dose index. *Med. Phys.*, 30(3):395–402, . . . 2, 21, 43, 44

Oliveira, A. D., Alves, J. G., Carvalho, A. F., and Carreiro, J. V. (1995). Dose profile and dose index analysis in computed tomography. *Radiat. Prot. Dosimetry*, 57:387–391, . . . 24, 93, 94

OOPEC (1999). European guidelines on quality criteria for computed tomography. Technical Report Report 16262, Office for Official Publications of the European Communities, . . . 32, 33

Pavlicek, W., Horton, J., and Turco, R. (1979). Evaluation of the MDH Industries, Inc. pencil chamber for direct beam CT measurements. *Health Phys.*, 37:773–774, . . . 30

Planskoy, B. (1980). Evaluation of diamond radiation dosemeters. *Phys. Med. Biol.*, 25(3):519–32, . . . 2, 58, 61

Radon, J. H. (1986). On determination of functions from their integral values along certain manifolds. *IEEE Transactions on Medical Imaging*, MI-5(4):170–176. English translation of the original 1917 paper, . . . 8

Ramo, S. (1939). *Proc. IRE*, 27:584, . . . 61

Rothenburg, L. and Pentlow, K. (1995). *Medical CT and Ultrasound*, chapter CT Dosimetry and Radiation Safety, pages 519–553. Advanced Medical Publishing, Madison, WI, . . . 27-29

Rustgi, S. N. (1995). Evaluation of the dosimetric characteristics of a diamond detector for photon beam measurements. *Med. Phys.*, 22(5):567–70. 0094-2405 Journal Article, . . . 58, 62

Seuntjens, J., Aalbers, A., Grimbergen, T., Mijnheer, B., Thierens, H., Van Dam, J., Wittkamper, F., Zoetlief, J., Piessens, M., and Piret, P. (1999). Suitability of diamond detectors to measure central axis depth kerma curves for low- and medium-energy x-rays. In *Kilovoltage X-Ray Dosimetry*, pages 227–238. Medical Physics Publishing, Madison, . . . 61, 90

Shope, T. B., Gagne, R. M., and Johnson, G. C. (1981). A method for describing the doses delivered by transmission x-ray computed tomography. *Med. Phys.*, 8(4):488–495, . . . 1, 21-23, 28, 30, 93

Shope, T. B., Morgan, T. J., Showalter, C. K., Pentlow, K. S., Rothenberg, L. N., White, D. R., and Speller, R. D. (1982). Radiation dosimetry survey of computed tomography systems from ten manufacturers. *Br. J. Radiol.*, 55(649):60–9, . . . 1, 21, 25, 46, 47

Shrimpton, P. C., Jones, D. G., Hillier, M. C., Wall, B. F., Le Heron, J. C., and Faulkner, K. (1991). Survey of CT practice in the UK-part 2: Dosimetric aspects. Technical Report R249, National Radiological Protection Board (NRBP), London:HMSO, . . . 34

Spokas, J. J. (1982). Dose descriptors for computed tomography. *Med. Phys.*, 9(2):288–92, . . . 23, 24

Suess, C., Kalendar, W. A., and Polacin, A. (1995). *Medical CT and Ultrasound*, chapter Performance Evaluation and Quality Control in CT. Advanced Medical Publishing, Madison, WA, . . . 13

Suzuki, A. and Suzuki, M. N. (1978). Use of a pencil-shaped ionization chamber for measurement of exposure resulting from a computed tomography scan. *Med. Phys.*, 5(6):536–9, . . . 1, 29, 63

Tapper, R. J. (2000). Diamond detectors in particle physics. *Rep. Prog. Phys.*, 63:1273–1316, . . . 60

Tsai, H. Y., Tung, C. J., Huang, M. H., and Wan, Y. L. (2003). Analyses and applications of single scan dose profiles in computed tomography. *Med. Phys.*, 30(8):1982–1989, . . . 26, 28, 47, 90, 93, 99

Van Dyk, J. (1999). *The Modern Technology of Radiation Oncology.* Medical Physics Publishing, Madison, . . . 8

Weisstein, E. W. (2004). Ellipse. *Mathworld-A Wolfram Web Resource.* http://mathworld.wofram.com/Ellipse.html, . . . 106

Yin, Z., Hugtenburg, R. P., Green, S., and Beddoe, A. H. (2004). Dose responses of diamond detectors to monoenergetic x-rays. *Nucl. Instr. and Meth. in Phys. Res. B.*, 213:646–649, . . . 61, 90

Zhu, X. R., Yoo, S., Jursinic, P. A., Grimm, D. F., Lopez, F., Rownd, J. J., and Gillin, M. T. (2003). Characteristics of sensitometric curves of radiographic films. *Med. Phys.*, 30(5):912–919, . . . 78

Zink, F. E. and McCollough, C. H. (1994). The measurement of radiation dose profiles for electron-beam computed tomography using film dosimetry. *Med. Phys.*, 21(8):1287–1291, . . . 26